FLUORESCENCE MICROSCOPY TOOLS FOR IN SITU CATALYST CHARACTERIZATION

Alexey KUBAREV

Supervisor:
Prof. M. Roeffaers, KU Leuven

Members of the Examination Committee:
Prof. E. Schrevens, KU Leuven, Chair
Prof. D. De Vos, KU Leuven
Prof. J. Hofkens, KU Leuven
Prof. S. De Feyter, KU Leuven
Prof. B. Weckhuysen, Utrecht University

Dissertation presented
in partial fulfilment of
the requirements for the
degree of Doctor of
Bioscience Engineering
(PhD)

June 2017

Doctoraatsproefschrift nr. 1429 aan de faculteit Bio-ingenieurswetenschappen van de KU Leuven

Uitgegeven in eigen beheer, Alexey Kubarev, Heverlee

PREFACE

When I was moving from Russia to Belgium to start my PhD, I felt I was making a leap to the unknown. I didn't know much about my future supervisor, and virtually nothing about my future colleagues. Multiply that by the potential cultural differences and now one could understand my concerns. Now, after more than four years in Leuven, I can definitely say that these fears were completely unjustified. The level of support from my friends and colleagues I received during my PhD was enormous and I am happy you were around.

First of all, I would like to thank my dear supervisor professor **Maarten Roeffaers**. During my PhD I received constant support and feedback from him, both in formal and informal context. I quickly learned to know that I can ask any question or suggest any idea without a fear to look stupid, and that means a lot to me. With a time, he provided me with more and more research freedom which was essential for me to develop as an independent researcher. I am grateful for him learning to appreciate my straightforwardness and teaching me how to use it to my advantage as well as when to not use it at all.

Then I would like to thank my assessors, professors **Johan Hofkens** and **Dirk De Vos**, who have not only critically evaluated my PhD progress during its milestones, but also were always available when I required their expertise.

Further, I would like to express my gratitude to the members of my examination committee professors **Steven De Feyter** and **Bert Weckhuysen** and examination committee chair professor **Eddie Schrevens** for the readiness to participate in this crucial part of PhD and the invaluable input during the preliminary defense, which enabled me to improve my PhD thesis.

I sincerely thank all my colleagues from Maarten's group, and in particular:

- **Liu, Jordi, Kris,** and **Guillaume** for the engaging discussions, collaboration and joint article-writing;
- **Filippo** for teaching me the single-molecule fluorescence microscopy;
- **Arnica** for the assistance with writing this thesis;
- **Christian, Eva, Wouter V., Dennis, Collin, Koen, Julian**, and others for a good collegial spirit, great company and readiness to help.

But in addition to the small research group of immediate colleagues, I have always felt that I belong to two bigger families – both the research group of Molecular Imaging and Photonics and the Centre for Surface Chemistry and Catalysis. I am immensely grateful for this feeling of belonging and friendly team spirit. In particular I want to thank:

- **Jeroen and Susanna** for the constant assistance with intricacies of wide-field fluorescence microscopy setups;
- **Peter** for assistance with Localizer software and Igor programming;
- **Charlotte, Lieve, Herlinde, Eduardo, Elke de Z., Elke D., Doortje, Bartosz, Jochem, Viktorija, Jelle, Wouter B.**, and others for great parties and family feel;
- **Pieterjan, Trees, Ivo,** and **Eric** for the collaborations and shared articles;
- **Carine, Annelies,** and **Sabina** for constant care that everyone in the lab has everything they need for the lab to run smoothly.

Further, I would like to thank my international collaborators **Zoran** and **Frank** (Utrecht University), and **Nikolay** and **Alexey** (TU Eindhoven) for our join fruitful work which resulted in several great publications.

A good work needs to be supported by good fun time. I would like to thank all my friends whom I have met in Leuven, especially **Anya, Dima, Ania, Mat, Goda, Marco, Nastya, Ksusha, Mada, Tomer, Neta, Einat, Kaveh, Eric, Stefanie, Danielle, Jasper, Maciek, Javier, Jehan, Sam, Steven**, and many others. Your company helped me to put my mind off work for a while, so it could process scientific problems in the background.

Наконец, я бы хотел от всей души поблагодарить мою семью. Моих родителей **Ирину** и **Славу**, которые, несмотря на тысячи километров между нами уже почти 15 лет, всегда как будто бы рядом, всегда знают что сказать, и всегда готовы приехать и поддержать меня. Мою сестру **Полину**, которая всегда искренне радовалась моим успехам и обсуждала со мной жизнь в аспирантуре. Мою дочку **Алису**, которая как яркое солнце освещала вечера после тяжелых дней в лаборатории. И конечно же мою дорогую жену **Сашу**, которая не только поддерживала меня и в радости, и в горе, но и помогла значительно улучшить мои писательские и научные навыки в ходе обсуждения моих текстов и моей работы.

This work wouldn’t be possible without all of you.

ABSTRACT

Catalyst characterization is an integral part of catalyst design and development. Traditionally, it is done with ensemble-based information averaging techniques, which overlook variations in catalytic properties within the sample batch. While hard to detect, such variations can lead to inefficient material use. Recently a number of fluorescence microscopy techniques have been introduced to catalysis research. These techniques can detect catalyst properties at single particle and even at the single-molecule level. The main goal of this PhD thesis is to apply fluorescence microscopy to investigate the interplay between local catalytic performance and catalyst porosity and to derive structure-activity and selectivity relationships for heterogeneous catalysts at the level of individual catalytic turnovers. To achieve this goal, I employed both diffraction-limited and super-resolution fluorescence microscopy with support from other techniques.

In **Chapters 2 and 3**, I used super-resolution fluorescence microscopy, Raman microspectroscopy, and focused-ion-beam-assisted scanning electron microscopy to study the effects of dealumination on catalytic activity and acid sites distribution of mordenite zeolites. Dealumination of zeolites is a common post-synthetic treatment to enhance mass transfer by introducing extra-framework porosity at the expense of acid sites. However, due to the tradeoff between porosity gain and acid site loss, it is important to study the effects of dealumination on catalytic performance at single-crystal level. I uncovered remarkable inter- and intracrystal heterogeneities in catalytic activity and acid sites distribution. The non-dealuminated samples did not contain these heterogeneities. Based on these results, I proposed a dealumination mechanism for mordenites. In addition to these, I also discovered ordered extra-framework meso/macropores in these samples. These pores provide an increase in molecular diffusion and allow for catalytic reaction inside zeolite crystal. However, the catalytic activity is not limited to the extra-framework pores. A majority of catalytic conversions happen in the original micropores of mordenite structure, in vicinity of the extra-framework pores or outer surface. Overall, I identified suboptimal catalytic properties of dealuminated mordenites and its origin being commercial, large-scale dealumination.

As the next step of this project I studied the structure/activity relationship of other zeolite, ZSM-5, which is a widely used shape-selective zeolite catalyst. It has two types of micropores which slightly differ in size and geometry. Based on literature reports of preferential sorption of aromatic molecules in different

pores depending on the conditions, I proposed that it could be possible to induce pore preference in H-ZSM-5-catalyzed reaction. In **Chapter 4** I used fluorescence microscopy to show that acid-catalyzed furfuryl alcohol oligomerization reaction can preferentially occur in one or the other micropore subsystem of H-ZSM-5 crystals depending on solvent polarity. This result can be used to selectively perform catalytic reactions in either micropore subsystem.

To further expand the range of the catalysts which could be investigated by fluorescence microscopy, I studied catalytic activity of metal-organic framework (MOF) zeolitic imidazolate framework ZIF-8. ZIF-8 has been reported to be catalytically active in (trans)esterification reactions, which makes it useful for biodiesel production. However, the origin and location of its active sites are debated. In **Chapter 5** I investigated catalytic activity of ZIF-8 single crystals with fluorescence microscopy. I discovered that catalytic activity of ZIF-8 is limited to the outer surface and bulk crystal defects, what results in inefficient use of catalyst material. To combat surface-only activity I used an oleic acid etching to successfully increase molecular penetration of the whole crystal volume. While successful in attaining the latter, the unfortunately strong adsorption of the pore-inducing agent at the catalytic site leads to an overall decrease in catalytic activity.

In conclusion, in this thesis I have applied fluorescence microscopy to resolve the structure-activity relationships in zeolites and MOFs, and suggested strategies to optimize catalytic activity. The results and the wealth of inferences therefrom demonstrate how fluorescence microscopy can enrich catalysis research as a characterization method. Such studies can be used to advance the field of catalyst design and development.

SAMENVATTING

Karakterisatie vormt een integraal onderdeel van het ontwerp en de ontwikkeling van meer performante katalysatoren. Typisch wordt dit gedaan op de bulk schaal. Hierdoor gaan details op de kleinste lengteschalen vaak verloren. Door de recente introductie van fluorescentiemicroscopie in het katalyseonderzoek, is het nu echter mogelijk om het katalytische proces te bestuderen op het niveau van enkelvoudige kristallen en zelfs individuele moleculen. In dit doctoraatswerk werd met behulp van fluorescentiemicroscopie gefocust op de katalytische activiteit van individuele katalysatorkristallen meer specifiek naar de link tussen porositeit, activiteit, en selectiviteit. Zo heb ik voor zeolieten en metaal organische roosters structuur-activiteit relaties bepaald tot op het niveau van individuele katalytische conversies. Hiervoor werd zowel diffractie-gelimiteerde als super-resolutie fluorescentiemicroscopie aangewend.

In **hoofdstukken 2 en 3** wordt super-resolutie fluorescentiemicroscopie, Raman microspectroscopie, en rasterelektronenmicroscopie gebruikt om de effecten van dealuminatie op de katalytische activiteit van zure mordeniet zeolieten te bestuderen. Vaak wordt dergelijke zeolietdealuminatie aangewend om post-synthetisch additionele porositeit in het zeolietrooster te introduceren ter bevordering van het moleculair transport; zeker voor zeolieten met een één-dimensionale poriestructuur zoals mordenieten. Dit gaat echter ten koste van het aantal zure sites. In dit werk werden commerciële zure mordenieten bestudeerd en dit bracht een opmerkelijke heterogeniteit aan het licht. Zo werd er zowel tussen als in verschillende kristallen een zeer verschillende verdeling van zure sites, kristalroostertoegankelijkheid en katalytische activiteit waargenomen. Deze heterogeniteit werd niet waargenomen in stalen zonder voorafgaande dealuminatie, wat aantoont dat er tijdens de grootschalige industriële dealuminatie vermoedelijk grote variaties in procescondities aanwezig zijn (temperatuur, waterdruk, …). Verder toonden de gedetailleerde beelden een zekere ordening in de geïnduceerde porositeit aan die directe gevolgen heeft voor de katalytische activiteit. Zo vinden de meeste katalytische omzettingen steeds plaats in de originele microporiën, nabij de extra-framework poriën en het buitenoppervlak.

In een volgende stap van mijn doctoraatsproject (**hoofdstuk 4**) werd de structuur-activiteitrelatie bestudeerd voor H-ZSM-5. Deze zeoliet wordt courant gebruikt omwille van zijn vormselectiviteit, het kristalrooster bevat namelijk twee porietypes met licht verschillende grootte en geometrie. Uit

rapporten blijkt dat aromatische moleculen selectief adsorberen in de verschillende poriën. Met behulp van fluorescentiemicroscopie heb ik het effect hiervan op het katalytische proces bekeken. Hieruit blijkt dat de zuur-gekatalyseerde furfuryl alcohol oligomerisatie preferentieel in één van de twee poriestructuren plaatsvindt. Dit fenomeen wordt veroorzaakt door verschillen in polariteit binnenin de zeolietporiën. Door een reactiesolvent met verschillende polariteit te gebruiken kan de reactie gestuurd worden. Dit kan toegepast worden om katalytische reacties selectief in één van de twee microporiën te laten plaatsvinden.

In **hoofdstuk 5** heb ik de katalytische activiteit van individuele ZIF-8 kristallen bestudeerd aan de hand van fluorescentiemicroscopie. ZIF-8 is een metaal-organisch rooster dat van belang is voor bijvoorbeeld de productie van biodiesel, omdat het (trans)esterificatiereacties katalyseert. De oorsprong en locatie van de actieve sites zijn echter nog onderwerp van debat. Met behulp van fluorescentiemicroscopie ontdekte ik dat uitsluitend het buitenoppervlak en de roosterdefecten katalytische activiteit vertonen. Hierdoor wordt de katalysator niet efficiënt gebruikt. Om dit te voorkomen heb ik met succes de structuur geëtst met oliezuur om zo het massa transport in de kristallen te verhogen. Het nadeel is dat oliezuur zeer sterk adsorbeert op de katalytische sites en zo de katalytische activiteit uiteindelijk verlaagt.

Samenvattend heb ik fluorescentiemicroscopie toegepast om de structuur-activiteitrelatie in zeolieten en metaal-organische roosters te bestuderen. Op basis hiervan heb ik voorstellen geformuleerd om de katalytische activiteit te optimaliseren. De bekomen resultaten en de resulterende inzichten tonen aan dat fluorescentiemicroscopie een meerwaarde is voor het katalyseonderzoek dat kan bijdragen tot katalytische reacties.

LIST OF ABBREVIATIONS

2D	two-dimensional
3D	three-dimensional
CARS	coherent anti-Stokes scattering
CCD	charged-coupled device
CMOS	complementary metal–oxide–semiconductor
CLSM	confocal laser scanning microscopy
EFAl	extra-framework aluminum
FDA	fluorescein diacetate
FIB	focused ion-beam
FTIR	Fourier transform infrared
MAS	magic-angle spinning
MOF	metal-organic framework
NASCA	nanometer accuracy by stochastic chemical reactions
NMR	nuclear magnetic resonance
PALM	photo-activated localization microscopy
Ph	phenyl
PSF	point-spread function
RI	refractive index
SBR	signal-to-background ratio
SEM	scanning electron microscopy
SNR	signal-to-noise ratio
SRS	stimulated Raman scattering
STORM	stochastic optical reconstruction microscopy
STXM	scanning transmission X-ray microscopy
TGA	thermogravimetric analysis
WFM	wide-field fluorescence microscopy
ZIF-8	zeolitic imidazolate framework-8
ZSM-5	zeolite Socony Mobil–5

CHAPTER 1

Introduction

Abstract

This literature overview presents an introduction to the fluorescence microscopy and its application in catalysis research. It covers such topics as current position of optical microscopy in the toolbox of catalysis researcher, basics of fluorescence microscopy, super-resolution microscopy approach, and main methods to introduce fluorescent function to study catalytic materials. In the end on the introduction, the research aims are formulated and scope of the thesis is outlined.

CHAPTER 1 - INTRODUCTION

The importance of heterogeneous catalysts for contemporary chemical industry is hard to overestimate. They are widely applied in the chemical, food, pharmaceutical, automobile and petrochemical industries. Approximately, 90% of all industrial chemical processes use heterogeneous catalysts.[1] More novel applications of heterogeneous catalysts include the emerging areas such as fuel cells, green chemistry, and biorefining.[2] Both rational improvement of the performance of the traditionally employed catalysts and invention of new materials and processes for novel applications rely heavily on detailed characterization of catalyst properties. Typically, catalyst characterization techniques reveal individual properties of the catalyst, such as concentration of catalytic sites or distribution of porosity, which are typically ensemble-averaged over millions or billions of catalyst particles. To use the obtained insight for performance interpretation as well as improvements to the catalyst design, it is assumed that the catalyst batches are homogeneous in terms of properties at the level of individual particles. For example, the average concentration of acid sites in zeolite samples is typically estimated via ammonia sorption or probe-assisted Fourier transform infrared (FTIR) spectroscopy. The values obtained from these bulk techniques represent the average acid sites concentration for all particles in the sampled volume, but reveal no information about the acidity distribution between individual particles let alone inside an individual zeolite particle.

Besides detailed catalyst characterization, the performance of a catalyst also needs to be determined in the desired application. To obtain representative information, the envisioned process is mimicked at the laboratory scale. Typically, the catalytic activity is assessed using so-called bulk catalytic experiments followed by analysis of the reaction mixture by chemical characterization techniques such as gas chromatography, mass spectrometry, nuclear magnetic resonance spectroscopy and FTIR spectroscopy. Similarly to catalyst characterization, assumptions are to be made regarding the homogeneity of the particles within the population used for the experiment. Intrinsically, the state-of-the-art approach in catalysis research overlooks the potential heterogeneous distribution of catalytic activity between and within the individual particles.

The advent of sensitive microscopy techniques has enabled to spatio-temporally characterize catalyst properties. Depending on the particular technique, it is possible to study catalysts' individual properties, such as structure and composition, or retrieve molecular information related to the envisioned chemical process. The use of microscopic techniques to characterize catalysts' structure has strongly increased over the past decades with the improved availability and quality of electron microscopes now routinely enabling sub-nanometer resolution.[3] With scanning transmission electron microscopy even atomic resolutions can now be attained.[4] However, electron microscopy techniques typically require ultrahigh vacuum conditions, hampering measurement under industrially-relevant reaction conditions. As such they are obtaining ex-situ static information about the catalyst properties pre-use or post-mortem, and links to the catalysts performance are inferred indirectly. Additionally, for larger, micrometer-sized catalyst particles, electron microscopy and related techniques provide only surface-related information unless some advanced sectioning routines are applied. In contrast, optical microscopy techniques, and in particular fluorescence microscopy, are more sensitive for molecular species rather than structural catalyst properties and these species can be imaged throughout the whole catalyst particle in 3D, however at a much reduced resolution compared to electron microscopy. Optical microscopy enables routine imaging under atmospheric conditions and when taking special measures even samples at elevated pressures and temperatures can be studied. Fluorescence microscopy is the most sensitive type of optical microscopy enabling the detection of individual molecules under ideal conditions. Often the diffraction-limited spatial resolution of a few hundred nanometers, offered by optical microscopy is cited as being its strongest limitation. Recently however, several elegant solutions have been developed that circumvent the diffraction limit. These techniques are collectively named super-resolution techniques (see below).

1.1 FLUORESCENCE MICROSCOPY

After the absorption of light and excitation to a higher electronic energy level, a molecule may release part of this gained energy by relaxing to the ground state via emission of a new photon. This process typically occurs over a nanosecond time-scale and is called fluorescence. The energy and the wavelength of the adsorbed and emitted photons differ because part of the energy is lost via non-radiative relaxation. Therefore, the excitation and emission light can be spectrally discriminated enabling very sensitive detection. In fluorescence microscopy the fluorescent signal of molecules can be detected, yielding information not only about the location but also about the molecular identity. Because different molecules may have different spectral properties, it is possible to selectively excite and/or detect only molecules of interest through the use of optical filters. For research applications, fluorescence microscopy techniques and assays were mainly developed to investigate biomedical samples, such as cells, tissues or viruses, but over the last decade they are being employed to study heterogeneous catalysts.[5]

1.1.1 Diffraction-limited Methods

There are two fluorescence microscopy configurations that are widely used: wide-field fluorescence microscopy (WFM) and confocal laser scanning microscopy (CLSM). Both are used in the work presented in this thesis. **Figure 1.1** presents a schematic summary of both approaches.

In WFM, a light beam evenly and continuously illuminates a large area of the sample typically in the range of several hundreds of square micrometers; often the used light is monochromatic and originates from a laser source. The fluorophores in the illuminated area are excited and subsequently emit fluorescence, which is captured by a camera (either charged-coupled device (CCD) or complementary metal–oxide–semiconductor (CMOS)). Using this approach, images are obtained with a high speed, limited only by the camera frame-rate, currently up to about 70 full-frames per second for the most sensitive CCD cameras (512 x 512 pixels) and 100 full-frames per second for research-grade CMOS cameras (2048 x 2048 pixels). Such high speeds enable the use of WFM to investigate relatively fast chemical reactions and diffusion processes. To its disadvantage, WFM suffers from axial out-of-focus fluorescence, which reduces the signal-to-background ratio (SBR).

In CLSM, the excitation laser light is focused on a single diffraction-limited spot in the sample. The fluorescence generated in this spot is captured by a point detector e.g. photomultiplier tube, avalanche photodiode, or hybrid detectors. Besides obtaining very fast dynamic information of process happening in the focal spot down to the sub-microsecond time scale e.g. in fluorescence correlation spectroscopy, sample images can be obtained by scanning this illumination spot with respect of the sample. Such images can be obtained by either controlled step-wise scanning of the sample stage with respect of the stationary laser spot (stage scanning) or by scanning the focal spot inside a stationary sample (laser scanning). An adjustable pinhole blocks axial out-of-focus fluorescence from above and below the focal plane hence strongly enhancing the obtained contrast and axial resolution, giving a slightly improved lateral resolution and enabling 3D sectioning of the sample under study. While these features offer clear advantages over WFM with respect to image quality, CLSM is typically 70-fold slower than WFM.

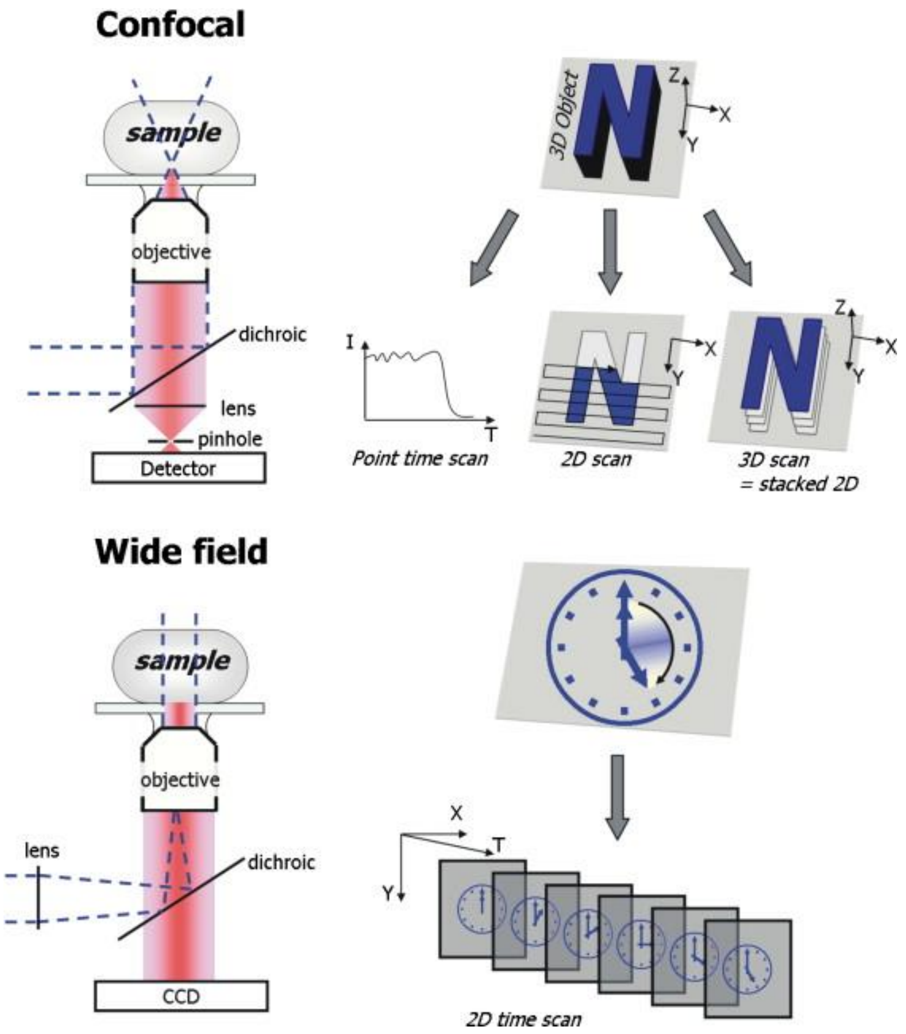

Figure 1.1. Schematic depiction of CLSM and WFM setups and approaches. In the CLSM approach, the collimated excitation light from the source is reflected by the dichroic mirror onto the objective lens. By overfilling the back aperture the light is then focused into a small spot. The fluorescence light is collected by the same objective lens and is transmitted by the dichroic mirror. In the WFM setup the collimated laser light is focused with a lens on the back aperture of the objective lens giving a collimated light beam illuminating the sample. The fluorescence generated by this area is then collected by the objective and passed through the dichroic mirror before touching the CCD camera. Reproduced with permission from M. B. J. Roeffaers, J. Hofkens, G. De Cremer, F. C. De Schryver, P. A. Jacobs, D. E. De Vos, B. F. Sels, *Catal. Today* **2007**, *126*, 44–53.[6]

Therefore, CLSM is less suited for imaging of dynamic processes, but offers clear advantages when studying larger 3D objects due to the customizable field of view.

Both techniques have a diffraction-limited spatial resolution defined by the Rayleigh criterion:

$$r = \frac{0.61\,\lambda}{n \times \sin\alpha} \text{ for WFM or}$$

$$r = \frac{0.43\,\lambda}{n \times \sin\alpha} \text{ for CLSM,}$$

where r, λ, n, and α denote the lateral resolution, the wavelength, the refractive index (RI) of the media, and the aperture angle of the lens.[7] The best research-grade modern lenses can collect light over a wide angle, $\alpha = 70°$, in combination with immersion oil of $n = 1.51$. This means that even under the best imaging conditions with visible light, the resolution is limited to about 0.31 λ (for CLSM) or 150 nm for visible light with $\lambda = 500$ nm. This renders fluorescence microscopy unsuitable for studies of the smallest submicron-sized catalyst particles, such as of industrially applied zeolites Y or ZSM-5.[8,9] In recent years, a host of super-resolution imaging techniques have been developed to overcome the diffraction limit; the inventors of these techniques were awarded the Nobel Prize in Chemistry 2014.[10] These super-resolution techniques can be subdivided in two groups of which I will focus in this chapter on one group – the single-molecule localization approaches. While the collected fluorescence signal of a single molecule in far field is inherently diffraction-limited in size, mathematical fitting of the recorded intensity distribution enables precise localization of the individual fluorescent molecule with nanometer precision. This approach only works if one can assume the recorded intensity to result from one individual emitting fluorophore. Practically, the intensity distribution of individual fluorophores can nowadays be routinely collected in WFM and localization-based methods such as stochastic optical reconstruction microscopy (STORM) and photo-activated localization microscopy (PALM) have found wide application in biomedical research over the past decade.[11,12] This particular approach is also ideally suited to study catalytic activity at the single particle level under realistic conditions.[6,13] Specifically, the conversion of a non-fluorescent (fluorogenic) reagent molecule into a fluorescent product molecule with single turnover sensitivity is used to identify the location of catalytic activity at the nanoscale. To link this local information on catalytic activity with the catalyst properties at the relevant length scales electron microscopy or Raman microscopy can be used.

1.1.2 Super-resolution Localization Microscopy

Super-resolution localization fluorescence microscopy techniques rely on creating the conditions in which fluorophores can be localized individually with precision higher then diffraction limit. To achieve this, fluorophores need to be separated from each other spatially and temporally. Typically localization fluorescence microscopy techniques control the concentration and quantum state of fluorophores to achieve the situation that in any given WFM frame the diffraction-limited fluorescence intensity spots, or point-spread functions (PSFs), produced by individual fluorophores do not overlap. After WFM imaging, the acquired frame sequences are analyzed one-by-one to localize the positions of each individual fluorophore with nanometer precision by fitting the experimental PSF most frequently to a 2D Gaussian function (**Figure 1.2**). The precision of this mathematical localization depends on the numerous experimental parameters, such as emission wavelength, the numerical aperture of the objective, the efficiency of the optical system, the emission rate of the single molecule, the acquisition time, total amount of emitted photons, camera parameters, molecular orientation of the fluorophore, SBR, and signal-to-noise ratio (SNR).[14,15] For typical experiments, precisions down to 10-20 nm can nowadays be obtained.[16–18]

In this thesis, nanometer accuracy by stochastic chemical reactions (NASCA) microscopy is prominently used.[19,20] It is a localization based super-resolution technique which is specifically designed to monitor chemical reactions at the single-molecule level in real time. It uses the fluorogenic chemical reactions – conversions of a non-fluorescent precursor into a strong fluorophore. These individual fluorophores captured in WFM images report on the local catalytic activity. To enable nanoscale activity imaging, an equilibrium between the creation of novel fluorophores and their subsequent removal is necessary to prevent the accumulation of background fluorescence and to maintain fluorophore concentrations low enough for the florescent products to not overlap. While fluorophores are created via fluorogenic reaction, they are removed from fluorophores population in focal volume via photobleaching, diffusion, or further chemical transformation.

Similar to other super-resolution localization fluorescence microscopy techniques the fluorophores should have high extinction coefficients and quantum yields of fluorescence and there should be low fluorescence background from reagent, catalyst, solvent, or reaction side products at the used excitation wavelength.

Satisfaction of these conditions allows spatio-temporal resolution of individual fluorescent products, and therefore the acts of fluorogenic reaction. Subsequently, individual fluorescent products are localized individually, in the same way as in STORM and PALM (**Figure 1.2**). The obtained localizations are reconstructed as 2D-accumulated histograms in this thesis, representing the activity map of the sample.

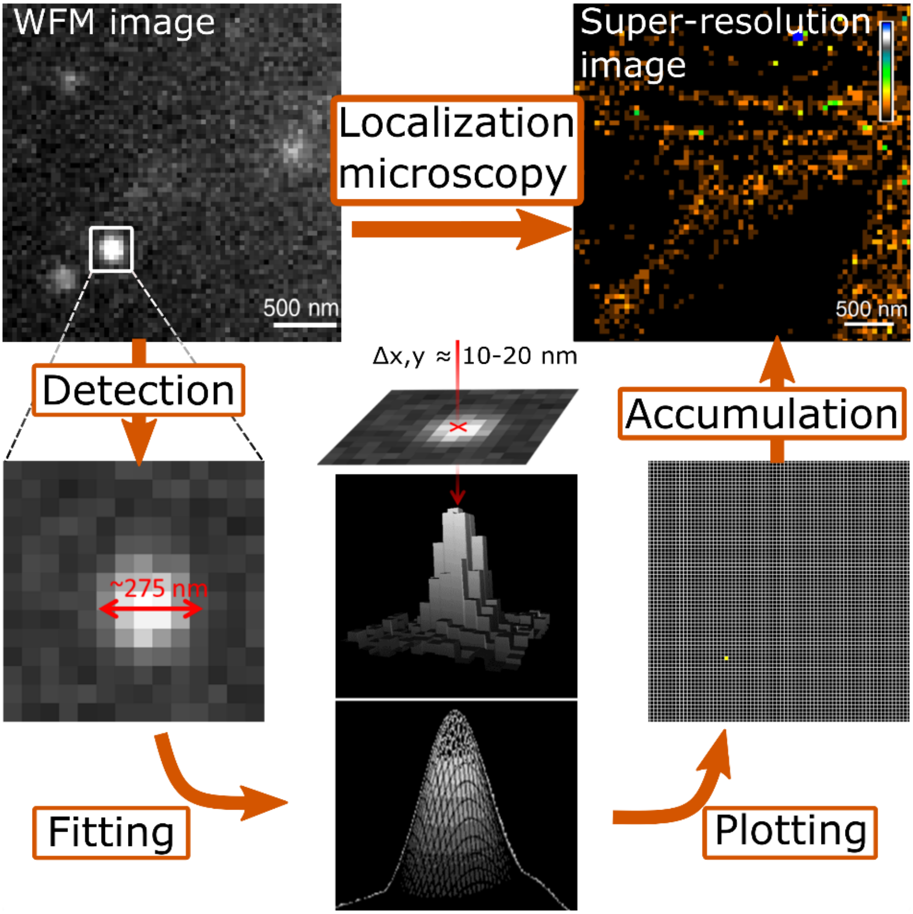

Figure 1.2. Schematic representation of the super-resolution localization fluorescence microscopy approach (STORM, PALM, NASCA). Individual fluorophores are detected on the WFM single frame image. Then their PSFs are fitted, typically with 2D Gaussian distribution, with a precision higher than diffraction limit. Subsequently, fluorophores localized in numerous frames are plotted as 2D histogram, which represents super-resolution image of fluorophores density (PALM, STORM) or catalytic activity distribution (NASCA).

1.2 FLUORESCENCE MICROSCOPY STUDIES OF HETEROGENEOUS CATALYSTS

Many heterogeneous catalysts do not intrinsically absorb light in the visible wavelength range and hence do not fluoresce, creating virtually no background and enabling excitation of fluorophores contained insight the catalyst. On the other hand, as the heterogeneous catalyst itself is not observed, the fluorescence image does not generate any context to the recorded signals. Often complementary structural imaging and identification via electron or optical transmission microscopy is necessary to rationalize the fluorescence imaging data. As described above, fluorogenic reactions can be used to map out the catalytic activity itself. Additionally, fluorescent molecules can be used to probe structural and chemical properties of the catalyst (**Figure 1.3**).

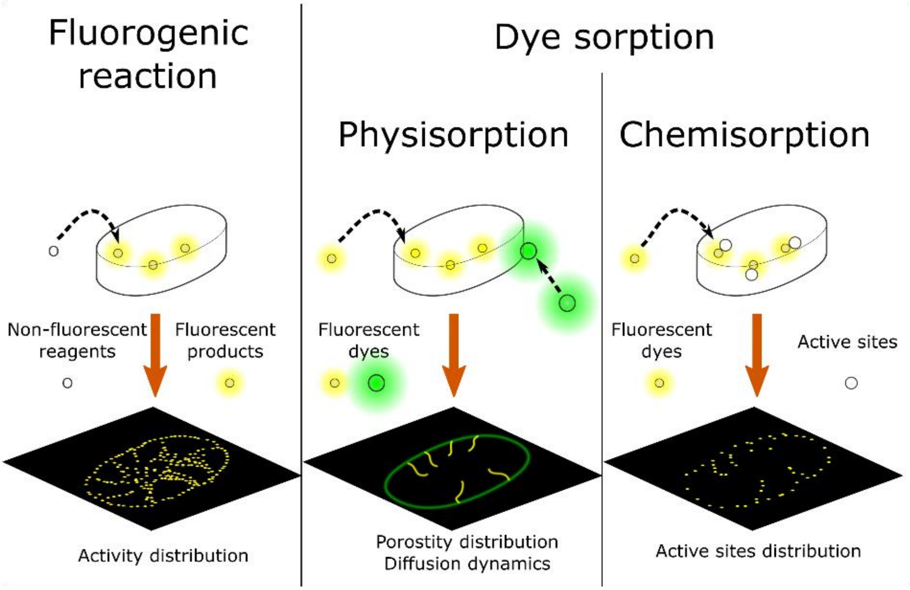

Figure 1.3. Schematic representation of two major approaches to introduce fluorescence into catalysts. In fluorogenic reaction, non-non fluorescent reagents diffuse inside catalyst crystal and are catalytically converted into fluorescent products, which are detected to uncover catalytic activity distribution. Fluorescent dyes can either physisorb, giving the information about porous structure and diffusion parameters, or chemisorb on catalytically active sites, uncovering their distribution.

Physisorption of intrinsically fluorescent dyes can be used to probe the pore accessibility as well as the mass transfer inside catalyst particles. Secondly, chemisorption of functional dyes at the catalytically active sites allows to probe site distribution, density and accessibility. As a result, fluorescence microscopy is used to study differences in catalyst properties via (selective) dye sorption, and in catalytic activity via fluorogenic reaction. Due to the already mentioned low background, fluorescence microscopy provides higher contrast and specificity in these studies than optical microscopy. Moreover, fluorescence microscopy can be also implemented in the super-resolution regime. Sharp contrast and high resolution in combination with excellent molecular sensitivity and specificity make fluorescence microscopy well suited for single catalytic particle characterization.

For concrete examples of applications of fluorescent microscopy techniques in catalysis research I refer the reader to several comprehensive reviews, focused in particular on fluorescence microscopy methods which are available for catalysis research,[21] on heterogeneities in catalyst properties uncovered with fluorescence microscopy and spectroscopy techniques,[22] on applications of single-molecule microscopy methods for catalysis research,[23] and on super-resolution imaging of surface reactions.[24]

In summary, fluorescence microscopy is uniquely suited to investigate numerous catalysts properties at single-crystal and single-molecule level. In recent years, local distribution of such properties as catalytic activity, active sites concentration, and porosity has been studied at different length-scales (nano- and micrometer) and in different materials (zeolites, MOFs, metal oxides, and metal nanoparticles).[21–24]

Furthermore, fluorescence microscopy can also be combined with other advanced techniques in the same setup, such as scanning electron microscopy (SEM), optical coherence microscopy, atomic force microscopy, or Raman microscopy.[25–28] This allows to establish the structure-activity relationship at the single-crystal, single-molecule level, typically unachievable for classical, ensemble-based, material characterization techniques.

1.3 SCOPE AND OUTLINE

Catalytic performance is typically defined as combination of catalytic activity, i.e. how much the catalyst can accelerate the reaction, and catalytic selectivity, i.e. how much the catalyst can promote desired reaction over side reactions. Both catalytic activity and catalytic selectivity are highly dependent on catalyst porosity. Smaller micropores provide spatial restrictions around active sites and enable selectivity based on molecular dimensions of reagents and products while larger meso- and macropores provide molecular highways and increase molecular transport throughout catalyst crystal. As a result, the local spatial distribution of porosity plays central role in affecting the catalytic performance, and fluorescence microscopy is well-suited to uncover that role. The main goal of this thesis is to apply fluorescence microscopy methods to investigate the interplay between local catalytic performance and catalyst porosity, whether inherent or introduced by post-synthetic procedures.

In first case study, I focused on the effect which post-synthetic extra-framework porosity introduction has on catalytic performance of mordenite zeolites. Mordenite zeolites are commonly used in petrochemical processes, but usually after they undergo post-synthetic dealumination. However, dealumination is a careful balancing act between introducing extra-framework mesopores and removing aluminum. Extra-framework mesopores introduction enhances catalytic activity by promoting molecular diffusion, but aluminum removal decreases the activity by removing catalytically active acid sites. Additionally, if catalytic reaction happens excessively in the mesopores, it can disrupt catalytic selectivity due to the lack of spatial restrictions. **Chapters 2 and 3** of this thesis describe my experiments to determine the effects of dealumination on the following catalyst properties of acid mordenite zeolites – distribution of the acid sites, extra-framework porosity, and catalytic performance.

In the second case study, I focus on catalytic selectivity in ZSM-5 zeolites, provided by its inherent micropores. Acid ZSM-5 zeolites have two micropore subsystems of different size and geometry. The differences between these pore sizes could potentially be used to fine-tune shape-selective catalytic processes. **Chapter 4** is an account of my attempts to use solvents of different polarities to affect the pore preference of catalysis in ZSM-5 catalysts and force the reaction to selectively occur within either one or another micropore subsystem.

In last case study, reported in **Chapter 5**, I study the spatial distribution of base catalytic activity of ZIF-8 MOF. ZIF-8 is a promising catalyst for catalytic transesterification of bio-based oils, but it is expected to have only surface-limited catalytic activity in this process. I observe predicted surface-limited catalytic activity and attempt to introduce extra-framework pores to circumvent it.

Lastly, in **Chapter 6**, the conclusions of this work are formulated, new research trends are highlighted and potential for future work is outlined.

1.4 REFERENCES

[1] *Catalysis Looks to the Future*, National Academies Press, Washington, D.C., USA, **1992**.

[2] G. Ertl, H. Knözinger, F. Schüth, J. Weitkamp, Eds., *Handbook of Heterogeneous Catalysis*, Wiley-VCH, Weinheim, Germany, **2008.**

[3] J. W. Niemantsverdriet, *Spectroscopy in Catalysis*, Wiley-VCH, Weinheim, Germany, **2007**.

[4] T. Altantzis, E. Coutino-Gonzalez, W. Baekelant, G. T. Martinez, A. M. Abakumov, G. Van Tendeloo, M. B. J. Roeffaers, S. Bals, J. Hofkens, *ACS Nano* **2016**, *10*, 7604–7611.

[5] K. P. F. Janssen, G. De Cremer, R. K. Neely, A. V. Kubarev, J. Van Loon, J. A. Martens, D. E. De Vos, M. B. J. Roeffaers, J. Hofkens, *Chem. Soc. Rev.* **2014**, *43*, 990–1006.

[6] M. B. J. Roeffaers, J. Hofkens, G. De Cremer, F. C. De Schryver, P. A. Jacobs, D. E. De Vos, B. F. Sels, *Catal. Today* **2007**, *126*, 44–53.

[7] U. Kubitscheck, *Fluorescence Microscopy*, Wiley-VCH, Weinheim, Germany, **2013**.

[8] F. C. Meunier, D. Verboekend, J.-P. Gilson, J. C. Groen, J. Pérez-Ramírez, *Microporous Mesoporous Mater.* **2012**, *148*, 115–121.

[9] P. A. Jacobs, P. J. A. Maes, S. J. Paulussen, M. Tielen, D. F. E. Van Steenkiste, L. K. Van Looveren, **1998**, *US Patent 6229032 B1*.

[10] The Royal Academy of Swedisch Sciences, *"Super-resolved fluorescence microscopy"* **2014**.

[11] C. Coltharp, J. Xiao, *Cell. Microbiol.* **2012**, *14*, 1808–1818.

[12] S. W. Hell, S. J. Sahl, M. Bates, X. Zhuang, R. Heintzmann, M. J. Booth, J. Bewersdorf, G. Shtengel, H. Hess, P. Tinnefeld, et al., *J. Phys. D. Appl. Phys.* **2015**, *48*, 443001.

[13] E. Betzig, G. H. Patterson, R. Sougrat, O. W. Lindwasser, S. Olenych, J. S. Bonifacino, M. W. Davidson, J. Lippincott-Schwartz, H. F. Hess, *Science* **2006**, *313*, 1642–1645.

[14] R. J. Ober, S. Ram, E. S. Ward, *Biophys. J.* **2004**, *86*, 1185–1200.

[15] J. Engelhardt, J. Keller, P. Hoyer, M. Reuss, T. Staudt, S. W. Hell, *Nano Lett.* **2011**, *11*, 209–213.

[16] Z. Ristanović, A. V. Kubarev, J. Hofkens, M. B. J. Roeffaers, B. M. Weckhuysen, *J. Am. Chem. Soc.* **2016**, *138*, 13586–13596.

[17] J. Lippincott-Schwartz, G. H. Patterson, *Trends Cell Biol.* **2009**, *19*, 555–565.

[18] P. Lemmer, M. Gunkel, Y. Weiland, P. Müller, D. Baddeley, R. Kaufmann, A. Urich, H. Eipel, R. Amberger, M. Hausmann, et al., *J. Microsc.* **2009**, *235*, 163–171.

[19] M. B. J. Roeffaers, G. De Cremer, J. Libeert, R. Ameloot, P. Dedecker, A. J. Bons, M. Buckins, J. A. Martens, B. F. Sels, D. E. De Vos, et al., *Angew. Chem. Int. Ed.* **2009**, *48*, 9285–9289.

[20] M. B. J. Roeffaers, B. F. Sels, H. Uji-I, F. C. De Schryver, P. A. Jacobs, D. E. De Vos, J. Hofkens, *Nature* **2006**, *439*, 572–575.

[21] G. De Cremer, B. F. Sels, D. E. De Vos, J. Hofkens, M. B. J. Roeffaers, *Chem. Soc. Rev.* **2010**, *39*, 4703–4717.

[22] I. L. C. Buurmans, B. M. Weckhuysen, *Nat. Chem.* **2012**, *4*, 873–886.

[23] K. P. F. Janssen, G. De Cremer, R. K. Neely, A. V. Kubarev, J. Van Loon, J. A. Martens, D. E. De Vos, M. B. J. Roeffaers, J. Hofkens, *Chem. Soc. Rev.* **2014**, *43*, 990–1006.

[24] T. Chen, B. Dong, K. Chen, F. Zhao, X. Cheng, C. Ma, S. Lee, P. Zhang, S. H. Kang, J. W. Ha, et al., *Chem. Rev.* **2017**, DOI 10.1021/acs.chemrev.6b00673.

[25] N. Liv, C. A. Zonnevylle, A. C. Narvaez, A. P. J. Effting, P. W. Voorneveld, M. S. Lucas, J. C. Hardwick, R. A. Wepf, P. Kruit, J. P. Hoogenboom, *PLoS One* **2013**, *8*, DOI 10.1371/journal.pone.0055707.

[26] E. Debroye, J. Van Loon, X. Gu, T. Franklin, J. Hofkens, K. P. F. Janssen, M. B. J. Roeffaers, *Part. Part. Syst. Charact.* **2016**, *33*, 412–418.

[27] C. Berclaz, C. Pache, A. Bouwens, D. Szlag, A. Lopez, L. Joosten, S. Ekim, M. Brom, M. Gotthardt, A. Grapin-Botton, et al., *Sci. Rep.* **2015**, *5*, 10385.

[28] W.-C. Lin, C. D. Blanchette, T. V. Ratto, M. L. Longo, *Biophys. J.* **2006**, *90*, 228–237.

CHAPTER 2

Rationalizing inter- and intracrystal heterogeneities in dealuminated acid mordenite zeolites by stimulated Raman scattering microscopy correlated with super-resolution fluorescence microscopy

Kuan-Liu Liu,* **Alexey V. Kubarev**,* Jordi Van Loon, Hiroshi Uji-I, Dirk E. De Vos, Johan Hofkens, Maarten B. J. Roeffaers

Adapted with permission from: *ACS Nano* **2014**, *8*, 12650–12659

* Joint first authors

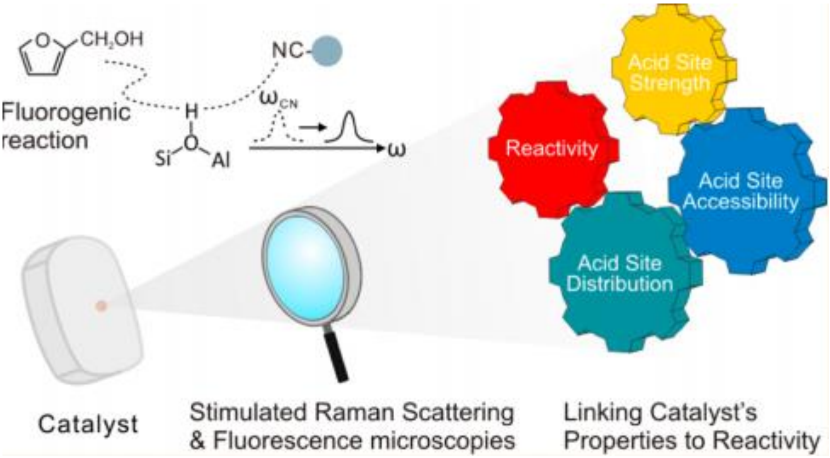

Abstract

Dealuminated zeolites are widely used acid catalysts in research and the chemical industry. Bulk-level studies have revealed that the improved catalytic performance results from an enhanced molecular transport as well as from changes in the active sites. However, fully exploiting this information in rational catalyst design still requires insight in the intricate interplay between both. Here we introduce fluorescence and stimulated Raman scattering microscopy to quantify subcrystal reactivity as well as acid site distribution and to probe site accessibility in the set of individual mordenite zeolites. Dealumination effectively introduces significant heterogeneities between different particles and even within individual crystals. Besides enabling direct rationalization of the nanoscale catalytic performance, these observations reveal valuable information on the industrial dealumination process itself.

http://pubs.acs.org/doi/full/10.1021/nn505576p

Modifications:

- Figures and tables numeration was adjusted to match the thesis.
- Figure 7 caption was corrected from “SRS microspectroscopy and polarization dependence of PhCN adsorbed in SP-MOR.” to “SRS microspectroscopy and polarization dependence of PhCN adsorbed in H-MORs.”
- Following phrase was corrected from “Since PhCN is a stronger base than CD$_3$CN, the C≡N stretches of 2249 and 2237 cm^{-1} are assigned to the PhCN interacting Brønsted acid framework silanol groups and weaker EFAl species, respectively.” to “Since PhCN is a stronger base than CD3CN, the C≡N stretches of 2249 and 2237 cm–1 are assigned to the PhCN interacting with Brønsted acid framework groups and weaker EFAl species, respectively.”

Contributions

The main part of the experimental work related to fluorescence microscopy and article writing was performed by Alexey Kubarev. Kuan-Lin Liu performed the Raman microspectroscopy measurements and related analysis. Maarten Roeffaers, Alexey Kubarev, and Kuan-Lin Liu conceived the project. All authors were involved in data interpretation and article writing.

CHAPTER 2 – RATIONALIZING INTER- AND INTRACRYSTAL HETEROGENEITIES IN DEALUMINATED ACID MORDENITE ZEOLITES BY STIMULATED RAMAN SCATTERING MICROSCOPY CORRELATED WITH SUPER-RESOLUTION FLUORESCENCE MICROSCOPY

2.1 INTRODUCTION

Zeolites are porous crystalline solids with pores of molecular dimensions, providing size and shape selectivity in catalysis.[1-4] Acid mordenites (H-MORs) are typical catalysts used in the petrochemical industry, mostly for cracking, isomerization, and alkylation reactions. The Brønsted acidic framework hydroxyls are lining the porous network that consists of main channels (6.5×7.0 Å^2) and small channels (5.7×2.6 Å^2) oriented along the crystallographic c-axis with side pockets (3.4×4.8 Å^2) along the b-axis. The side pockets are too small for most organic molecules, resulting in a quasi-unidirectional microporous system that makes as-synthesized H-MOR susceptible to mass transport limitations and rapid deactivation.[5,6] Optimization of the catalytic performance often relies on postsynthetic treatments such as dealumination that reduces the framework aluminum content and also introduces mesoporosity, thus enhancing molecular transport and slowing the deactivation by coke formation. Typically, dealumination involves repeated chemical (e.g., acid leaching) and hydrothermal (steaming) treatments that have complex implications on both compositional and structural properties, such as acid site density, accessibility, pore network, etc.[7,8] Currently, optimization of H-MOR performance and of catalysts in general is largely based on trial-and-error experiments using bulk catalyst samples, without much insight at the relevant length scales since tools capable of looking beyond the crystal surface and providing relevant information with high sensitivity and spatial resolution are not available.[9-11]

Recently, 3D nanoscale reactivity mapping of catalytic reactions in zeolite catalysts has become possible via single-molecule spectroscopy.[12] NASCA microscopy captures single catalytic conversions of fluorogenic molecules and determination of the local nanoscale reactivity results from accurate fitting and mapping of the recorded emission from individual fluorescent reaction products.[13,14] In-depth rationalization of this spatially resolved catalytic performance information was so far not possible because of a lack of complementary techniques in the current catalyst characterization toolbox. Highly specialized scanning transmission X-ray microscopy (STXM) has been proven to generate very detailed chemical composition maps;[15] it provides information on local aluminum content and its coordination in dealuminated zeolites, allowing a rationalization of catalytic performance.[16,17] Moreover, chemical maps obtained from STXM are not limited to aluminum, but they also allow measuring spatial distribution of the other elements, such as carbon in probe molecules, allowing investigation of the acid sites.[18] Infrared spectroscopy using organic probe molecules is routinely applied to characterize acid zeolites, as well, but this technique does not offer the required 3D spatial resolution.[19] Closely related Raman microscopy offers this resolution, but it is much less used because of the strongly interfering background fluorescence and because of the inherently weak signals.[20,21] Various enhancement methods have been developed for Raman spectroscopy over the years, of which coherent Raman scattering seems to offer most advantages for 3D catalyst characterization. As an example, coherent anti-Stokes scattering (CARS) microspectroscopy has been applied to record the density map of thiophene in individual H-ZSM-5 crystals[22] and to follow the catalytic conversion of alkene and glycol in single H-Beta crystals, which provides one with important insights about catalysis, such as reaction pathways and activation energy.[23] However, the non-resonant background inherently distorts the CARS spectrum, requiring complex mathematical treatments to extract quantitative information.[24] The development of stimulated Raman scattering (SRS) microscopy offers an unprecedented capability of fast molecular imaging.[25,26] Unlike the more often used CARS, the SRS signal is free from non-resonant background, thus enabling straightforward quantitative and qualitative analyses without assumptions and data interpretation. Here we show how the complex inter- and intraparticle heterogeneities in catalytic performance observed for dealuminated H-MOR in NASCA microscopy (**Figure 2.1A**) can be rationalized by local acid site density and accessibility obtained from SRS microscopy using nitrile probes (**Figure 2.1B**). The described method is straightforward and can be widely used in heterogeneous catalysis.

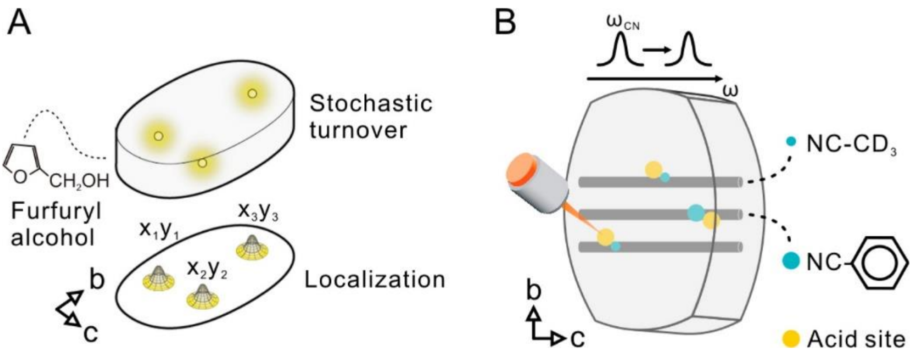

Figure 2.1. Schematic representation of the used optical micro(spectro)scopic assay. (A) NASCA and (B) SRS microscopy.

2.2 RESULTS AND DISCUSSION

Three synthetic mordenite samples with typical crystal dimensions of 5–10 μm were used in the present study; the parent small-port mordenite has a bulk Si/Al = 6.2 (SP-MOR);[8,27-30] starting from this material, the two other mordenite samples are produced via mild (Si/Al = 11; mildly dealuminated MD-MOR) and strong (Si/Al = 65; strongly dealuminated SD-MOR) dealumination by one of several cycles of steaming and subsequent acid leaching as described by Hamon et al.[31]

2.2.1 **NASCA Microscopy**

To investigate the effect of the dealumination process on the catalytic performance at the individual crystal level, NASCA microscopy with furfuryl alcohol (FFA) as a fluorogenic reactant was chosen (**Figure 2.1A, Figure 8.1**); based on the crystal structure of mordenite, FFA fits inside the micropores.[13,32-34] **Figure 2.2A** reveals that the catalytic activity of non-dealuminated SP-MOR is limited to the outer surface of the crystal. This is visual evidence of the so-called small-port behavior hindering access of FFA to the microporous network, which was already demonstrated at the bulk level for many synthetic and natural mordenites.[27,28] In addition to this direct visual observation, quantitative analysis of the local reaction rate determined for $500 \times 500 \times 800$ nm^3 voxels (see Supporting Information) reveals a clear bimodal distribution for the presented SP-MOR crystal with active regions at the crystal periphery that have an activity of $2.6 \pm 0.1 \times 10^{-10}$ M·s^{-1}, whereas parts of the crystal away from the surface have no measurable catalytic activity (**Figure 2.2F**).

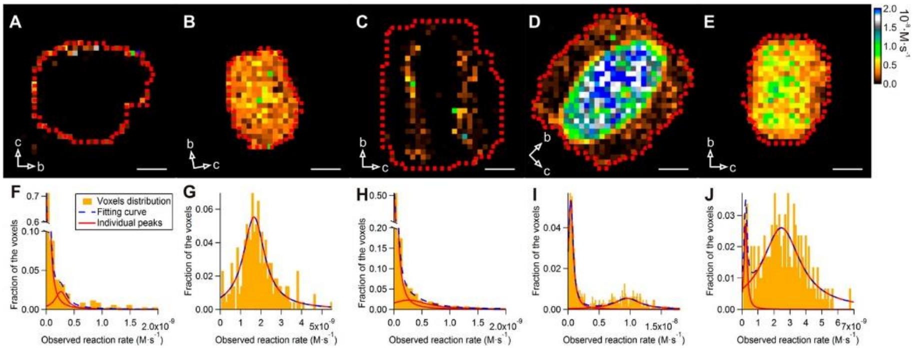

Figure 2.2. Quantitative analysis of NASCA reactivity maps obtained for 500 × 500 × 800 nm^3 voxels (XYZ). (A) SP-MOR crystal; (B) SD-MOR crystal; (C–E) MD-MOR crystals at different stages of dealumination. Red dashed line indicates the region used for histogram analysis; false color scale indicates observed reaction rate (from 0 to 2 × 10^{-8} M·s^{-1}); crystal axes are indicated by arrows; scale bar: 3 μm. (F–J) Histograms of measured reactivity fitted with single, double, or triple Lorentzian curve as dashed blue line (for parameters, see **Table 2.S1**): (F) SP-MOR crystal (presented in A); (G) SD-MOR crystal (presented in B); (H) MD-MOR crystal (presented in C); (I) MD-MOR crystal (presented in D); (J) MD-MOR crystal (presented in E).

Within measured 14 crystals from this batch, no substantial variation in catalytic performance is found. Compared to SP-MOR, severely dealuminated SD-MOR crystals (n = 27) are fully accessible for furfuryl alcohol, showing a homogeneous activity of 16.6 ± 0.4 × 10^{-10} M·s^{-1} throughout the whole crystal volume (**Figure 2.2B,G**). The presence of only one peak in the activity histogram, at least at the scale of analysis which is 500 × 500 × 800 nm^3, reflects an efficient pore opening by the dealumination process, that is, transition to large-port mordenite for the whole crystal volume.[35] Surprisingly, and in contrast to SP-MOR and SD-MOR, crystals from the mildly dealuminated MD-MOR sample show a pronounced intercrystal heterogeneity in their reactivity distribution; the crystals from this sample can be divided into three types. About 33% of the crystals (n = 38) display some activity at the outer region of the crystal (2.6 ± 0.6 × 10^{-10} M·s^{-1}) and no catalytic activity at the crystals' center (**Figure 2.2C,H**). A second group (25%, n = 29) displays the inverse behavior with a highly active core (95 ± 3 × 10^{-10} M·s^{-1}) and a zone of about 3 μm at the periphery of the crystals with a much lower activity of 4.3 ± 0.1 × 10^{-10} M·s^{-1} (**Figure 2.2D,I**). Thirty-three crystals in MD-MOR (28%) show a transitional behavior between crystals in the just described second group and those with homogeneous reactivity observed in SD-MOR as these crystals still show a bimodal activity distribution (**Figure 2.2E,J**) with peak positions at 2.3 ± 0.2 × 10^{-10} for the periphery and 24 ± 1 × 10^{-10} M·s^{-1} for the center, but the difference in catalytic activity between the peaks is, however, significantly smaller than for the second group. Finally, 14% (n = 16) of the crystals show transitional behaviors between the aforementioned groups and, therefore, were not assigned to one of them.

2.2.2 SRS Microscopy

The remarkable heterogeneities in reactivity observed in the NASCA experiments are the result of acid site distribution as well as of the molecular accessibility. Since none of the classical characterization tools allows studying these zeolite properties at the relevant subcrystal level, we resort to highly sensitive and spatially resolved chemical imaging by SRS microscopy in combination with nitrile probes (**Figure 2.1B**). Bulk infrared spectroscopy has shown that small deuterated acetonitrile (CD_3CN) molecules effectively access all Brønsted acid sites in both small- and large-port H-mordenites, whereas the bulkier benzonitrile (PhCN) allows discrimination of large-port from small-port behavior.[35-37] **Figure 2.3** presents the density map of adsorbed CD_3CN in three H-MOR samples, obtained from chemical mapping as well as spectral analysis (see below).

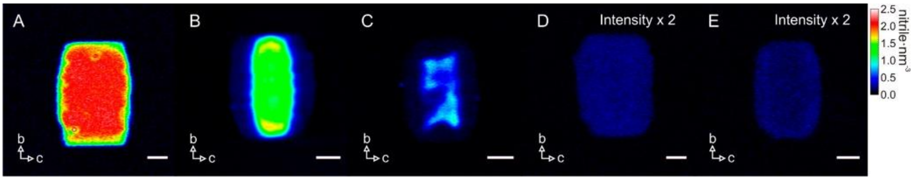

Figure 2.3. Chemical mapping of CD_3CN adsorbed in H-MORs. (A) SP-MOR; (B–D) MD-MOR crystals at different stages of dealumination: (B) early, (C) intermediate, and (D) late stages; (E) SD-MOR. False color scale indicates the acid site density (from 0 to 2.5 nitrile·nm^{-3} for A–C and from 0 to 1.25 nitrile·nm^{-3} for D,E); crystal axes are indicated by arrows; scale bar: 3 μm.

Inside SP-MOR crystals (**Figure 2.3A**), CD_3CN is distributed homogeneously and the C≡N stretch is shifted by 10 cm^{-1} to 2275 cm^{-1} as compared to liquid CD_3CN (**Figure 2.4A**). To gain insight into the orientation of adsorbed nitriles, the polarization dependence of the SRS response was examined. **Figure 2.4B,C** depicts the relative C≡N stretch intensity at 2275 cm^{-1} of CD_3CN adsorbed in the SP-MOR along the crystallographic *ac* and *bc* planes as a function of angle θ between laser polarization and the crystallographic *b*-axis.

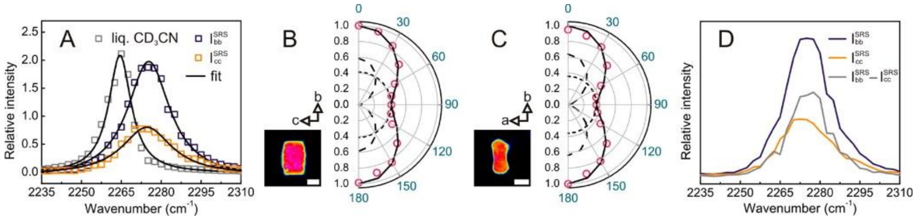

Figure 2.4. SRS microspectroscopy and polarization dependence of CD_3CN adsorbed in SP-MOR. (A) SRS response of the C≡N stretch region of liquid CD_3CN (×0.2) and of CD_3CN adsorbed in SP-MOR (averaged over a whole crystal) recorded with lasers polarized in crystallographic *b*- (I_{bb}^{SRS}) and *c*-axes (I_{cc}^{SRS}); spectra are fitted by a single Lorentzian curve (solid line). (B,C) Polar plot for C≡N stretch (2275 cm⁻¹) in SP-MOR crystals with different crystal orientations shown in the insets as a function of θ (angle between laser polarization and crystallographic *b*-axis); the polar plots can be simulated by the sum (solid line) of a $\cos^2 \theta$ function (anisotropic component, dashed line) and a circle (isotropic component, dotted line); scale bar: 5 μm. (D) Spectra for the anisotropic ($I_{bb}^{SRS} - I_{cc}^{SRS}$) and the isotropic ($I_{cc}^{SRS}$) components in the C≡N vibration.

A uniaxial symmetry is observed with the signal about 2.3 times higher when the lasers are polarized in the crystallographic *b*-axis than in either the *a*- or *c*-axis, indicating that a fraction of nitriles is symmetrically oriented with respect to the crystallographic *b*-axis. These polar plots can be simulated by a sum of two components, an isotropic (circle) and an anisotropic component ($\cos^2 \theta$), with the latter oriented along the crystallographic *b*-axis (**Figure 2.S1**). Theoretical calculation by Dominguez-Soria et al. suggested that part of the CH_3CN adsorbed in H-MOR is confined in the side pocket, with its C≡N bond parallel to the crystallographic *b*-axis, to access acid sites in the side pockets; CD_3CN molecules are tilted and become rather randomly distributed to interact with acid sites in the 12-membered ring channels.[38] Therefore, the anisotropic and isotropic components can be assigned to CD_3CN interacting with acid sites in the side pocket and main channel, respectively. Here we introduce I_{kl}^{SRS} to denote the SRS response obtained with pump and Stokes beams polarized in the *k* and *l* directions, respectively. When both lasers are polarized along the *a* or *c*-axis, only the isotropic component contributes to SRS response (I_{cc}^{SRS} or I_{aa}^{SRS}), whereas both components are present with lasers polarized along the crystallographic *b*-axis (I_{bb}^{SRS}). The spectral response of CD_3CN interacting with acid sites in the side pocket, approximated by $I_{bb}^{SRS} - I_{cc}^{SRS}$, is similar to that of CD_3CN in the main channel (**Figure 2.4D**).

Taking advantage of the linear concentration dependence of the SRS signal, one can evaluate the absolute local density of adsorbed CD_3CN by comparing its signal intensity with that of liquid CD_3CN with known molecular density

(10.8 nm^{-3}). In contrast to the isotropic distribution of CD_3CN in the main channels, the highly oriented CD_3CN in the side pockets leads to a uniaxial symmetry of the SRS response in the focal volume. The measured intensity thus contains mixed information about oscillator density and molecular orientation. An orientation-independent Raman spectrum of adsorbed CD_3CN should be obtained before quantitatively comparing the integrated C≡N stretch intensity with its liquid counterpart. In brief, the orientation-independent spectrum can be obtained from a linear combination of two SRS spectra recorded with lasers polarized along the crystallographic *b*- and *c*-axes and normalized for the laser power (detailed information on the local CD_3CN quantification can be found in the Supporting Information). Similarly, the nitrile density map can be reconstructed using a linear combination of two single-frequency SRS images recorded at the peak of the C≡N stretch along the crystallographic *b*- and *c*-axes. The resulting chemical map (**Figure 2.3**) is orientation-independent, assuming constant bandwidth, and after laser power normalization, the scale is calibrated with that of liquid CD_3CN.

For the investigated SP-MOR crystals (n = 19), an average density of 1.81 ± 0.11 nm^{-3} was found matching the expected framework aluminum density. Since the SRS response can be decomposed in an isotropic component (I_{cc}^{SRS}) and an anisotropic component ($I_{bb}^{SRS} - I_{cc}^{SRS}$) representing CD_3CN interacting with acid sites in the main channel and in the side pocket, respectively, the integrated spectral peak intensity reveals their relative abundance in a single-crystal or subcrystal region (see Supporting Information). For SP-MOR, a ratio of 0.37 ± 0.05 can be calculated, which is similar to the 1:3 ratio recently reported by Huo et al. based on bulk nuclear magnetic resonance (NMR) spectroscopy.[39]

For MD-MOR, with an average acid site density of 0.31 nm^{-3} (total = 13), heterogeneous acid site distributions within individual particles and varying total acid site densities among different crystals are observed (**Figure 2.3B–D**). Based on the total acid site density per crystal, a significant intraparticle heterogeneity is uncovered for the first time; similar to the NASCA results, crystals can be divided into three groups representing a gradual transition from SP-MOR toward SD-MOR behavior: early (>0.40 nm^{-3}), intermediate (0.40–0.15 nm^{-3}), and late stage (<0.15 nm^{-3}) of dealumination. For early stage dealuminated crystals (n = 4), acid site densities at the center of the crystal are 0.78–1.15 nm^{-3} and there is a zone with an acid site density of 0.15–0.17 nm^{-3}underlying the crystal facet where the main channels are surfacing (**Figure 2.3B**). For the intermediate stage dealuminated crystals (n = 5), the behavior is similar; however, the absolute densities in the center (0.25–0.99

nm^{-3}) and at the edge (0.10–0.15 nm^{-3}) are generally lower (**Figure 2.3C**). Crystals at the late dealumination stage (n = 4) in this sample show homogeneous distributions with densities of 0.08–0.11 nm^{-3} (**Figure 2.3D**). Further dealumination also results in homogeneous distribution of the acid site with lower density (0.07–0.1 nm^{-3}) in SD-MOR (n = 3, **Figure 2.2E**). Most crystals (n = 47), however, did not show a measurable SRS signal while the detection limit of our current setup was determined to be 0.07 molecules nm^{-3} with a SNR larger than 3. Whereas the Si/Al ratio from bulk elemental analysis shows a 10-fold decreased total aluminum content compared to SP-MOR, the acid site density measured by SRS reduces over 20-fold, implying that a considerable amount of the aluminum does not contribute to the measured acidity, for example, pentahedral and octahedral aluminum species.[40]

The SRS spectra of CD_3CN in MD-MOR shows various shifts in the C≡N stretch region not only between different crystals but also within one single crystal (**Figure 2.5A,B**), depending on the extent of dealumination. In the center of a crystal, which is the least dealuminated region as shown in **Figure 2.3B**, CD_3CN chemisorbed in the main channel (I_{cc}^{SRS}) shows a shift of 10 cm^{-1} (**Figure 2.5A**), whereas the shift decreases to 2 cm^{-1} for CD_3CN in the side pocket ($I_{bb}^{SRS} - I_{cc}^{SRS}$). In the highly dealuminated regions of the crystal near the edge, the C≡N stretch of CD_3CN in the main channel decreases from 2275 to 2271 cm^{-1} (**Figure 2.5B**). Note that the relative amount of CD_3CN located in the side pockets increases in the dealuminated region (**Figure 2.5B**), implying that the acid sites in the main channel are removed preferentially (Supporting Information).

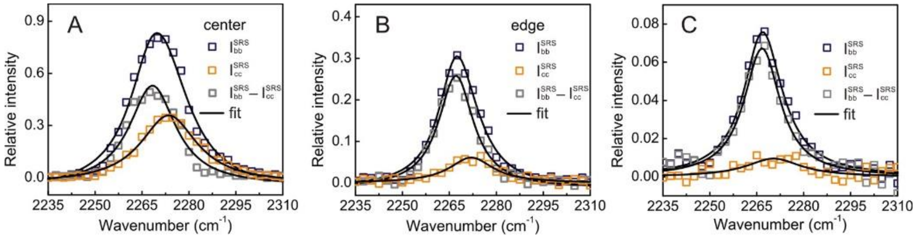

Figure 2.5. SRS microspectroscopy of CD_3CN adsorbed in MD-MOR and SD-MOR. SRS spectra of CD_3CN adsorbed in the (A) center and (B) edge of an early dealuminated MD-MOR crystal and (C) in the SD-MOR recorded with lasers polarized in crystallographic b- (I_{bb}^{SRS}) and c-axes (I_{cc}^{SRS}).

The SRS spectra in the C≡N stretch region, averaged over a whole SD-MOR crystal, are shown in **Figure 2.4C**. Smaller shifts in C≡N vibration, 2 and 6 cm^{-1}, were observed for CD_3CN in the side pocket (2267 cm^{-1}, $I_{bb}^{SRS} - I_{cc}^{SRS}$) and the main channel (2271 cm^{-1}, I_{cc}^{SRS}), respectively. Despite the low intensity of the SRS signal, we estimate an approximately 5-fold increase in the relative amount of available acid sites in the side pockets versus main channels from the polarized SRS intensities of the measurable SD-MORs. It is known that hydrothermal dealumination produces extra-framework aluminum (EFAl) species, which stay in close proximity to remaining framework aluminum located mainly in the side pocket.[40,41] This change in environment (e.g., in confinement effect as well as in acid site strength) can lead to the rather small peak shift observed for this situation (2 cm^{-1} with respect to liquid CD_3CN, **Figure 2.5B**); even for nitriles in bulk infrared spectroscopy, both factors have been linked to observed variations in C≡N vibration frequency.[36,42] These spatially resolved acidity maps provide a unique insight into the dealumination process. Whereas kinetic studies of zeolite dealumination are sparse, aluminum removal is generally described to proceed via the reaction with an apparent first-order kinetics with respect to the total framework aluminum content;[43] this model, however, not only assumes a step-by-step aluminum removal process, which is generally accepted from bulk NMR data,[44] but also assumes homogeneous process conditions for all crystals and within every crystal's volume, such as temperature, framework composition, and the absence of chemical gradients (e.g., water, dealumination agents, etc.).

The intercrystal heterogeneity in MD-MOR and the peculiar acid site distribution showing two distinct areas with different densities separated by a steep transition zone within individual crystals, observed for early and intermediate stage dealuminated crystals (**Figure 2.6**), cannot be explained by this hypothesis. Clearly, the extent of dealumination in the zones underneath the crystal surface where the main channels are surfacing is higher than in the middle of the crystal, suggestive of the presence of a diffusion-limited process step. Likely, a moving front, induced by hindered mass transport, is at the origin of the observed heterogeneity; the length scales over which the observed variations occur rule out temperature effects. Compositional variations are also very unlikely because of the homogeneous aluminum distribution in the starting material SP-MOR. Possibly, the EFAl species in the main channels of the mordenite strongly hinder mass transport, and the removal of these barriers and associated pore opening during acid leaching can be considered slow because of single-file diffusion. It is only upon more extensive acid leaching that fast mass transport throughout an increasingly broader outer crystal is restored.

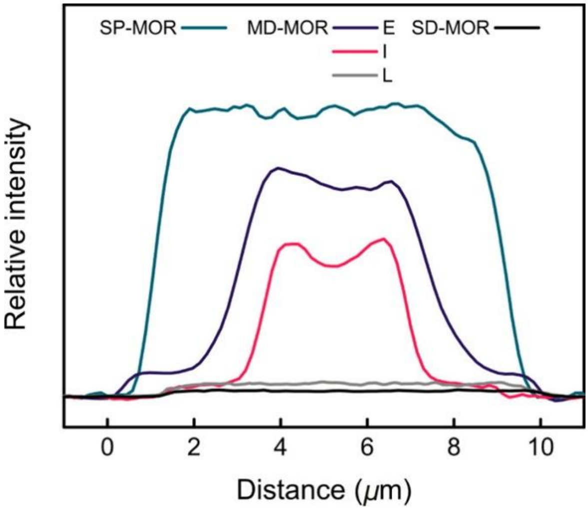

Figure 2.6. Horizontal line profiles of SRS signal from CD_3CN adsorbed in H-MORs. Profiles are plotted for the crystals shown in **Figure 2.3**; E, I, and L denote MD-MOR crystals at early, intermediate, and late stages of dealumination; curves are centered for better comparison.

Indirect support for this hypothesis can be found in a report by Moreno and Poncelet, where the authors show a strongly reduced dealumination by acid leaching in small-port versus large-port mordenites, whereas variations in hydrothermal dealumination are only minimal.[30] However, it should be emphasized that mordenite dealumination is a complex process that depends on many parameters and consists of several consecutive process steps.

To further support this model, PhCN was used to probe the acid site accessibility. For PhCN, an opposite trend compared to CD_3CN was found (**Figure 2.7**). SP-MOR crystals show no sign of PhCN uptake inside the crystals due to the small-port behavior. In MD-MOR samples, again three types of crystals are found. In early dealuminated crystal PhCN, probes only access the rim of the crystal just below the pore entrances, that is, the dealuminated region (**Figure 2.7A**). As the extent of dealumination increases, PhCN gradually reaches the center of the crystal, following the direction of main channels (**Figure 2.7B**). Extensive self-healing and mesopore creation in late stage dealuminated MD-MOR crystals and SD-MOR result in homogeneous PhCN distributions (**Figure 2.7C,D**), that is, full availability of acid sites. Two C≡N stretching frequencies, 2237 and 2249 cm^{-1}, are observed in both MD-MOR and SD-MOR with, respectively, 4 and 16 cm^{-1} shifts compared to liquid PhCN (**Figure 2.7E**).

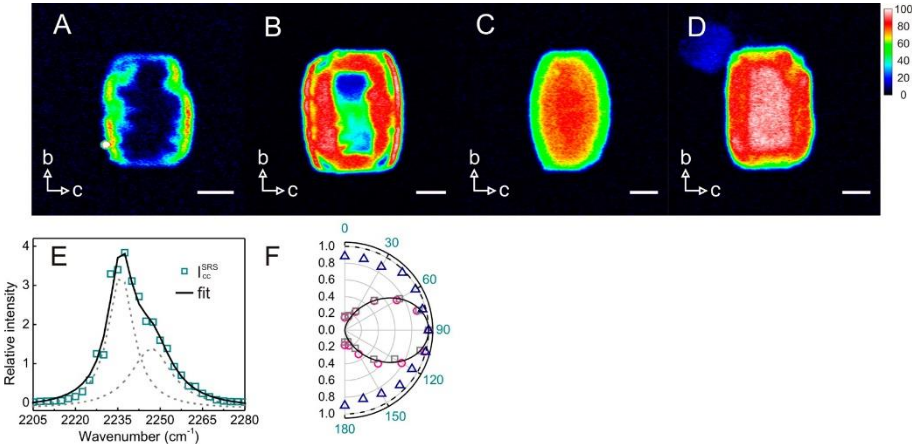

Figure 2.7. SRS microspectroscopy and polarization dependence of PhCN adsorbed in H-MORs. (A–D) Chemical mapping (2249 cm^{-1}) of PhCN adsorbed in H-MORs revealing the accessibility of acid sites; gradual enhancement of acid site availability in MD-MOR from early (A), intermediate (B), and to late stages (C) of dealumination as well as SD-MOR (D). Images were recorded with lasers polarized along the crystallographic c-axis. False color scale indicates relative abundance of PhCN (from 0 to 100 au). Crystal axes are indicated by arrows. Scale bar: 3 μm. (E) SRS response in the C≡N stretch region for PhCN adsorbed in SD-MOR averaged over a single crystal; spectrum is fitted by a sum (solid line) of two Lorentzian curves (dashed lines). (F) Polar plots of 2237.5 (circles) and 2249 cm^{-1} (squares) vibrations with respect to crystallographic b-axis recorded in the *bc* plane of the crystal; a $\sin^2\theta$ function (solid line) is shown for comparison. Polar plot of 2237.5 cm^{-1} with respect to crystallographic *b*-axis recorded in the *ab* plane of the crystal (triangles); a circle with a radius of 1 (solid line) is shown for comparison.

The spectral profile is similar for different samples; only the relative intensity of the 2249 cm^{-1} peak slightly decreases from 44% in MD-MOR to 37% in SD-MOR. The polar plots of both the vibrations at 2237 and 2249 cm^{-1} show that the C≡N bond is parallel to the crystallographic *c*-axis (**Figure 2.7F**); this is also evident from the very small polarization dependence of the SRS response when looking along the crystallographic *c*-axis (**Figure 2.7F**), indicating that PhCN molecules are inside the micropores with the C≡N bond aligned parallel to the main channel. Since PhCN is a stronger base than CD_3CN, the C≡N stretches of 2249 and 2237 cm^{-1} are assigned to the PhCN interacting with Brønsted acid framework groups and weaker EFAl species, respectively.[45]

2.2.3 Dealumination at the Single-crystal Level

The catalytic reactivity, associated with the Brønsted acid hydroxyls as observed by NASCA microscopy, is dictated by the convolved effects of the active site distribution and the accessibility inside the catalyst porous network. In depth insight has now been generated by SRS microscopy using a suitable probe molecule that provides a detailed picture of the site distribution and accessibility of H-MOR crystals at different stages of the dealumination process.

Initially, before dealumination, the acid sites are homogeneously distributed throughout the microporous network of the SP crystals. These sites are, however, inaccessible to larger, aromatic molecules, limiting the oligomerization of furfuryl alcohol to the crystals’ surface. At early stages of dealumination, only the outer regions of the crystal near the outer surface become partially accessible for aromatics due to the transition from small-port to large-port behavior while the core remains inaccessible to PhCN; this is reflected in the catalytic performance. At the intermediate stage of dealumination, the central part of the crystals also becomes partially available for PhCN, whereas the edges of the crystals are fully accessible; as a result, the local catalytic performance becomes largely determined by the local acid site density, which is higher in the center of the crystal. Finally, after extensive dealumination (i.e., for the late stage dealuminated MD-MOR and SD-MOR), the crystals are fully available but have a strongly reduced acid site density, explaining the homogeneous reactivity map with a relatively lower turnover rate.

2.2.4 Mesoporosity and Catalytic Performance

Mesopore creation in zeolites is often beneficial because of the enhanced mass transport; it can, however, also deteriorate the shape selectivity. Polarized light excitation in NASCA microscopy allows determining the orientation of the formed catalytic reaction products (**Figure 2.8**). Such measurements show that over 90% of the fluorescent reaction products are aligned along the main channels for all the dealuminated mordenite samples regardless of the degree of dealumination, indicating that the acid-catalyzed furfuryl alcohol oligomerization preferentially takes place inside the original microporous structure of the mordenite crystals.

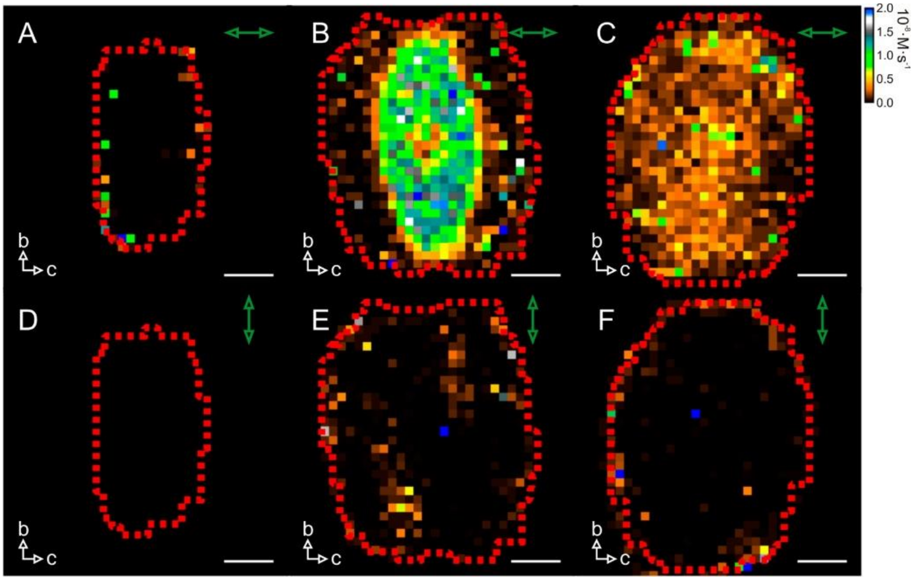

Figure 2.8. Polarization-resolved NASCA reactivity maps of furfuryl alcohol conversion onto H-MORs obtained for 500 × 500 × 800 nm^3 (XYZ) voxels. (A,D) SP-MOR crystal; (B,E) MD-MOR crystal; (C,F) SD-MOR crystal. Green arrow indicates orientation of polarization of excitation light; false color scale indicates observed reaction rate (from 0 to 2×10^{-8} $M{\cdot}s^{-1}$); crystal axes are indicated by white arrows.

2.3 CONCLUSIONS

It has been demonstrated with NASCA microscopy that the catalytic performance of dealuminated acid mordenites shows a remarkable heterogeneity at the intercrystal and subcrystal level. Rationalization of this observation is possible by studying the acid site distribution and accessibility at the same length scales using stimulated Raman microscopy with nitrile probe molecules. Uniquely, this approach allows one to spatially resolve the acid site distribution, directly relevant to the catalytic performance rather than aluminum content, as in the case of other techniques. Importantly, the parent mordenite does not show any gradient in acid site density, and therefore, all heterogeneities observed in dealuminated samples are the result of the postsynthetic treatment. Besides stimulated Raman microspectroscopy and polarization-dependent signal intensity, the use of different nitrile probes made it possible for the first time to directly generate insights into the removal of aluminum from different framework positions as well as to unravel the complex interplay between framework aluminum removal and the small-port to large-port mordenite transition by steaming and acid leaching. Similar questions are highly relevant not only to H-MOR and the effect of dealumination but also to zeolite research in general. This novel approach can be applied to study the physicochemical properties of heterogeneous catalysts in general by adapting well-developed strategies in infrared spectroscopy.

2.4 EXPERIMENTAL SECTION

2.4.1 **NASCA Microscopy[13]**

Synthetic mordenites SP-MOR (ZM-101, NH_4 form, Si/Al ratio 6.2), MD-MOR (ZM-510, H form, Si/Al ratio 11), and SD-MOR (ZM-980, H form, Si/Al ratio 65) were obtained from Zéocat (Montoir de Bretagne, France). For the microscopy experiments, the crystals were deposited on a #1 cover glass via spin-coating from an aqueous suspension. Calcination on the cover glass in an ashing furnace (Nabertherm LVT 3/11) was done according to the following three-step procedure. First, the samples were heated to 80°C (1°C/min) and kept at this temperature for 1 h to remove easily desorbing molecules. Next, they were heated to 120°C (1°C/min) and kept at this temperature for 1 h to remove physisorbed water and minimize undesirable hydrothermal dealumination. Further, the samples were heated to 450°C (1°C/min) at which temperature the samples were kept for 50 h to remove contaminants and convert SP-MOR into the acidic H form. After this heat treatment, samples were cooled and used for microscopy experiments within several hours after cooling. Liquid-phase experiments on an inverted epifluorescence microscope were performed using a Teflon container sealed to the glass coverslip via a silicone rubber gasket.

Furfuryl alcohol oligomerization (water–furfuryl alcohol mixture 0.7% wt) was used as a fluorogenic reaction for the NASCA experiments. Furfuryl alcohol (Sigma-Aldrich, 98%) was additionally purified by vacuum distillation prior to the measurements. Milli-Q water was obtained from the water purification system Synergy UV (Merck Millipore).

The NASCA investigation was performed on the WFM setup based on an inverted microscope IX71 platform (Olympus, Japan) equipped with an oil immersion objective lens (Olympus, 100×, 1.4 NA) and a diode-pumped solid-state Excelsior laser (Spectra-Physics, USA). The latter provided a laser excitation with λ_{exc} = 532 nm (Spectra-Physics Excelsior) of 100 W/cm^2 power on the sample. Fluorescence imaging (545 nm long-pass filter) was performed with an EM-CCD camera ImagEM Enhanced C9100-13 (Hamamatsu, Japan). Further single-molecule identification, localization, and generation of the NASCA images were performed with dedicated routines (http://sushi.chem.kuleuven.be/svn/Localizer/) for IgorPro v.6.34A software

(Wavemetrics, USA). The presented images were obtained by the accumulation of localized fluorescent emitters which appeared during reaction in the focal plane in the middle of the crystals for a recording duration of 90 s.

2.4.2 SRS Microscopy[25]

The mordenites were deposited on a clean cover glass #1 via spin-coating from an aqueous suspension. These mordenite-loaded cover glasses were heated to 450°C with a temperature ramp of 1°C/min under air. After 10 h at 450°C, these samples were quickly transferred, while hot, into a cleaned desiccator under nitrogen atmosphere. After being cooled to room temperature the desiccator was opened briefly to add a few drops of liquid CD_3CN (100% with 99.96% D atom, Sigma-Aldrich) or PhCN (99%, Sigma-Aldrich) to the samples. After 10 h and prior to measurements, the excess nitrile was removed by purging with argon. The SRS imaging was performed on an upright microscope (BX61WI/FV1000, Olympus) with 25×, 1.05 NA water immersion objective (XLPLAN, Olympus). An optical parametric oscillator (OPO) (Levante Emerald, APE-Berlin) was synchronously pumped by the second harmonic of a Nd:YVO4 laser (picoTRAIN, High-Q) operating at a fundamental wavelength of 1064 nm with a repetition of 80 MHz. The OPO employs a temperature-tuned non-critically phase-matched LBO crystal and an intracavity Lyot filter to allow continuous tuning of the OPO output. The signal beam (700–980 nm) from the OPO and the fundamental 1064 nm beam were used as the pump and Stokes beam, respectively. The Stokes beam was amplitude-modulated at 9.7 MHz with a Pockel Cell (model 360-80, ConOptics) triggered by a function generator (model 29, Waveteck). The power of each beam at focus was 15–20 mW. The transmitted beams were collected with an oil immersion condenser (U-UCD8, Olympus) and were then reflected off the microscope with a dichroic mirror (FF750, Semrock). A band-pass filter (Chroma Technology, CARS 890/220 m) was used to block the Stokes beam, and the stimulated Raman loss (SRL) of the pump beam was detected by a large-area silicon PIN photodiode (S8650, Hamamatsu) with reversed bias of 60 V. The output photocurrent is low-pass-filtered (Mini-Circuits, BLP-1.9+) and demodulated by a lock-in amplifier (HF2LI, Zurich Instrument). The output of the lock-in amplifier is fed into the analog-to-digital converter (FV-10-ANALOG, Olympus) synchronized with the scanning unit. Optical transmission images were recorded with a digital camera (XC50, Olympus).

For the SRL spectra acquisition, OPO is sequentially tuned with home-built LabVIEW software. An SRL image was recorded within a fixed field of view at each OPO wavelength, that is, hyperspectral imaging, which allowed us to analyze the SRL spectra in any specific region of interest. The intensity variations of the OPO beam were recorded simultaneously by reflecting 10% of the OPO beam to a power meter with a broad-band beam splitter (FS01, Semrock) and were used to correct the SRL signal. The polarization dependence of the SRL signal was measured by simultaneously controlling the polarization of the pump and Stokes beams with two zero-order half-wave plates (WPH05M, Thorlabs). Before recording SRL image or spectra, an analyzer was used to ensure that the polarizations of the two beams are parallel in either vertical or horizontal plane.

2.5 REFERENCES

[1] N. Mizuno, M. Misono, *Chem. Rev.* **1998**, *98*, 199–218.

[2] K. Tanabe, *Appl. Catal. A Gen.* **1999**, *181*, 399–434.

[3] G. Busca, *Chem. Rev.* **2007**, *107*, 5366–5410.

[4] J. Čejka, G. Centi, J. Perez-Pariente, W. J. Roth, *Catal. Today* **2012**, *179*, 2–15.

[5] W. M. Meier, *Zeitschrift für Krist.* **1961**, *115*, 439–450.

[6] P. Magnoux, P. Cartraud, S. Mignard, M. Guisnet, *J. Catal.* **1987**, *106*, 242–250.

[7] M. J. Remy, M. J. Genet, P. P. Notté, P. F. Lardinois, G. Poncelet, *Microporous Mater.* **1993**, *2*, 7–15.

[8] N. S. Nesterenko, F. Thibault-Starzyk, V. Montouillout, V. V. Yuschenko, C. Fernandez, J.-P. Gilson, F. Fajula, I. I. Ivanova, *Microporous Mesoporous Mater.* **2004**, *71*, 157–166.

[9] M. B. J. Roeffaers, G. De Cremer, H. Uji-i, B. Muls, B. F. Sels, P. A. Jacobs, F. C. De Schryver, D. E. De Vos, J. Hofkens, *Proc. Natl. Acad. Sci. U.S.A.* **2007**, *104*, 12603–12609.

[10] T. Cordes, S. A. Blum, *Nat. Chem.* **2013**, *5*, 993–999.

[11] I. L. C. Buurmans, B. M. Weckhuysen, *Nat. Chem.* **2012**, *4*, 873–886.

[12] M. B. J. Roeffaers, B. F. Sels, H. Uji-I, F. C. De Schryver, P. A. Jacobs, D. E. De Vos, J. Hofkens, *Nature* **2006**, *439*, 572–575.

[13] M. B. J. Roeffaers, G. De Cremer, J. Libeert, R. Ameloot, P. Dedecker, A. J. Bons, M. Bückins, J. A. Martens, B. F. Sels, D. E. De Vos, et al., *Angew. Chem. Int. Ed.* **2009**, *48*, 9285–9289..

[14] W. Xu, J. S. Kong, Y.-T. E. Yeh, P. Chen, *Nat. Mater.* **2008**, *7*, 992–996.

[15] E. de Smit, I. Swart, J. F. Creemer, G. Hoveling, M. Gilles, T. Tyliszczak, P. Kooyman, H. Zandbergen, C. Morin, B. Weckhuysen, et al., *Nature* **2008**, *456*, 222–225.

[16] L. R. Aramburo, E. De Smit, B. Arstad, M. M. Van Schooneveld, L. Sommer, A. Juhin, T. Yokosawa, H. W. Zandbergen, U. Olsbye, F. M. F. De Groot, et al., *Angew. Chem. Int. Ed.* **2012**, *51*, 3616–3619.

[17] L. R. Aramburo, Y. Liu, T. Tyliszczak, F. M. F. De Groot, J. C. Andrews, B. M. Weckhuysen, *ChemPhysChem* **2013**, *14*, 496–499.

[18] L. R. Aramburo, S. Teketel, S. Svelle, S. R. Bare, B. Arstad, H. W. Zandbergen, U. Olsbye, F. M. F. de Groot, B. M. Weckhuysen, *J. Catal.* **2013**, *307*, 185–193.

[19] E. Stavitski, B. M. Weckhuysen, *Chem. Soc. Rev.* **2010**, *39*, 4615–4625.

[20] M. A. Bañares, G. Mestl, in *Adv. Catal.*, Elsevier Inc., **2009**, 43–128.

[21] P.-P. Knops-Gerrits, D. E. De Vos, E. J. P. Feijen, P. A. Jacobs, *Microporous Mater.* **1997**, *8*, 3–17.

[22] M. H. F. Kox, K. F. Domke, J. P. R. Day, G. Rago, E. Stavitski, M. Bonn, B. M. Weckhuysen, *Angew. Chem. Int. Ed.* **2009**, *48*, 8990–8994.

[23] K. F. Domke, T. A. Riemer, G. Rago, A. N. Parvulescu, P. C. A. Bruijnincx, A. Enejder, B. M. Weckhuysen, M. Bonn, *J. Am. Chem. Soc.* **2012**, *134*, 1124–1129.

[24] J. P. R. Day, K. F. Domke, G. Rago, H. Kano, H. Hamaguchi, E. M. Vartiainen, M. Bonn, *J. Phys. Chem. B* **2011**, *115*, 7713–7725.

[25] C. W. Freudiger, W. Min, B. G. Saar, S. Lu, G. R. Holtom, C. He, J. C. Tsai, J. X. Kang, X. S. Xie, *Science* **2008**, *322*, 1857–1861.

[26] X. Zhang, M. B. J. Roeffaers, S. Basu, J. R. Daniele, D. Fu, C. W. Freudiger, G. R. Holtom, X. S. Xie, *ChemPhysChem* **2012**, *13*, 1054–1059.

[27] E. Freund, C. Marcilly, F. Raatz, *J. Chem. Soc. Chem. Commun.* **1982**, *5*, 309–310.

[28] F. Raatz, C. Marcilly, E. Freund, *Zeolites* **1985**, *5*, 329–333.

[29] P. C. Van Geem, K. F. M. G. J. Scholle, G. P. M. Van der Velden, W. S. Veeman, *J. Phys. Chem.* **1988**, *92*, 1585–1589.

[30] S. Moreno, G. Poncelet, *Microporous Mater.* **1997**, *12*, 197–222.

[31] C. Hamon, J. Bandiera, M. Senes, *US Patent 4447669*, **1984**.

[32] M. B. J. Roeffaers, J. Hofkens, G. De Cremer, F. C. De Schryver, P. A. Jacobs, D. E. De Vos, B. F. Sels, *Catal. Today* **2007**, *126*, 44–53.

[33] M. B. J. Roeffaers, R. Ameloot, M. Baruah, H. Uji-i, M. Bulut, G. De Cremer, U. Müller, P. A. Jacobs, J. Hofkens, B. F. Sels, et al., *J. Am. Chem. Soc.* **2008**, *130*, 5763–5772.

[34] R. Ameloot, F. Vermoortele, J. Hofkens, F. C. De Schryver, D. E. De Vos, M. B. J. Roeffaers, *Angew. Chem. Int. Ed.* **2013**, *52*, 401–405.

[35] M. Bevilacqua, A. G. Alejandre, C. Resini, M. Casagrande, J. Ramirez, G. Busca, *Phys. Chem. Chem. Phys.* **2002**, *4*, 4575–4583.

[36] O. Marie, F. Thibault-Starzyk, J.-C. Lavalley, *Phys. Chem. Chem. Phys.* **2000**, *2*, 5341–5349.

[37] T. Montanari, M. Bevilacqua, G. Busca, *Appl. Catal. A Gen.* **2006**, *307*, 21–29.

[38] V. D. Dominguez-Soria, P. Calaminici, A. Goursot, *J. Phys. Chem. C* **2011**, *115*, 6508–6512.

[39] H. Huo, L. Peng, Z. Gan, C. P. Grey, *J. Am. Chem. Soc.* **2012**, *134*, 9708–9720.

[40] T. H. Chen, K. Houthoofd, P. J. Grobet, *Microporous Mesoporous Mater.* **2005**, *86*, 31–37.

[41] Z. Yu, S. Li, Q. Wang, A. Zheng, X. Jun, L. Chen, F. Deng, *J. Phys. Chem. C* **2011**, *115*, 22320–22327.

[42] K. S. Smirnov, F. Thibault-Starzyk, *J. Phys. Chem. B* **1999**, *103*, 8595–8601.

[43] Q. L. Wang, G. Giannetto, M. Torrealba, G. Perot, C. Kappenstein, M. Guisnet, *J. Catal* **1991**, *130*, 459–470.

[44] G. Engelhardt, U. Lohse, V. Patzelová, M. Mägi, E. Lippmaa, *Zeolites* **1983**, *3*, 233–238.

[45] T. Montanari, M. Bevilacqua, C. Resini, G. Busca, *J. Phys. Chem. B* **2004**, *108*, 2120–2127.

2.6 SUPPORTING INFORMATION

2.6.1 Quantification of Intracrystal Reactivity Distribution from NASCA Experiments

In order to quantify the inter- and intracrystal heterogeneity reactivity maps containing the localized reaction events for 500 x 500 x 800 nm^3 voxels were reconstructed; the effective thickness of the observed layer is assumed to be 800 nm. The histogram, showing the reactivity distribution, was fitted with Lorentzian curves which give an indication of the number of zones within the crystals which show a distinct catalytic activity. The peak location corresponds to the most often observed reaction rate in the region, whereas FWHM of the peak reports on the degree of heterogeneity in that region. Binned NASCA images, histograms and results of fitting are presented in the **Figure 2.2**. The used fitting parameters are summarized in **Table 2.S1**.

The resolution of NASCA microscopy that can be obtained with current experimental conditions is typically around 20 nm. However, for a detailed statistical analysis large amount of turnovers per voxel is required to clearly deconvolute individual activity peaks in the histogram. Therefore, we decided to use a larger voxel size than the minimal one allowed by the precision of NASCA microscopy.

Table 2.S1. Obtained peak parameters for fitting the histograms in **Figure 2.2 A-E** and displayed in **Figure 2.2 F-J**.

Sample (histogram)	Peak number	Location, (M·s^{-1} × 10^{-10})	Relative Area	FWHM, (M·s^{-1} × 10^{-10})
SP-MOR (2F)	0	0	0.83±0.01	0.65±0.01
	1	2.6±0.1	0.17±0.02	2.5±0.3
SD-MOR (2G)	0	16.6±0.4	1.00	13±1
MD-MOR (2H)	0	0	0.71±0.02	1.24±0.02
	1	2.6±0.6	0.29±0.04	8.3±0.9
MD-MOR (2I)	0	4.3±0.1	0.61±0.02	9.1±0.4
	1	95±3	0.39±0.04	51±8
MD-MOR (2J)	0	2.3±0.2	0.09±0.02	2.3±0.9
	1	24±1	0.91±0.08	29±3

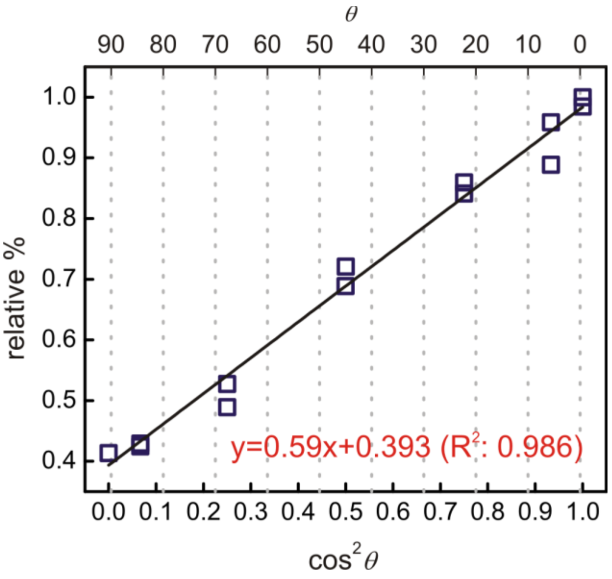

Figure 2.S1. Linear relationship between cos^{2}θ and relative SRS response of C≡N stretch; θ is the angle between laser polarization and crystallographic *b*-axis; the slope and intercept indicate the contributions from anisotropic and isotropic terms, respectively.

2.6.2 Quantification of Adsorbed CD_3CN Density

For spontaneous Raman measurement, the procedures of calculating orientation independent spectrum for a system of uniaxial symmetry have been established. Using the coordinate system given in **Figure 2.S2** the orientation independent spectrum can be obtained from a linear combination of four polarized Raman measurements [1,2]

$$I^{iso}(3+6R) = I_{bb} + 2I_{cc} + 2I_{ca} + 4I_{bc} \qquad (\mathbf{2.S1})$$

where I_{ij} indicates the Raman intensity ($I_{ij} = I_{ji}$) measured with incident and scattered photons polarized parallel to the *i* and *j*-directions, respectively; *R* is the Raman depolarization ratio evaluated from an isotropic sample; in this case liquid CD_3CN.[2] Because we are only interested in the C≡N vibration, the depolarization ratio of I_{bb} (R_1) and I_{cc} terms (R_2) can be introduced into equation (**2.S1**).

$$R_1 = \frac{I_{bc}}{I_{bb}}, \qquad (\mathbf{2.S2})$$

$$R_2 = \frac{I_{ca}}{I_{cc}}, \qquad (\mathbf{2.S3})$$

and thus

$$I^{iso}(3+6R) = I_{bb}(1+4R_1) + 2I_{cc}(1+R_2). \qquad (\mathbf{2.S4})$$

When performing measurement on a microscope, however, the number of scattering intensities, I_{ij}^{μ} (*μ* denotes the Raman signal measured using an optical microscope), that can be measured is limited; the four Raman intensities I_{bb}, I_{cc}, I_{ca}, and I_{cb}, can be evaluated by:[3,4]

$$I_{bb} = \frac{1}{AC_0}\left(I_{bb}^{\mu} - \frac{B}{A+B} I_{bc}^{\mu}\right), \qquad (\mathbf{2.S5})$$

$$I_{cc} = \frac{1}{AC_0}\left(I_{cc}^{\mu} - I_{cb}^{\mu} + \frac{A}{A+B} I_{bc}^{\mu}\right), \qquad (\mathbf{2.S6})$$

$$I_{cb} = \frac{I_{bc}^{\mu}}{C_0(A+B)}, \qquad (\mathbf{2.S7})$$

$$I_{ca} = \frac{1}{BC_0}(I^{\mu}_{cb} - \frac{A}{A+B} I^{\mu}_{bc}), \qquad (\mathbf{2.S8})$$

with

$$A = \pi^2(\frac{4}{3} - \cos\theta_m - \frac{1}{3}\cos^3\theta_m), \qquad (\mathbf{2.S9})$$

and

$$B = 2\pi^2(\frac{2}{3} - \cos\theta_m + \frac{1}{3}\cos^3\theta_m). \qquad (\mathbf{2.S10})$$

where A and B account for the collection of the Raman scattering with an objective of given numerical aperture (NA); C_0 is related to the energy distribution of incident electric field at the focal plane; θ_m is the half angle of NA. The depolarization ratio *R* can be evaluated from the experimental depolarization ratio obtained by microscopy R^{μ}:

$$R^{\mu} = \frac{(A+B)R}{A+BR}. \qquad (\mathbf{2.S11})$$

The relationship between normal Raman intensity and SRS response is given by:[5]

$$I^{\mu}_{ij} = \kappa I^{SRS}_{kl}. \qquad (\mathbf{2.S12})$$

where κ is the proportionality coefficient, and a constant κ value is assumed for different configurations of laser polarization. The depolarization ratio (R^{μ}) of the C≡N stretch for liquid CD_3CN is determined with the SRS setup by using parallel and perpendicular polarizations between pump and Stokes beams (**Figure 2.S3A**).[6] The obtained depolarization ratio R is 0.04 with a NA=1.05 objective; a low value typical for A1 mode vibrations. I^{SRS}_{bb}, I^{SRS}_{cc}, I^{SRS}_{bc}, and I^{SRS}_{cb} are measured for CD_3CN adsorbed in SP-MOR crystals (**Figure 2.S3B**). R_1 and R_2 are 0.06 and 0.04, respectively, evaluated by equations (**2.S2**), (**2.S3**), and (**2.S5**)–(**2.S8**). By rearranging (**2.S5**)–(**2.S8**), I_{bb} and I_{cc} can be obtained by

$$I_{bb} = \frac{I^{\mu}_{bb}}{C_0(A+BR_1)} = \frac{\kappa I^{SRS}_{bb}}{C_0(A+BR_1)}, \qquad (\mathbf{2.S13})$$

$$I_{cc} = \frac{I^{\mu}_{cc}}{C_0(A+BR_2)} = \frac{\kappa I^{SRS}_{cc}}{C_0(A+BR_2)}. \qquad (\mathbf{2.S14})$$

By substitution of (**2.S13**) and (**2.S14**) and of numerical values of A, B, R, R_1, and R_2 into equation (**2.S4**), the orientation independent spectrum for adsorbed CD_3CN (I^{iso}_{ad,CD_3CN}) can be calculated by

$$I^{iso}_{ad,CD_3CN} = \frac{\kappa}{\pi^2 C_0}\left(0.58 I^{SRS}_{bb} + 0.98 I^{SRS}_{cc}\right). \qquad (\mathbf{2.S15})$$

On the other hand, for liquid CD_3CN, $I^{iso}_{CD_3CN} = I_{zz}$, and thus

$$I^{iso}_{CD_3CN} = \frac{I^{\mu}_{zz}}{C_0(A+BR)} = \frac{\kappa I^{SRS}_{zz}}{C_0(A+BR)} = \frac{\kappa}{\pi^2 C_0} 1.54 I^{SRS}_{zz}. \qquad (\mathbf{2.S16})$$

where I^{SRS}_{zz} represents the SRS response recorded with pump and Stokes beams polarized along the laboratory *z*-axis. Assuming a similar Raman scattering cross-section, the density of adsorbed CD_3CN can be evaluated by comparing its integrated C≡N peak intensity (**2.S15**) to that of liquid CD_3CN (**2.S16**) with known density (10.8 nm^{-3}). Note that the uniaxial symmetry is maintained after dealumination (**Figure 2.4**), equation (**2.S15**) and (**2.S16**) are still valid for the quantification of site density. Similarly, the density map can be reconstructed using (**2.S15**) via a linear combination of two chemical mappings, at the peak of the C≡N stretch, along crystallographic *b*- and *c*-axes, respectively. The resulting intensity map is orientation independent, assuming constant bandwidth, and after laser power normalization the scale is calibrated with that of liquid CD_3CN (**2.S16**).

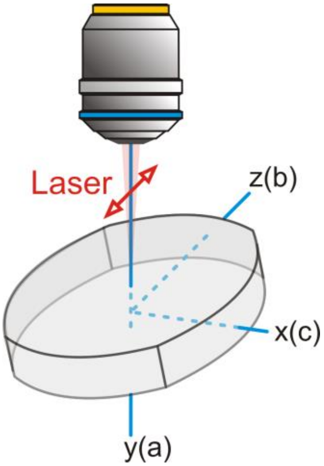

Figure 2.S2. Schematic drawing of laboratory and crystallographic axes (latter shown between brackets); laboratory *z* and *x*-axes are aligned to crystallographic *b* and *c* (or *a*) axes by rotating the crystals before the measurement.

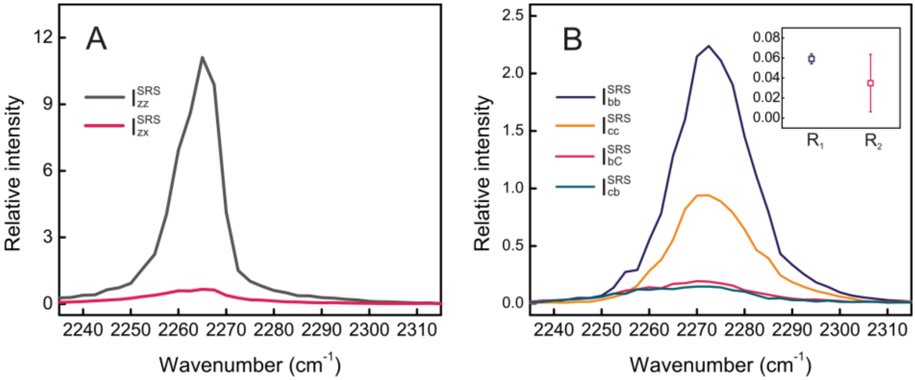

Figure 2.S3. SRS response in the C≡N stretch region of liquid CD_3CN (A) and CD_3CN adsorbed in SP-MOR (B), averaged within the whole crystal, measured with different configurations of laser polarization; inset shows the depolarization ratios R_1 and R_2.

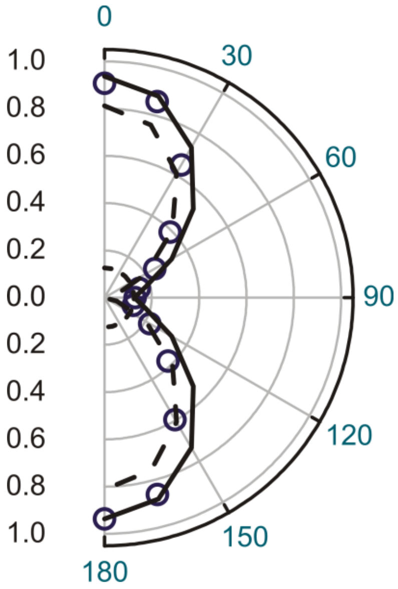

Figure 2.S4. Polar plot of C≡N stretch (2267 cm^{-1}) recorded at the edge of an early dealuminated MD-MOR crystal, where the acid sites in main channels have been preferentially removed.

2.6.3 Quantification of Acid Site Density in Main Channel and Side Pocket

Since the SRS response of C≡N vibration for CD_3CN adsorbed side pockets ($I_{bb}^{SRS}-I_{cc}^{SRS}$) and main channels ($I_{cc}^{SRS}$) possess a uniaxial (a $\cos^2\theta$ function, θ is the angle between laser polarization and crystallographic *b*-axis) and isotropic symmetry, respectively, their orientation independent spectra can be calculated by substituting individual SRS signal into (**2.S15**) and (**2.S16**). Noted the $I_{bb}^{SRS}-I_{cc}^{SRS}$ spectrum approaches maximum and zero with lasers polarized in crystallographic *b*- and *c*-axes, respectively. We thus obtain

$$I_{\text{side pocket}}^{\text{iso}}=\frac{\kappa}{\pi^2 C_0}\left[0.58(I_{bb}^{SRS}-I_{cc}^{SRS})\right], \quad (\textbf{2.S17})$$

$$I_{\text{main channel}}^{\text{iso}}=\frac{\kappa}{\pi^2 C_0}1.54 I_{cc}^{SRS}. \quad (\textbf{2.S18})$$

The ratio of acid site in side pocket to main channel can be obtained by comparing the integrated intensity of (**2.S17**) to that of (**2.S18**).

Among SP-MOR crystals the ratio is 0.37±0.05, and is almost a constant within single crystal. However, for MD-MOR samples at early and intermediate stage of dealumination the ratio increases to 0.4–0.5 and 0.7–1.3 at the center and edge of the crystal, respectively, showing the acid sites in the main channel are removed preferentially. For MD-MOR at a late stage of dealumination and for SD-MOR the ratio is 1.3–1.8; this is independent of the position inside a single crystal. Note that CD_3CN adsorbed in the side pocket might possess some orientational freedom resulting in a slight misalignment between the crystallographic *b*-axis and laboratory *z*-axis, which both could result in a slight underestimation of the acid site density in the side pocket; e.g. for a C≡N bond oriented at an average angle of 10° with respect to crystallographic *b*-axis the ratio of acid site in side pocket vs. main channel would only increase from 0.37 to 0.40 i.e. about 8% difference.

2.6.4 Spontaneous Raman Measurements

Spontaneous Raman measurements on some H-MOR were performed to validate the SRS spectra. CD_3CN/SP-MOR, PhCN/MD-MOR, and PhCN/SD-MOR samples are selected because of their favorable spontaneous Raman signal. Spontaneous Raman spectra were recorded with an inverted confocal Raman microscope (Ti-U, Nikon). The 632.8 nm line from a He–Ne laser (Research Electro-Optics) was used as the excitation source. Excitation polarization was converted to circular by a quarter-wave plate. The laser beam was guided through a dichroic mirror (Chroma Technology, z633rdc) to the objective and focused onto the center of each crystal with a 60× 0.95 NA air objective (Nikon). The backward Raman scattering was collected by the same objective and passed through a 100-μm confocal pinhole, filtered by a long-pass filter (Chroma Technology, HQ645LP), and directed into a monochromator (HORIBA, iHR320). The signal was dispersed with a 600 grooves/mm grating (Andor Technology) and detected by a CCD camera (Newton, Andor Technology). Typical integration time for each crystal was 5 minutes.

Figure 2.S5A presents spontaneous Raman spectra of CD_3CN adsorbed in SP-MOR; the C≡N stretch shifts to 2274.6±0.7 cm^{-1} which resembles the wavenumbers obtained with SRS microscopy. **Figures 2.S5B,C** show the spontaneous Raman spectra of PhCN adsorbed in MD- and SD-MOR, respectively. Similar spectral profiles with two C≡N vibrational frequencies are observed for PhCN, which are 2238.1±0.7 and 2247.8±1.6 cm^{-1}, respectively. The spontaneous Raman measurements validate the approach, SRS microscopy in combination with nitrile probe, employed in this study.

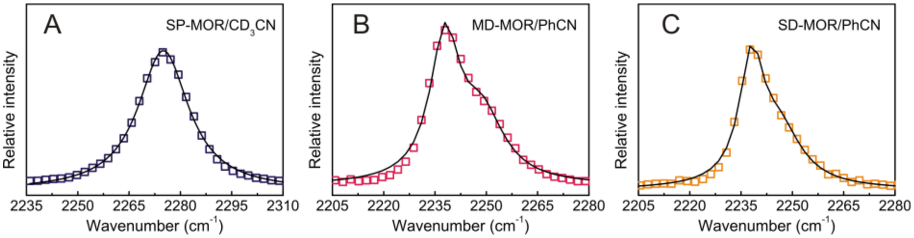

Figure 2.S5. (A–C) Spontaneous Raman measurement of SP-MOR/CD_3CN (A), MD-MOR/PhCN (B), and SD-MOR/PhCN (C); experimental data of SP-MOR and MD-, SD-MOR are fitted by a single Lorentzian curves and a sum of two Lorentzian curves (solid line), respectively.

2.6.5 References

[1] M. Tanaka, R. J. Young, *J. Mater. Sci.* **2006**, *41*, 963–991.

[2] S. Frisk, R. M. Ikeda, D. B. Chase, J. F. Rabolt, *Appl. Spectrosc.* **2003**, *57*, 1053–1057.

[3] T. Lefèvre, M. E. Rousseau, M. Pézolet, *Appl. Spectrosc.* **2006**, *60*, 841–846.

[4] C. Sourisseau, *Chem. Rev.* **2004**, *104*, 3851–3891.

[5] M. D. Levenson, S. S. Kano, *Introduction to Nonlinear Laser Spectroscopy*, Academic Press INC., London, UK, **1988**.

[6] F. Munhoz, S. Brustlein, R. Hostein, P. Berto, S. Brasselet, H. J. Rigneault, *Raman. Spectrosc.* **2012**, *43*, 419–424.

CHAPTER 3

Noninvasive nanoscopy uncovers the impact of the hierarchical porous structure on the catalytic activity of single dealuminated mordenite crystals

Alexey V. Kubarev, Kris P. F. Janssen, Maarten B. J. Roeffaers

Adapted with permission from: *ChemCatChem* **2015**, *7*, 3646–3650

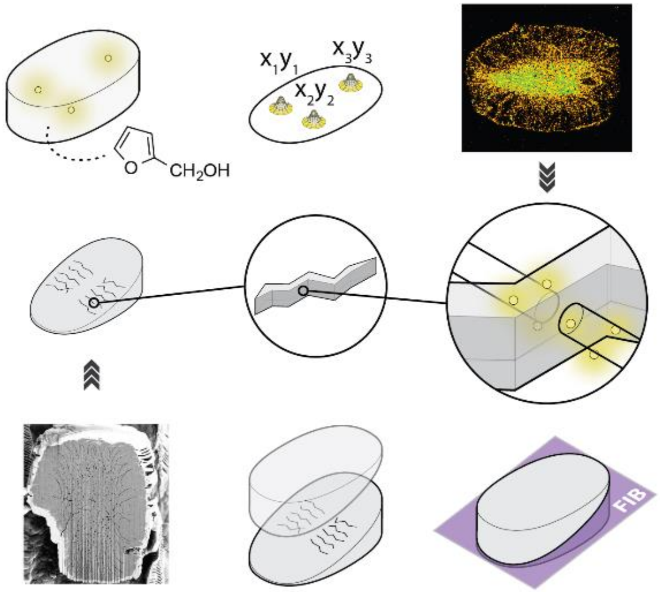

Abstract

Spatial restrictions around catalytic sites, provided by molecular-sized micropores, are beneficial to reaction selectivity but also inherently limit diffusion. The molecular transport can be enhanced by introducing meso- and macropores. However, the impact of this extra-framework porosity on the local nanoscale reactivity is relatively unexplored. Herein we show that the area of enhanced reactivity in hierarchical zeolite, examined with super-resolution fluorescence microscopy, is spatially restricted to narrow zones around meso- and macropores, as observed with focused ion-beam-assisted SEM. This comparison indicates that reagent molecules efficiently reach catalytic active sites only in the micropores surrounding extra-framework porosity and that extensive macroporosity does not warrant optimal reactivity distribution throughout a hierarchical porous zeolite.

Contributions

The main part of the experimental work and article writing was performed by Alexey Kubarev. Maarten Roeffaers and Alexey Kubarev conceived the project. All authors were involved in data interpretation and article writing.

CHAPTER 3 – NONINVASIVE NANOSCOPY UNCOVERS THE IMPACT OF THE HIERARCHICAL POROUS STRUCTURE ON THE CATALYTIC ACTIVITY OF SINGLE DEALUMINATED MORDENITE CRYSTALS

3.1 INTRODUCTION

Nanoporosity ensures an optimal interaction between a heterogeneous solid catalyst and a reaction mixture.[1]* The resulting large specific surface area, in combination with a high density of active sites, enables the effective use of the entire catalyst particle volume. Depending on their diameter, pores can play several important roles in the heterogeneous catalytic process. Molecular-sized micropores provide spatial restrictions for reagent and/or product molecules around the catalytic active site, and this gives rise to the unique ability to control the reaction outcome on the basis of molecular dimensions. Ideally, these pores are an inherent feature of the crystalline framework ordering, as this would lead to reproducible and uniform pore dimensions, as in the case of zeolites. Such shape-selective zeolite catalysts are widely employed in numerous industrial processes.[3,4]

However, an inherent drawback of these molecular sieve catalysts is restricted diffusion, which often leads to suboptimal crystal volume utilization and accelerates catalyst aging.[5] These intracrystalline diffusion limitations can be overcome through the introduction of larger extra-framework meso- and macroporosity into the solid catalyst, which enhances the effectiveness.[6] Perturbation of the periodic crystal structure during creation of a hierarchical porous catalyst can, however, also cause undesired changes in the catalyst's properties or affect the catalytic reaction conditions. For example, at the level

---

*Porosity-describing terms are used according to IUPAC recommended classification: “micropores” for pore sizes up to 2 nm, “mesopores” for sizes of 2–50 nm, and “macropores” for pores larger than 50 nm.[2] “Nanopores” is used as an overarching term for all pores with a size in the nanometer range (up to 100 nm). Extra-framework porosity refers to meso- and macropores that are not part of the zeolite's crystal structure and that, in this case, are introduced by postsynthetic zeolite modification.

of the catalyst's properties, decreased structure density and modifications of the chemical composition can lead to a decrease in the density of active sites. At the reaction level, there is a possibility of side reactions occurring on active sites in the larger extra-framework pores, which leads to partial loss of micropore-induced shape selectivity. Whereas the overall effect of meso- and macropore introduction on catalytic performance has thoroughly been investigated at the ensemble-averaged scale level,[6] the direct impact of extra-framework porosity on the local, nanoscale reactivity remains relatively unexplored.[7] Nonetheless, small-scale, microscopy-based investigations seem especially essential in view of several recent studies, which revealed the major impact of structural and compositional heterogeneities on the catalytic performance within and between individual catalyst particles.[7-15]

Dealuminated mordenite zeolites are well-known and widely used hierarchical porous catalysts.[16,17] In addition to the intrinsic unidimensional framework microporosity of the mordenite zeolite structure,[18,19] postsynthetic dealumination can further introduce extra-framework meso- and macroporosity.[20,21] It is commonly assumed that such extra-framework porosity provides more efficient access to the inner micropore volume. However, single-crystal studies of these materials are few, and none have made the direct link between extra-framework pore structure and local catalytic activity.[22-25] For these reasons, dealuminated mordenite can be considered an ideal model system for the nanoscale study of hierarchical porous systems. To reveal the effect of the extra-framework porosity on the local catalytic activity, we opted to apply two complementary microscopy techniques. Direct extra-framework porosity visualization inside a zeolite crystal was performed by SEM assisted by focused ion-beam (FIB) milling; this approach is particularly suited for detailed structural characterization of catalyst particles not transparent to the electron beam.[7,26,27] Next, the local catalytic activity was imaged by confocal and super-resolution fluorescence microscopy at the single crystal and single catalytic turnover levels.

3.2 RESULTS AND DISCUSSION

For this study, we employed an industrially produced dealuminated synthetic acid mordenite sample. High-resolution SEM is in its nature a surface characterization technique that does not allow the direct exploration of the dealumination-induced extra-framework porosity inside a zeolite crystal. For this reason, we resorted to focused ion-beam milling to slice the zeolite crystal in a very precise way, thus exposing the interior of the material for SEM observation (**Figure 3.1**).

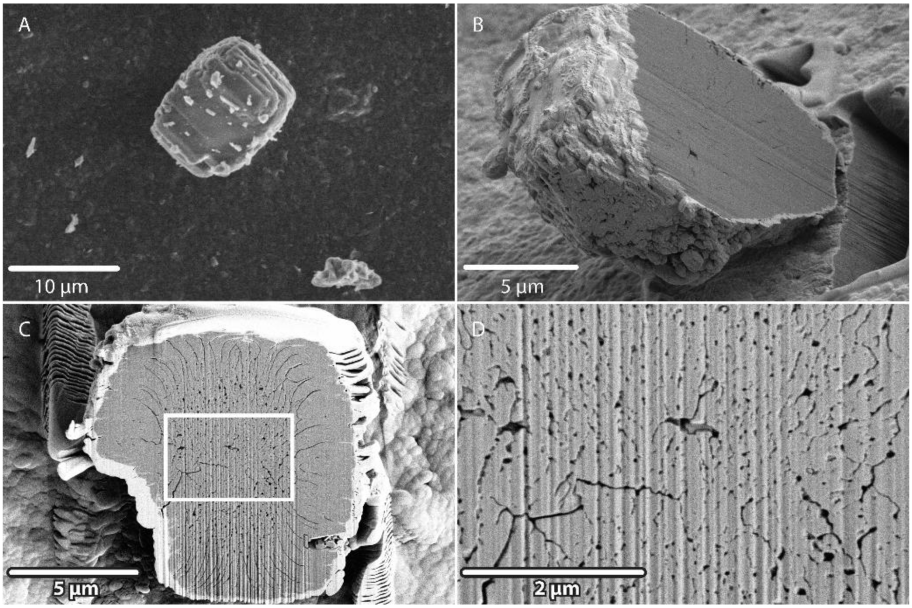

Figure 3.1. SEM images of A) the intact dealuminated mordenite crystal and B) the side view, C) the front view (white rectangle indicates area of panel D), and D) a highly magnified front view of the FIB-cut dealuminated mordenite crystal. Note that some curtaining effect of the FIB sectioning is visible as straight lines running from the top to the bottom of the crystal section.

A diagonal section of the crystal was made with a beam of Ga^+ ions (**Figure 3.1 B**). Magnification of the freshly uncovered crystal interior reveals an extensive system of macropores running throughout the crystal (**Figure 3.1 C, D**).

In contrast to multiple earlier single-crystal studies, for which a random and irregular orientation of meso- or macropores in hierarchical zeolites was seen,[22-25,28-30] in this crystal the similarly highly and randomly porous core is complemented by distinct radial pores extending from the center of the crystal to its edges. Next, 10 consecutive images were acquired by shaving approximately 3 nm per slice of the exposed zeolite surface by using the FIB, which allowed evolution of the local 3D extra-framework porosity to be traced and represented (**Figure 3.S1**). The observed bimodal pore-size distribution is likely a result of uneven dealumination conditions for different parts of the crystal.

One could expect extended extra-framework macroporosity to result in an improved catalytic performance of the zeolite crystals' interior as a result of strongly enhanced molecular transport. However, depletion of framework aluminum might offset this beneficial effect, as a loss in the associated acid sites could result in a reduction in catalytic performance. Moreover, the observed bimodal pore distribution might give rise to a more complicated situation, such as limited accessibility of the potentially active core by diffusion of the reagent through radial pores.

To investigate the effects of dealumination and the resulting extra-framework porosity on catalytic performance at a scale compatible with the previous SEM nanoscopy, we relied on super-resolution fluorescence microscopy. The local activity inside catalyst particles can be resolved by monitoring the fluorescence signal originating from the conversion of fluorogenic reactants into fluorescent reaction products.[8,14,31-40] Furfuryl alcohol was used as reactant because it fits inside the mordenite framework micropores and because acid-catalyzed oligomerization leads to the formation of fluorescent oligomers (**Figure 8.1**).[32,41] We focused on the initial reactivity, as we were interested in the impact of the enhanced molecular transport in the extra-framework porosity on the catalytic performance; all fluorescent microscopy observations were performed within the first 20 min after reagent addition. Further, this minimized the effect of pore blocking by formed reaction products. CLSM allows the fluorescence intensity in a 1 μm thick layer of a crystal to be measured and, hence, allows the local catalytic performance to be evaluated (**Figure 3.2**).

The measured activity profile closely matches the porosity pattern observed with FIB-SEM. Stepwise shifting of the focal plane allows the intracrystal activity distribution throughout the whole crystal volume to be observed. The uncovered 3D reactivity profile also shows similar activity patterns throughout the entire crystal (**Figure 3.2 A**). According to previous research, we know that acid site distribution in such crystals does not follow the observed fan-shaped linear pattern.[10] Therefore, these results clearly show that the entire crystal volume is not available for reactant molecules despite the extensive extra-framework porosity. Although the observed elongated zones of catalytic activity follow the same pattern as the extra-framework pores, the resolution of the CLSM is diffraction-limited and prohibits accurate zone size estimation. Furthermore, the registered fluorescent intensity is not linearly dependent on the chemical reaction rate owing to uneven accumulation of fluorescent product and variance in the number of emitted photons per molecule.

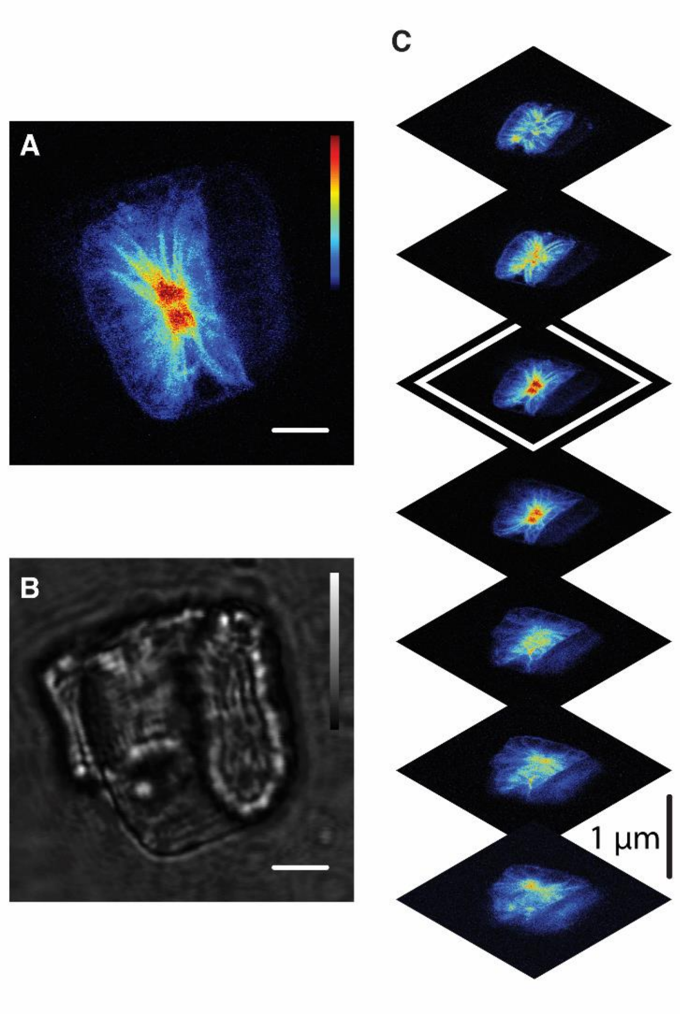

Figure 3.2. CLSM microphotograph of furfuryl alcohol oligomers obtained and accumulated within the mordenite crystal. A) Fluorescence image slice (middle of the crystal, depth of field is approximately 800 nm). B) Transmission image. C) Optical sectioning of the crystal. Z-scan was performed with a step size of 1 µm in the axial direction. The white border outlines the slice presented in large in panel B. False color scale shows the observed fluorescence intensity, scale bar: 3 µm.

To address these issues, we applied NASCA microscopy, which is super-resolution fluorescence microscopy that enables direct reactivity quantification. NASCA microscopy relies on the mathematical localization of single fluorescent reaction products to circumvent the diffraction-limited resolution of typical far-field fluorescence microscopy.[41-43]

This localization enables accurate pinpointing of the reaction product molecule down to a precision of 10 nm. By registering the exact locations of successive, individual reaction events, it becomes possible to distinguish between active and inactive zones at the nanoscale on the basis of differences in their observed catalytic activity.

The reactivity map, obtained from this NASCA approach, is presented in **Figure 3.3 A** for a representative crystal sample, along with the bright-light transmission image of the same crystal in **Figure 3.3 C**. These reactivity maps are 2 D histograms of the distributions of the localized emitters, reconstructed in 50 × 50 nm^2 bins. Additional examples can be found in **Figure 3.S2**. Similar to the CLSM measurements, the spatial reactivity pattern matches the extra-framework porosity pattern observed by FIB-SEM. Precise analysis of the scatter plot of localized catalytic turnovers inside the zeolite crystal reveals that these highly active zones have a characteristic width of (110±40) nm (**Figure 3.3 B**).

This size is larger than the localization precision, which ranges from 10 to 50 nm, and this indicates that active zones might correspond to either the macropores or to the microporous zones of the crystal that border the mesopores. Therefore, the question as to where the reaction happens—in the extra-framework macropores or in the original micropores of the mordenite structure—remains unanswered.

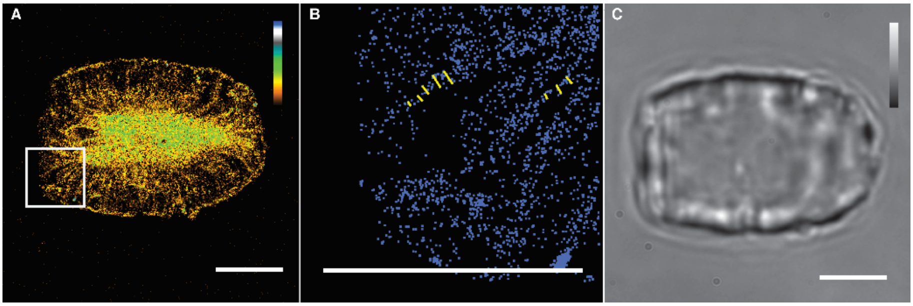

Figure 3.3. Optical microscopy investigation of furfuryl alcohol conversion inside a mordenite crystal. Scale bars: 3 μm. A) NASCA reactivity map obtained for 50 × 50 × 800 nm^3 voxels (*xyz*) for the duration of 500 s; false color scale shows the observed relative reaction rate; white rectangle indicates area enlarged in panel B. B) Magnification showing the scatter plot with locations of individual reaction events; yellow lines indicate distances taken for region width estimation. C) Corresponding bright-field optical transmission image.

In an effort to distinguish between both possibilities, we used polarization-resolved fluorescence microscopy measurements, which yield direct insight into the spatial orientation of the product molecules with respect to the underlying pore system. To this end, we used linear polarized excitation light instead of typical circular polarization (**Figure 3.4**).

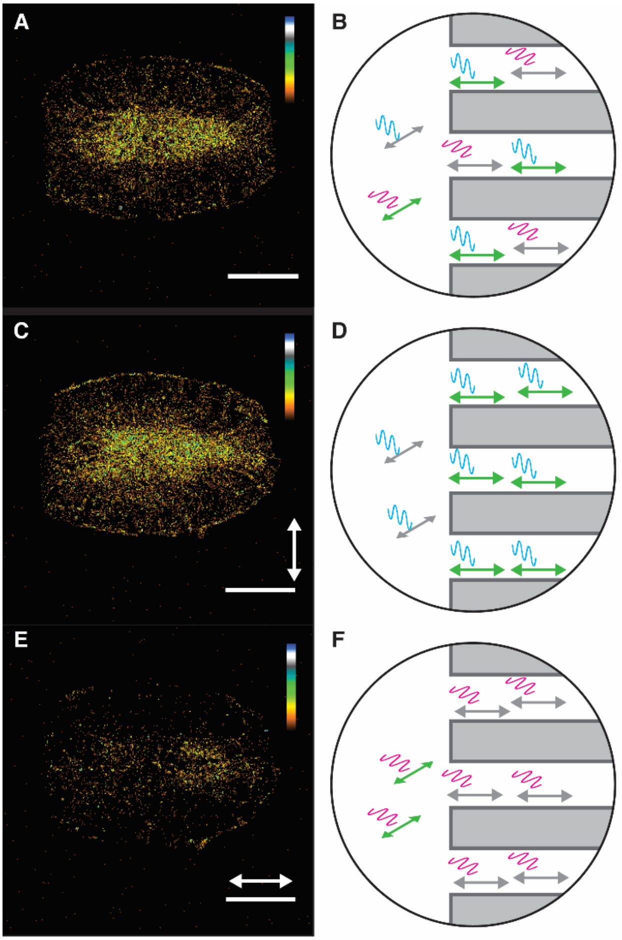

Figure 3.4. Excitation polarization resolved WFM investigation of furfuryl alcohol conversion inside a mordenite crystal. Scale bars: 3 µm. NASCA reactivity maps obtained for 50 × 50 × 800 nm^3 voxels (*xyz*) for the duration of 150 s; false color scale indicates observed relative reaction rate. A) NASCA reactivity map obtained with circular polarization of excitation light. C, E) NASCA reactivity maps obtained with linear polarization of excitation light; white arrows indicate the light polarization. B, D, F) Schematic representation of light-fluorophore interaction in the experiments presented in A, C, and E, respectively. Cyan and magenta waves indicate photons with different orientation of polarization plane, green/gray arrows stand for excited/not excited fluorophore molecules.

Compared to the situation for which the excitation light polarization was perpendicular to the micropores direction (**Figure 3.4 E, F**), linearly polarized light parallel to the crystal's micropores could excite 4.1 times more molecules (**Figure 3.4 C, D**). Thus, most of the fluorescent reaction product molecules are observed in the micropores, in which they are highly aligned. In contrast, reactivity inside the extra-framework pores, in which molecular orientation is more randomized, is limited (**Figure 3.4 B, D, F**).

This observation agrees well with the previously reported results of polarization-resolved fluorescence microscopy investigation of other dealuminated mordenite crystals.[10] However, it was never shown that the observed activity takes place along the micropores directly outlining the distinct extra-framework pores. Additionally, it can be seen that circularly polarized light of the same intensity excites molecules less efficiently than linearly polarized light parallel to the micropores because of the reduced probability of absorption (**Figure 3.4 A, B**).

3.3 CONCLUSIONS

Our results show that in dealuminated mordenites the reagent molecules can only reach catalytic active sites in close vicinity of the extra-framework porosity. The results prove that the common belief that the existence of macropores will invariably result in full accessibility to the inner microporous structure is not always correct. Possibly due to small-port behavior of mordenite, even a hierarchical porous structure with seemingly extensive macroporosity can lead to suboptimal reactivity distribution throughout a crystal. This degree of insight into the catalytic activity can only be obtained by correlating detailed structural information, for example, from electron microscopy, with high-resolution molecular insight generated by super-resolution fluorescence microscopy. Such single-crystal-level studies provide a solid basis for the rational design of catalysts.

3.4 EXPERIMENTAL SECTION

3.4.1 Materials

Dealuminated synthetic mordenite MD-MOR (ZM-510, H-form, Si/Al ratio = 11) was obtained from Zéocat (France). 98% pure furfuryl alcohol (Sigma-Aldrich, USA) was additionally purified by vacuum distillation prior to experiments. MilliQ water was obtained from water purification system Synergy UV (Merck Millipore, USA).

3.4.2 FIB-SEM

The SEM imaging and cross-section FIB slicing and milling were performed using an Scios Dual Beam system (FEI, The Netherlands). Before FIB cutting, a 2 μm protective layer applied to the crystal surface through ion-beam-assisted deposition (30 kV, 1 nA) to minimize the curtaining effect. Ga^+ ion beams of 30 kV/15 nA and 1 nA were used for trench milling and sample slicing respectively; slice thickness was 3 nm. Conventional SEM (1 kV, 13 pA, WD = 6.9-7.1 mm, spotsize 5 nm) was used to observe crystal morphology after FIB milling and slicing. Image acquisition was performed using the lower (T1) in-lens BSE detector and using NG Microscope User Interface software (FEI); further image analysis and processing were performed with AutoSlice And View software (FEI).

3.4.3 Fluorescence Microscopy - Sample Preparation

For the microscopy experiments, crystals were deposited on a #1 cover glass through spincoating from an aqueous suspension. Calcination on the cover glass in an ashing furnace LVT 3/11 (Nabertherm, Germany) was conducted in three stages. First the samples were heated to 80°C (1°C/min) and kept at this temperature for 1 h in order to remove easily desorbing molecules. Next, they were heated to 120°C (1°C/min) and kept at this temperature for 1 h to remove physisorbed water, minimizing undesirable hydrothermal dealumination. Finally, the samples were heated to 450°C (1°C/min) and subsequently kept at this temperature for 50 h to remove fluorescent contaminants. After allowing samples to cool, they were immediately used in microscopy experiments to prevent re-adsorption of fluorescent contaminants from the environment. Liquid phase experiments on an inverted epi-fluorescence microscope were performed using a polytetrafluoroethylene container sealed to the glass cover slip via a silicone rubber gasket. All fluorescent microscopy observation were carried out within first 20 minutes after reagent addition.

3.4.4 Fluorescence Microscopy - CLSM

Furfuryl alcohol oligomerization (water-furfuryl alcohol mixture 9.3% wt) was used as a fluorogenic reaction. CLSM images were acquired using a FluoView FV1000 (Olympus, Japan) with an oil immersion objective lens (100×, 1.4 NA, Olympus) and λ_{exc} = 532 nm, λ_{em} = 545-645 nm. Further image analysis and processing was performed with ImageJ v.1.49i software (NIH, USA).

3.4.5 Fluorescence Microscopy - NASCA Microscopy

Furfuryl alcohol oligomerization (water-furfuryl alcohol mixture 6.7% wt) was used as a fluorogenic reaction. The NASCA investigation was conducted on a WFM setup based on an inverted microscope IX71 (Olympus) platform equipped with an oil immersion objective lens (100×, 1.4 NA, Olympus) and a Diode-Pumped Solid State Excelsior laser (Spectra-Physics, USA). The latter provided a laser excitation with $\lambda = 532$ nm of 100 W/cm^2 power on the sample. Fluorescence imaging (545 nm long pass filter) was performed using an ImagEM Enhanced C9100-23B EM-CCD camera (Hamamatsu, Japan). Further single molecule identification, localization and generation of NASCA images were performed using an in-house developed set of open-source plugin routines (https://bitbucket.org/pdedecker/localizer)[43] for IgorPro v.6.34A software (Wavemetrics, USA). The presented NASCA images were obtained by the accumulation of localized fluorescent emitters which appeared during reaction in the focal plane in the middle of the crystals for a recording duration indicated in the figure caption.

3.5 REFERENCES

[1] M. E. Davis, *Nature* **2002**, *417*, 813–821.

[2] D. H. Everett, *Pure Appl. Chem.* **1972**, *31,* 577–638.

[3] N. Mizuno, M. Misono, *Chem. Rev.* **1998**, *98*, 199–218.

[4] J. Čejka, G. Centi, J. Perez-Pariente, W. J. Roth, *Catal. Today* **2012**, *179*, 2–15.

[5] P. Magnoux, P. Cartraud, S. Mignard, M. Guisnet, *J. Catal.* **1987**, *106*, 242–250.

[6] J. Pérez-Ramírez, C. H. Christensen, K. Egeblad, C. H. Christensen, J. C. Groen, *Chem. Soc. Rev.* **2008**, *37*, 2530–2542.

[7] L. R. Aramburo, L. Karwacki, P. Cubillas, S. Asahina, D. A. M. De Winter, M. R. Drury, I. L. C. Buurmans, E. Stavitski, D. Mores, M. Daturi, et al., *Chem. - A Eur. J.* **2011**, *17*, 13773–13781.

[8] M. H. F. Kox, E. Stavitski, J. C. Groen, J. Pérez-Ramírez, F. Kapteijn, B. M. Weckhuysen, *Chem. - A Eur. J.* **2008**, *14*, 1718–1725.

[9] R. Ameloot, F. Vermoortele, J. Hofkens, F. C. De Schryver, D. E. De Vos, M. B. J. Roeffaers, *Angew. Chem. Int. Ed.* **2013**, *52*, 401–405.

[10] K.-L. Liu, A. V. Kubarev, J. Van Loon, H. Uji-i, D. E. De Vos, J. Hofkens, M. B. J. Roeffaers, *ACS Nano* **2014**, *8*, 12650–12659.

[11] L. R. Aramburo, S. Teketel, S. Svelle, S. R. Bare, B. Arstad, H. W. Zandbergen, U. Olsbye, F. M. F. de Groot, B. M. Weckhuysen, *J. Catal.* **2013**, *307*, 185–193.

[12] L. Sommer, S. Svelle, K. P. Lillerud, M. Stöcker, B. M. Weckhuysen, U. Olsbye, *Langmuir* **2010**, *26*, 16510–16516.

[13] I. L. C. Buurmans, B. M. Weckhuysen, *Nat. Chem.* **2012**, *4*, 873–886.

[14] M. B. J. Roeffaers, R. Ameloot, A.-J. Bons, W. Mortier, G. De Cremer, R. de Kloe, J. Hofkens, D. E. De Vos, B. F. Sels, *J. Am. Chem. Soc.* **2008**, *130*, 13516–13517.

[15] K. P. F. Janssen, G. De Cremer, R. K. Neely, A. V. Kubarev, J. Van Loon, J. A. Martens, D. E. De Vos, M. B. J. Roeffaers, J. Hofkens, *Chem. Soc. Rev.* **2014**, *43*, 990–1006.

[16] X. Tu, M. Matsumoto, T. Matsuzaki, T. Hanaoka, Y. Kubota, J.-H. Kim, Y. Sugi, *Catal. Letters* **1993**, *21*, 71–75.

[17] J. Lecomte, A. Finiels, P. Geneste, C. Moreau, *J. Mol. Catal. A Chem.* **1998**, *133*, 283–288.

[18] W. M. Meier, *Zeitschrift für Krist.* **1961**, *115*, 439–450.

[19] P. Simoncic, T. Armbruster, *Am. Mineral.* **2004**, *89*, 421–431.

[20] N. S. Nesterenko, F. Thibault-Starzyk, V. Montouillout, V. V. Yuschenko, C. Fernandez, J.-P. Gilson, F. Fajula, I. I. Ivanova, *Microporous Mesoporous Mater.* **2004**, *71*, 157–166.

[21] K.-H. Lee, B.-H. Ha, *Microporous Mesoporous Mater.* **1998**, *23*, 211–219.

[22] H. Ajot, J. F. Joly, J. Lynch, F. Raatz, P. Caullet, in *Stud. Surf. Sci. Catal.*, **1991**, 583–590.

[23] A. J. Koster, U. Ziese, A. J. Verkleij, A. H. Janssen, K. P. De Jong, *J. Phys. Chem. B* **2000**, *104*, 9368–9370.

[24] J. C. Groen, T. Sano, J. A. Moulijn, J. Pérez-Ramírez, *J. Catal.* **2007**, *251*, 21–27.

[25] Y. Jin, Y. Li, S. Zhao, Z. Lv, Q. Wang, X. Liu, L. Wang, *Microporous Mesoporous Mater.* **2012**, *147*, 259–266.

[26] L. Karwacki, D. A. M. De Winter, L. R. Aramburo, M. N. Lebbink, J. A. Post, M. R. Drury, B. M. Weckhuysen, *Angew. Chem. Int. Ed.* **2011**, *50*, 1294–1298.

[27] S. Mitchell, N.-L. Michels, K. Kunze, J. Pérez-Ramírez, *Nat. Chem.* **2012**, *4*, 825–831.

[28] A. H. Janssen, A. J. Koster, K. P. De Jong, *J. Phys. Chem. B* **2002**, *106*, 11905–11909.

[29] J. Lynch, F. Raatz, P. Dufresne, *Zeolites* **1987**, *7*, 333–340.

[30] C. Choi-Feng, J. B. Hall, B. J. Huggins, R. A. Beyerlein, *J. Catal.* **1993**, *140*, 395–405.

[31] G. De Cremer, B. F. Sels, D. E. De Vos, J. Hofkens, M. B. J. Roeffaers, *Chem. Soc. Rev.* **2010**, *39*, 4703–4717.

[32] M. B. J. Roeffaers, B. F. Sels, H. Uji-i, B. Blanpain, P. L'hoëst, P. A. Jacobs, F. C. De Schryver, J. Hofkens, D. E. De Vos, *Angew. Chem. Int. Ed.* **2007**, *46*, 1706–1709.

[33] M. R. Decan, S. Impellizzeri, M. L. Marin, J. C. Scaiano, *Nat Commun* **2014**, *5*, 4612.

[34] T. Cordes, S. A. Blum, *Nat. Chem.* **2013**, *5*, 993–999.

[35] E. M. Hensle, S. A. Blum, *J. Am. Chem. Soc.* **2013**, *135*, 12324–12328.

[36] W. Xu, J. S. Kong, Y.-T. E. Yeh, P. Chen, *Nat. Mater.* **2008**, *7*, 992–996.

[37] N. M. Andoy, X. Zhou, E. Choudhary, H. Shen, G. Liu, P. Chen, *J. Am. Chem. Soc.* **2013**, *135*, 1845–1852.

[38] N. M. Esfandiari, Y. Wang, J. Y. Bass, T. P. Cornell, D. A. L. Otte, M. H. Cheng, J. C. Hemminger, T. M. McIntire, V. A. Mandelshtam, S. A. Blum, *J. Am. Chem. Soc.* **2010**, *132*, 15167–15169.

[39] N. M. Esfandiari, S. A. Blum, *J. Am. Chem. Soc.* **2011**, *133*, 18145–18147.

[40] P. Chen, X. Zhou, N. M. Andoy, K.-S. Han, E. Choudhary, N. Zou, G. Chen, H. Shen, *Chem. Soc. Rev.* **2014**, *43*, 1107–1117.

[41] M. B. J. Roeffaers, G. De Cremer, J. Libeert, R. Ameloot, P. Dedecker, A. J. Bons, M. Bückins, J. A. Martens, B. F. Sels, D. E. De Vos, et al., *Angew. Chem. Int. Ed.* **2009**, *48*, 9285–9289.

[42] M. B. J. Roeffaers, B. F. Sels, H. Uji-I, F. C. De Schryver, P. A. Jacobs, D. E. De Vos, J. Hofkens, *Nature* **2006**, *439*, 572–575.

[43] P. Dedecker, S. Duwé, R. K. Neely, J. Zhang, *J. Biomed. Opt.* **2012**, *17*, 126008.

SUPPORTING INFORMATION TO CHAPTER 3

3.6 SUPPORTING INFORMATION

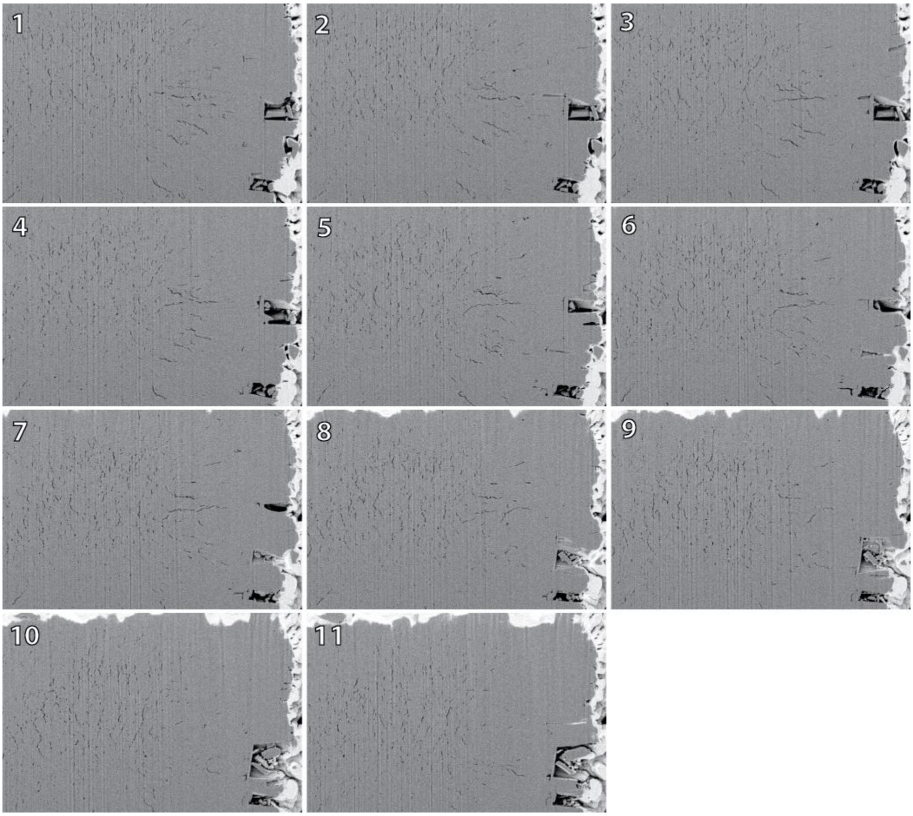

Figure 3.S1. SEM images of a gradually FIB-sliced dealuminated mordenite crystal. Step size of slicing is 3 nm.

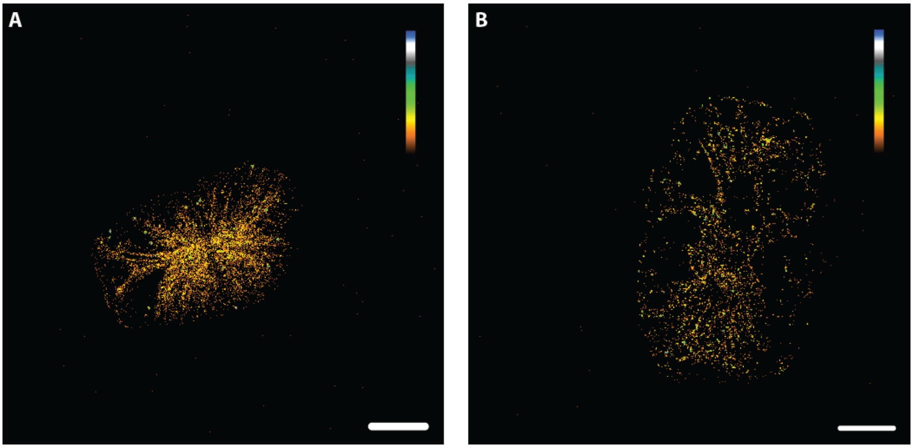

Figure 3.S2. WFM investigation of furfuryl alcohol conversion inside several mordenite crystals. NASCA reactivity maps were obtained for 50 × 50 × 800 nm^3 voxels (XYZ). False color scale shows the observed relative reaction rate; scale bars: 3 μm.

CHAPTER 4

Solvent polarity-induced pore selectivity in H-ZSM-5 catalysis

Alexey V. Kubarev, Eric Breynaert, Jordi Van Loon, Arunasish Layek, Guillaume Fleury, Sambhu Radhakrishnan, Johan A. Martens, Maarten B. J. Roeffaers

Adapted with permission from *ACS Catalysis*, **2017**, *7,* 4248–4252

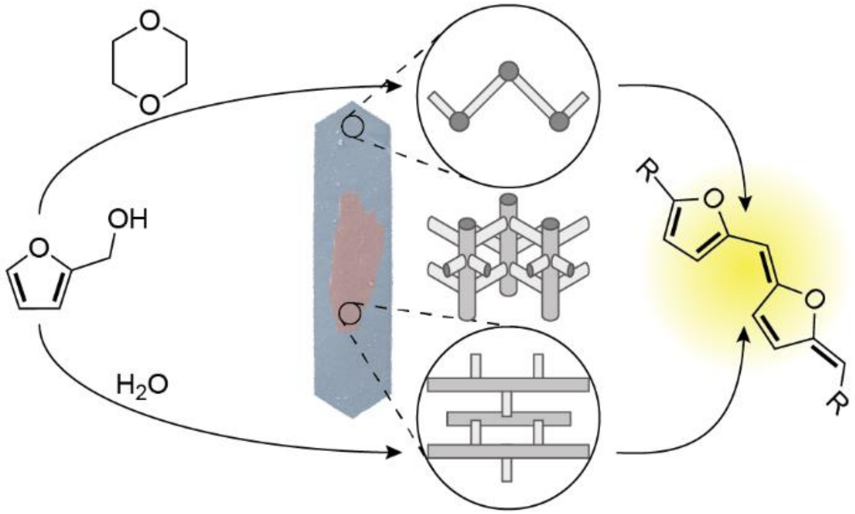

Abstract

Molecular-sized micropores of ZSM-5 zeolite catalysts provide spatial restrictions around catalytic sites that allow for shape-selective catalysis. However, the fact that ZSM-5 has two main pore systems with different geometries is relatively unexploited as a potential source of additional shape selectivity. Here, we use CLSM to show that by changing the polarity of the solvent, the acid-catalyzed furfuryl alcohol oligomerization can be directed to selectively occur within either of two locations in the microporous network. This finding is confirmed for H-ZSM-5 particles with different Si/Al ratios and indicates a general trend for shape-selective catalytic reactions.

http://pubs.acs.org/doi/abs/10.1021/acscatal.7b00782

Contributions

The main part of the experimental work and article writing was performed by Alexey Kubarev. Maarten Roeffaers and Alexey Kubarev designed the experiments. Alexey Kubarev supported by Jordi Van Loon and Arunasish Layek performed the CLSM measurements, Guillaume Fleury performed the Raman experiments. Eric Breynaert, Sambhu Radhakrishnan, and Johan Martens are responsible for the NMR. measurements. All authors were involved in data interpretation and article writing.

CHAPTER 4 – SOLVENT POLARITY-INDUCED PORE SELECTIVITY IN H-ZSM-5 CATALYSIS

4.1 INTRODUCTION

Zeolites are the most commonly used heterogeneous catalysts in the (petro)chemical industry.[1–3] Since the middle of the 20th century, they have been extensively studied and applied in industrial processes because of their unique combination of extensive microporosity and the intrinsic strong acidity of their hydrogen form. This combination enables them to achieve both high catalytic activity and high chemical selectivity.

One of the most important and widely used types of zeolite catalysts is the hydrogen form of ZSM-5 (MFI framework type). H-ZSM-5 is industrially used in fluid catalytic cracking,[4] the synthesis of ethylbenzene,[5,6] the isomerization of xylenes,[6] and the disproportionation of toluene.[6,7] Also, it is often looked upon as the prototype of a shape-selective catalysts because of its high para-selectivity toward the alkylation of alkylbenzenes.[3] More recently, with a focus on environmentally sustainable processes, there were numerous and promising studies regarding the activity and shape selectivity of H-ZSM-5 in the catalytic conversion of biomass and its derivatives.[8–11] For example, it was shown that ZSM-5 exhibited the highest aromatic yield and the least amount of coking among 13 zeolites with different pore sizes and shapes when applied in the fast catalytic pyrolysis of glucose.8

The MFI framework consists of two types of intersecting 10-membered-ring pores. The geometry and size of these perpendicular pores differ: one type consists of straight channels with a size of 5.3 × 5.6 $Å^2$, running along the crystallographic *b*-axis, the other has a tortuous shape, commonly referred to as the sinusoidal channels, with a size of 5.1 × 5.5 $Å^2$, running along the crystallographic *a*-axis.[12,13] Such differences in pore size and local environment can trigger different adsorption properties between the two types of pores. For example, it has been shown that aromatic molecules, such as *p*-xylene, *p*-dichlorobenzene, and *trans*-stilbene, preferentially adsorb at different locations of the framework depending not only on the adsorbate nature but also on the adsorbate loading.[14–19] Techniques such as single-crystal X-ray diffraction and high-resolution synchrotron X-ray powder diffraction showed that at low loadings, the adsorbate molecules are preferentially located inside in the straight pores of ZSM-5 crystals,[14–16] whereas at high loadings, they accumulate at pore intersections and in the sinusoidal pores.[18,19] In addition, Eckman et al. used deuterium solid-state NMR spectroscopy to trace temperature-dependent changes in orientation of *p*-xylene molecules in H-ZSM-5 at low loadings. They concluded that molecules are neither able to move from the straight channels into the sinusoidal channels nor move along the sinusoidal channels.[17]

Such differences in molecular adsorption and transport should influence the catalytic processes. However, given the increased complexity of the chemical reaction system compared with adsorption and diffusion, it has proven to be not straightforward to study the molecular orientation during catalytic conversions inside zeolite crystals. Luckily, catalysis characterization has benefitted from the development and application of powerful microscopy techniques in recent years, such as fluorescence and optical microspectroscopy.[20,21] They allow the monitoring of molecular processes inside a single catalyst crystal, for example to determine the exact location of catalytic conversions. Additionally, they can resolve the orientation of reaction products with respect to the crystalline porous network by using linearly polarized excitation light. These techniques were successfully applied to study H-ZSM-5 catalysts and their activity where other microscopic techniques failed. For example, the early attempt to use polarized FTIR to study the location of adsorbates in single ZSM-5 crystals was hampered by crystal twinning or intergrowth, which could not be resolved by infrared microscopy.[22] Later on, numerous fluorescence, optical and electron microscopic investigations discerned the intergrowth structure of ZSM-5 crystals and the crystallographic orientation of the subcrystal units.[23–28]

In the case of the ZSM-5 crystals used in this study, a pronounced intergrowth is present in the main body of the coffin-shaped H-ZSM-5 particles (**Figure 4.1a**). Such 90 deg intergrowths are commonly observed in ZSM-5 crystals and were previously also observed in this specific sample.[26,28] The crystallographic *c*-axis aligns with the longest particle dimension both for the main crystal body and the intergrowth. However, in the intergrowth (pink area in **Figure 4.1a**) the crystallographic *a*- and *b*-axes are rotated 90° around the *c*-axis with respect to the main crystal body (blue area in **Figure 4.1a**). As a consequence, the orientation of the straight and sinusoidal pores is swapped between the main body and the intergrowth of the crystal. This property can be exploited to reveal differences in reactivity between the two pore structures, as the orientation of the acid-catalyzed reaction products can be identified by using linear polarized excitation light (see below). Because pore systems are oriented perpendicularly to each other, differences in reactivity should be easy to identify.

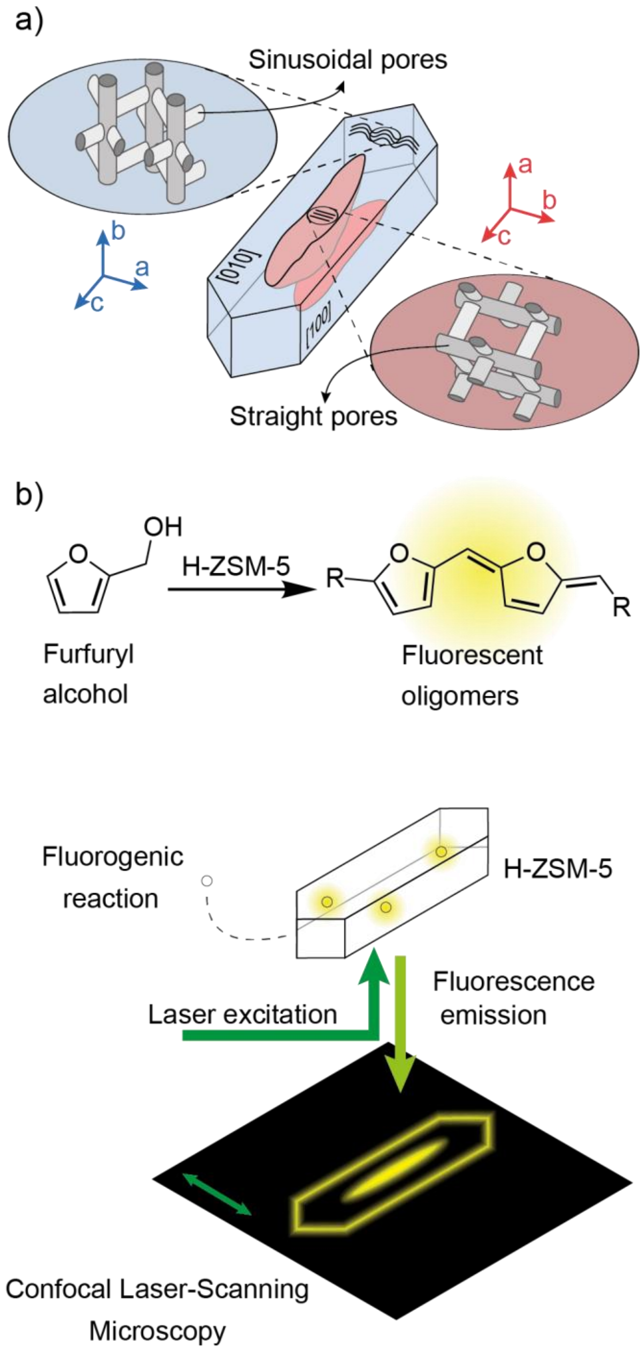

Figure 4.1. Schematic representation of (a) the intergrowth structure of a ZSM-5 crystal and the relative pore orientations and (b) the used fluorescence microscopy approach. The green two-headed arrow indicates the orientation of the applied light polarization.

As mentioned earlier, it has been described in the literature that the pore preference of *p*-dichlorobenzene depends on the adsorbate loading.[14,18] On this basis, we speculated that it should be possible to affect the pore preference of the catalytic reaction and direct the reaction to predominantly happen in one of both pore types. Numerous microspectroscopic studies have been conducted in the past to investigate the factors affecting catalytic activity of H-ZSM-5, such as its relation with the subcrystalline intergrowth structure,[24–26,29–33] the effect of commonly applied steaming treatments,[34,35] the mechanisms of coke formation,[36] and the solvent effect.[37] In particular, the choice of solvent has been shown to significantly affect the catalytic activity of H-ZSM-5 crystals in the styrene dimerization reaction, as solvents with a different polarity interact differently with zeolite Brønsted acid sites.[37] On the basis of these considerations, we hypothesized that by using different solvents the pore preference of a catalytic reaction could also be affected.

4.2 RESULTS AND DISCUSSION

In this work, this hypothesis was investigated by comparing the effect of a polar solvent, water, to that of the more apolar, 1,4-dioxane. Earlier, both of these solvents were shown to be appropriate to study acid zeolite catalysis with our chosen probe reaction (i.e., the furfuryl alcohol oligomerization),[24,38] but they differ significantly in polarity (spectroscopic polarity indices are 1.000 for water, 0.164 for 1,4-dioxane, and 0.605 for furfuryl alcohol).[39]

We applied the furfuryl alcohol oligomerization as model reaction (**Figure 4.1b, Figure 8.1**) which catalytically stains zeolite crystals with fluorescent products. Subsequently, CLSM detects these fluorescent reaction products, enabling a differentiation between zones within single H-ZSM-5 crystals based on their catalytic performance (**Figure 4.1b**). The molecular orientation of the fluorescent reaction products, and therefore the type of pore in which they are formed, was revealed using linearly polarized excitation light. Under these conditions, only fluorescent species with their dipole moment oriented along the polarization direction of the incident light (indicated by the green two-headed arrow on the figures) are efficiently excited.

In our experiments, we used four H-ZSM-5 samples with experimentally determined Si/Al ratios of 880, 82, 75, and 27, respectively, designated H-ZSM-5-880, H-ZSM-5-82, H-ZSM-5-75, and H-ZSM-5-27. In the main article we present experimental data related only to the H-ZSM-5-880 sample, whereas the results for other samples are given in the Supporting Information.

The CLSM micrographs of the catalytically stained H-ZSM-5-880 crystals lying on their [010] plane surfaces (based on the crystallographic structure of the main body) are presented in **Figure 4.2**. In this orientation, the main crystal body has sinusoidal pores running parallel compared to the excitation light polarization orientation, while its straight pores run perpendicular to the presented image plane and lie along the direction of the light propagation.

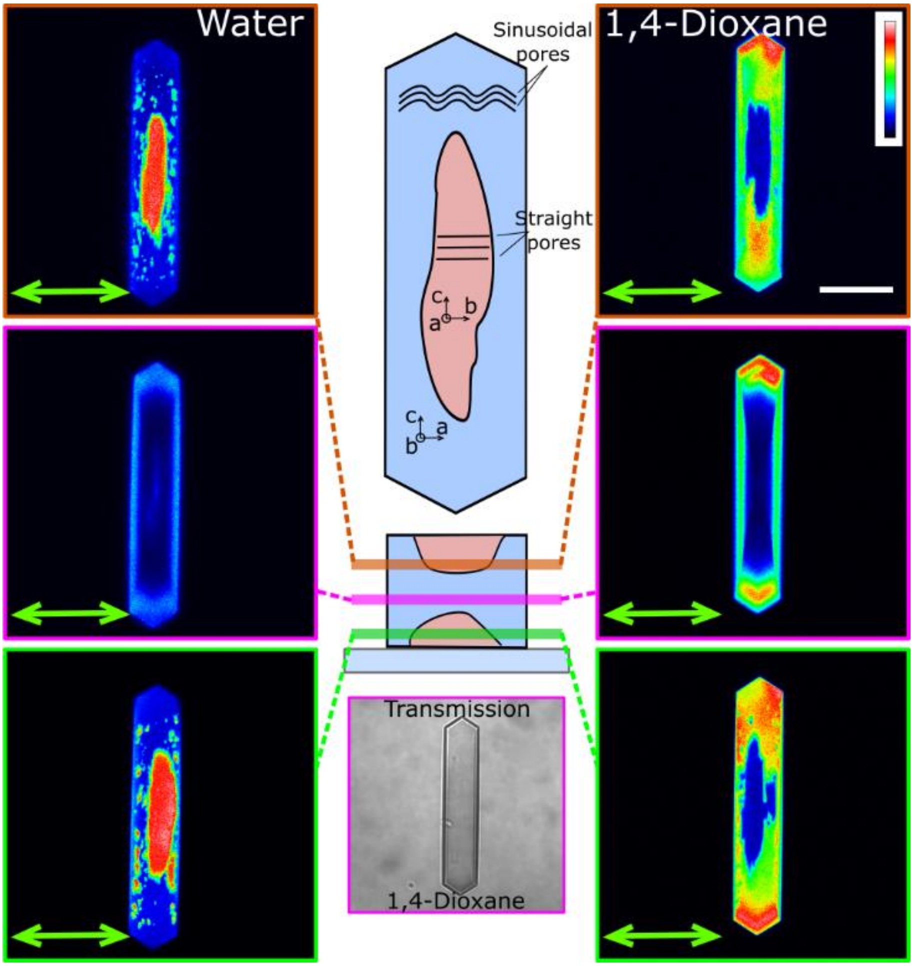

Figure 4.2. CLSM micrographs of furfuryl alcohol oligomers accumulated at different depths within H-ZSM-5-880 crystals (lying on the [010] facet) using water (left) or 1,4-dioxane (right) as a solvent. Transmission image is presented from the 1,4-dioxane based experiment. False color scale shows the observed fluorescence intensity adjusted for each slide; the green two-headed arrow indicates the excitation light polarization orientation; scale bar: 20 μm.

In the intergrowth, the opposite is true – the straight pores are coaligned with the excitation light polarization orientation, while the sinusoidal pores lie along the line of observation.

We observed that fluorescent molecules are accumulated in the straight pores of the intergrowth when water is used as solvent, whereas reactions take place in the sinusoidal pores in the main body of the crystal in 1,4-dioxane. We conclude that, in line with our expectations, the type of pores in which the reaction takes place can be controlled on the basis of the solvent.

However, it is possible that our observations highlight differences in activity between the intergrowth and main body of the crystal, rather than between the straight and sinusoidal pores. In order to confirm our results, we have conducted CLSM microscopic imaging of crystals lying on their [100] facet (based on the crystallographic structure of the main body). In this orientation, the straight pores of the main body and sinusoidal pores of the intergrowth are coaligned with the excitation light polarization orientation. The micrographs presented in **Figure 4.3** confirm that without regard to main body or intergrowth 1,4-dioxane promotes catalytic activity in sinusoidal pores, whereas water promotes the reaction to occur mainly in the straight pores.

We observed the same effect in two other batches: H-ZSM-5-82 and H-ZSM-5-27 (**Figures 4.S1-4.S4**). H-ZSM-5-75 showed a slightly deviating picture. While the reaction is also highly favored in the straight pores when using water as a solvent, the product formation shows a weak preference toward the straight pores as well when 1,4-dioxane is used (**Figures 4.S5-4.S6**).

A possible explanation for the observed solvent-dependent pore preference may be sought in the differences in solvent polarity and its interaction with the zeolite pores of different polarity. Pore polarity differences can be caused by (1) the uneven distribution of framework aluminum and the associated acid sites or (2) by differences in defect silanols in straight versus sinusoidal pores. As the pore preference effect appears to be independent of the Si/Al ratio and is even observed in Al-poor H-ZSM-5-880 sample, we rule out that framework aluminum distribution is the main cause for polarity differences. To investigate the possibility of silanol groups affecting pore polarity, we have conducted ^{1}H magic-angle spinning (MAS) NMR spectroscopy investigation of H-ZSM-5-880 (Supporting Information and **Figures 4.S8-4.S10**),[40] which revealed an estimated minimal concentration of silanol groups as Si/SiOH ratio of 82. The actual silanol concentration is even higher as even in the calcined sample traces of water were present; water in exchange with silanols decreases the detected silanol signal. This concentration of silanols is in line with earlier reports.[41,42]

Controlled addition of water shows the strong interaction with these silanols indicative for a high local polarity. From these ^{1}H MAS NMR spectroscopy data in combination with the CLSM observations we conclude that there is a silanol-induced polarity which is potentially different between the sinusoidal and straight pores with silanols being preferentially present in the sinusoidal pores.

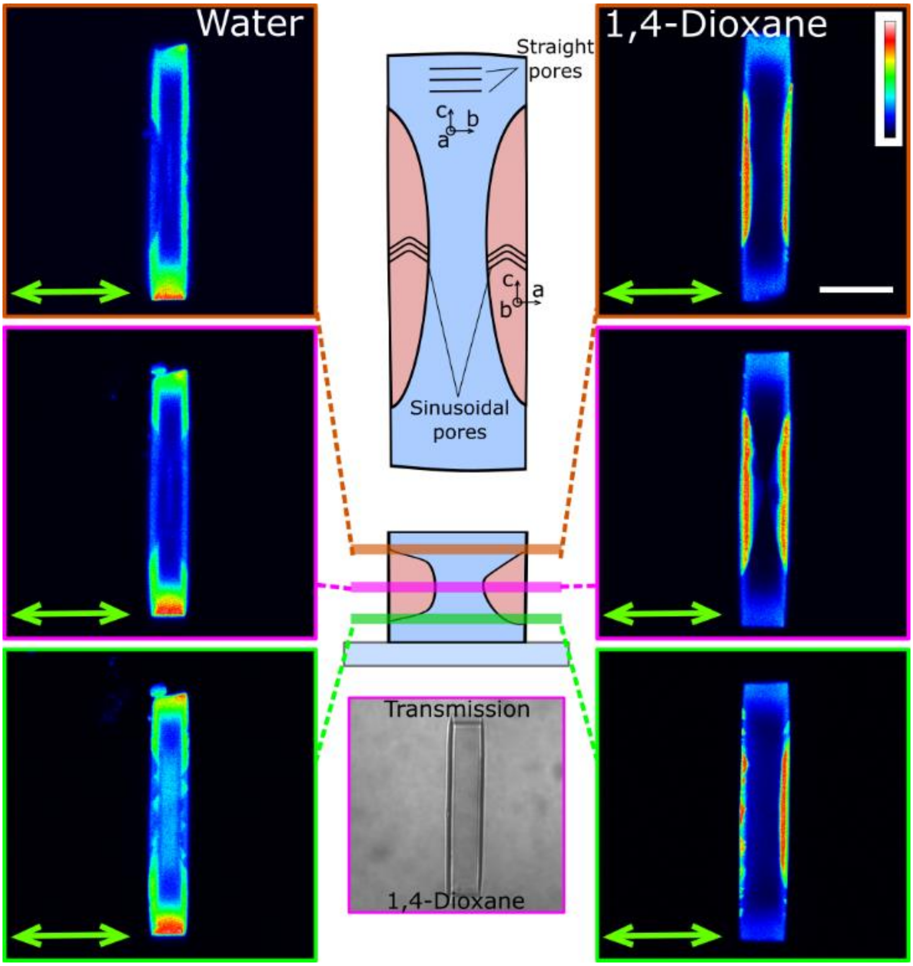

Figure 4.3. CLSM micrographs of furfuryl alcohol oligomers accumulated at different depths within H-ZSM-5-880 crystals (lying on the [100] facet) using water (left) or 1,4-dioxane (right) as a solvent. Transmission image is presented from the 1,4-dioxane based experiment. False color scale shows the observed fluorescence intensity adjusted for each slide; the green two-headed arrow indicates the excitation light polarization orientation; scale bar: 20 µm.

Hence, the enhanced polarity of the sinusoidal pores compared with the straight pores can lead to differences in the respective coadsorption dynamics for solvent-furfuryl alcohol systems: the more polar molecules in the system will preferentially adsorb in the sinusoidal pores and the more apolar in the straight pores. This preferential molecular absorption was further confirmed by the distribution of the apolar benzonitrile molecules, which are preferentially adsorbed along the straight pores of the H-ZSM-5-880 as revealed by SRS microscopy (**Figure 4.S11**).

To further support this model that the acid catalysis in ZSM-5 is strongly influenced by differences in pore polarity and the preferential molecular adsorption, we tested another apolar solvent 2-butanone, similar in polarity to 1,4-dioxane. With a spectroscopic polarity index of 0.327, 2-butanone is more apolar than furfuryl alcohol.[39] The results of these experiments are presented in **Figure 4.4**.

The measured catalytic activity patterns confirm that the activity is mostly restricted to sinusoidal pores of H-ZSM-5, similar to the reaction in 1,4-dioxane and opposite to what is observed in water. These results support our proposed model that the observed solvent-induced pore preference is indeed guided by the solvent polarity and the related molecular adsorption based on pore polarity.

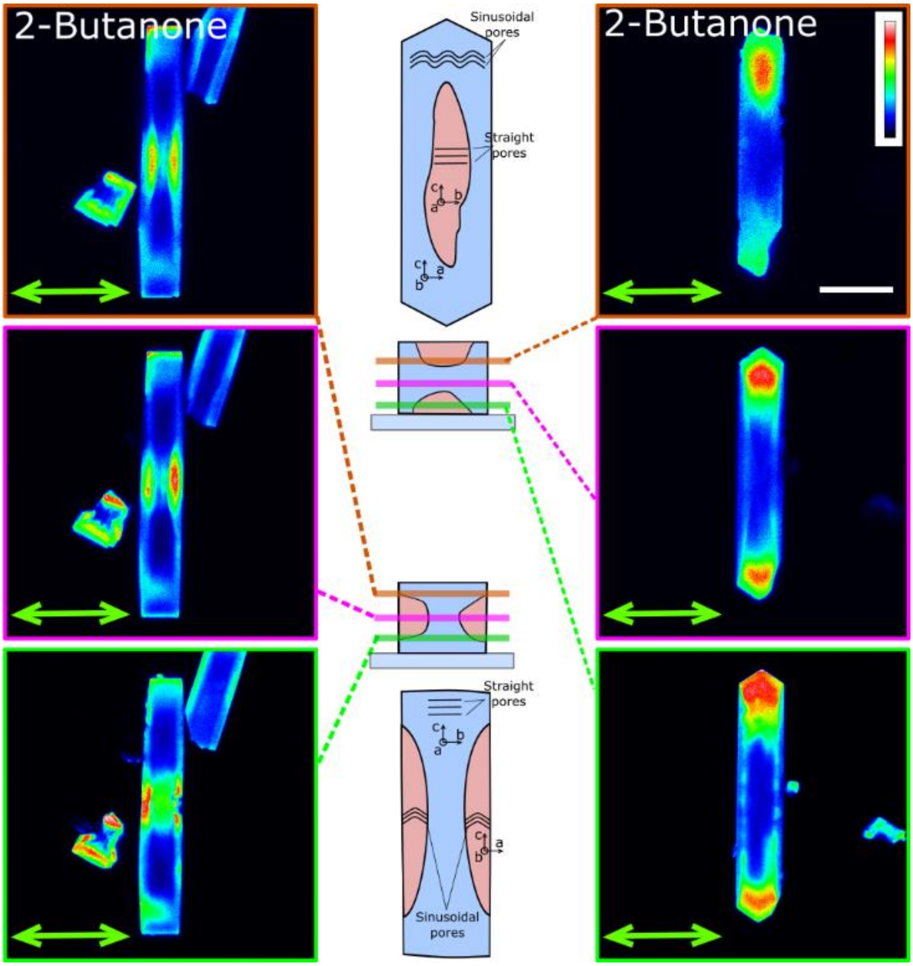

Figure 4.4. CLSM micrographs of furfuryl alcohol oligomers accumulated at different depths within H-ZSM-5-880 crystals lying on the [100] (left) and [010] (right) facet using 2-butanone as a solvent. False color scale shows the observed fluorescence intensity adjusted for each slide; the green two-headed arrow indicates the excitation light polarization orientation; scale bar: 20 μm.

4.3 CONCLUSIONS

In conclusion, the presented work shows that differences in solvent and reagent polarity can be employed to steer the catalytic activity toward the straight or sinusoidal pores in H-ZSM-5. This effect is likely related to the intrinsic presence of silanol defects. CLSM in combination with furfuryl alcohol oligomerization as probe reaction shows that this acid-catalyzed reaction preferentially occurs in the straight pores of H-ZSM-5 crystals if water is used as solvent and in the sinusoidal pores if the more apolar 1,4-dioxane or 2-butanone are used. Additional ^{1}H MAS NMR spectroscopy and SRS microscopy with probe molecules support the proposed model, which relates the observed pore preference to a difference in polarity between straight and sinusoidal pores as result of silanol defects.

4.4 EXPERIMENTAL SECTION

4.4.1 **Materials**

Materials: H-ZSM-5-880 sample was prepared according to method (V) from the paper of Müller and Unger, with gel composition $8TPABr/123(NH_4)_2O/Al_2O_3/1460SiO_2/2280H_2O$ and crystallization for 7 days at 180°C.[43] H-ZSM-5-82 sample was prepared according to method (IV) from the same paper, with gel composition $8TPABr/123(NH_4)_2O/Al_2O_3/80SiO_2/2280H_2O$ and crystallization for 7 days at 180°C.[43] H-ZSM-5-75 sample was prepared according to a method described by Chen et al. with intended Si/Al = 94.[44] Medium-silica H-ZSM-5-27 sample (NH_4-form, Si/Al ratio = 27, supplier name SM-55) was obtained from AlSi-Penta Zeolithe GmbH. 98% pure furfuryl alcohol (Sigma-Aldrich) was additionally purified by vacuum distillation prior to experiments. 1,4-dioxane (99.8%) was purchased from Sigma-Aldrich. 2-butanone (99%) was purchased from Acros Organics. MilliQ water was obtained from water purification system Synergy UV (Merck Millipore).

4.4.2 **CLSM**

Prior to the catalytic staining and microscopy experiments, samples were deposited in small vials and calcined in an ashing furnace LVT 3/11 (Nabertherm) in three stages. First the samples were heated to 80°C (1°C/min) and kept at this temperature for 1 h in order to remove easily desorbing molecules. Next, they were heated to 120°C (1°C/min) and kept at this temperature for 1 h to remove physisorbed water, minimizing undesirable hydrothermal dealumination. Finally, the samples were heated to 450°C (1°C/min) and subsequently kept at this temperature for 50 h to remove fluorescent contaminants. After allowing samples to cool, they were immediately used in catalytic staining experiments to prevent re-adsorption of fluorescent contaminants from the environment. Furfuryl alcohol oligomerization was used as a fluorogenic reaction. Portions of 0.5 mg zeolite samples were added to 1 ml of an appropriate solvent-furfuryl alcohol mixture (furfuryl alcohol content 10% vol) and left to react for 65 hours under magnetic stirring at room temperature. Stained zeolite samples were spin-coated on a clean #1 cover glass and sealed to polytetrafluoroethylene container via a silicone rubber gasket. As immersion media, 1 ml of the respective solvent was added. Confocal fluorescence images were acquired using a FluoView FV1000 (Olympus) with an oil immersion objective lens (100×, 1.4 NA, Olympus) and λ_{exc} = 532 nm, λ_{em} = 545-645 nm. Further image analysis and processing was performed with ImageJ v.1.49i software (NIH).

4.4.3 Elemental Analysis

A Varian 720-ES (simultaneous inductively coupled plasma optical emission spectrometry with axially viewed plasma) (Varian Inc.) supplied with double-pass glass cyclonic spray chamber, concentric glass nebulizer SeaSpray (Glass Expansion) and “high solids” torch was used. The instrument features a Cooled Cone Interface, echelle monochromator and custom-designed Vistachip CCD detector (Agilent) mounted on a triple-stage Peltier device and cooled to -35°C. The instrument provides true simultaneous measurements and full wavelength coverage from 167 to 785 nm, given its ability to determination of a series of elements from one single run. Solutions were presented to the spectrometer using the Varian SPS3 Sample Preparation System (Varian Inc.).

4.4.4 Thermogravimetric Analysis (TGA)

H-ZSM-5-88050 mg samples were catalytically stained with 20 ml of 10% vol furfuryl alcohol-water/1,4-dioxane mixture for 65 hours under magnetic stirring at room temperature. After they were dried at 40°C for 30 minutes and analyzed in TGA Q500 V6.7 Build 203 (TA instruments) with platinum pan. The TGA method was the following: 5°C/min heating ramp to 800°C in O2 atmosphere.

4.4.5 ^{1}H MAS NMR Spectroscopy

^{1}H NMR experiments were performed at 298 K (BCU II) using a standard bore Bruker AVANCE III HD spectrometer operating at 500.87 MHz with a H/X/Y CP-MAS probe. Data collection was performed at spinning speeds of 10 kHz, using a $\pi/2$ flip angle, a repetition delay of 5 s and chemical shift referencing with respect to TMS, using adamantane (chemical shift δ = 1.773 ppm) as secondary reference. To exclude fast-relaxing background signals originating from the probe, linear back-prediction of the FID-signal was performed using Bruker Topspin 3.5 software. The evolution of the ^{1}H NMR spectra of H-ZSM-5-880 with increasing water and dioxane content are shown in **Figures 4.S8 and 4.S9** respectively. The ^{1}H NMR spectra were deconvoluted using DMFit software and quantified according to the method described by Houlleberghs et al.[40]

4.4.6 SRS Microscopy

The H-ZSM-5-880 crystals were spin-coated on a clean cover glass #1 from an aqueous suspension. The zeolite-loaded cover glasses were thermally treated using the same procedure used for fluorescence microscopy experiments. The samples at 450°C were quickly transferred, while hot, into a cleaned desiccator under nitrogen. After being cooled down to room temperature, the desiccator was opened to briefly add a few drops of liquid benzonitrile (99%, Sigma-Aldrich) to the samples. After 24 h and prior to measurements, the desiccator was put under vacuum (1×10^{-1} mbar) at 150°C in order to remove the excess of nitrile. The benzonitrile adsorbed in the H-ZSM-5-880 zeolites was imaged using SRS microscopy.[45,46] The experimental setup used for SRS imaging has been described elsewhere.[45]

4.5 REFERENCES

[1] N. Mizuno, M. Misono, *Chem. Rev.* **1998**, *98*, 199–218.

[2] J. Čejka, G. Centi, J. Perez-Pariente, W. J. Roth, *Catal. Today* **2012**, *179*, 2–15.

[3] J. Weitkamp, *Solid State Ionics* **2000**, *131*, 175–188.

[4] T. F. Degnan, G. K. Chitnis, P. H. Schipper, *Microporous Mesoporous Mater.* **2000**, *35–36*, 245–252.

[5] D. H. O. Jeevan S. Abichandani, Jeffrey S. Beck, Sharon B. McCullen, **1995**, *US Patent 5689025 A*.

[6] J. Weitkamp, L. Puppe, *Catalysis and Zeolites*; Springer Berlin, Heidelberg, Germany, **1999**.

[7] W. Kaeding, *J. Catal.* **1981**, *69*, 392–398.

[8] J. Jae, G. A. Tompsett, A. J. Foster, K. D. Hammond, S. M. Auerbach, R. F. Lobo, G. W. Huber, *J. Catal.* **2011**, *279*, 257–268.

[9] G. M. González Maldonado, R. S. Assary, J. Dumesic, L. A. Curtiss, *Energy Environ. Sci.* **2012**, *5*, 6981.

[10] M. A. Mellmer, J. M. R. Gallo, D. Martin Alonso, J. A. Dumesic, *ACS Catal.* **2015**, *5*, 3354–3359.

[11] T. M. Lima, C. G. S. Lima, A. K. Rathi, M. B. Gawande, J. Tucek, E. A. Urquieta-González, R. Zbořil, M. W. Paixão, R. S. Varma, *Green Chem.* **2016**, *18*, 5586–5593.

[12] G. T. Kokotailo, S. L. Lawton, D. H. Olson, W. M. Meier, *Nature* **1978**, *272*, 437–438.

[13] D. H. Olson, G. T. Kokotailo, S. L. Lawton, W. M. Meier, *J. Phys. Chem.* **1981**, *85*, 2238–2243.

[14] H. van Koningsveld, J. C. Jansen, A. J. M. de Man, *Acta Crystallogr. Sect. B Struct. Sci.* **1996**, *52*, 131–139.

[15] J. B. Parise, J. A. Hriljac, D. E. Cox, D. R. Corbin, V. Ramamurthy, *J. Chem. Soc. Chem. Commun.* **1993**, 226–228.

[16] H. Gies, B. Marler, C. Fyfe, G. Kokotailo, Y. Feng, D. E. Cox, *J. Phys. Chem. Solids* **1991**, *52*, 1235–1241.

[17] R. R. Eckman, A. J. Vega, *J. Phys. Chem.* **1986**, *90*, 4679–4683.

[18] H. van Koningsveld, J. C. Jansen, H. van Bekkum, *Acta Crystallogr. Sect. B Struct. Sci.* **1996**, *52*, 140–144.

[19] H. van Koningsveld, F. Tuinstra, H. van Bekkum, J. C. Jansen, *Acta Crystallogr. Sect. B Struct. Sci.* **1989**, *45*, 423–431.

[20] K. P. F. Janssen, G. De Cremer, R. K. Neely, A. V Kubarev, J. Van Loon, J. A. Martens, D. E. De Vos, M. B. J. Roeffaers, J. Hofkens, *Chem. Soc. Rev.* **2014**, *43*, 990–1006.

[21] B. M. Weckhuysen, *Angew. Chem. Int. Ed.* **2009**, *48*, 4910–4943.

[22] F. Schueth, *J. Phys. Chem.* **1992**, *96*, 7493–7496.

[23] M. B. J. Roeffaers, B. F. Sels, H. Uji-i, B. Blanpain, P. L'hoëst, P. A. Jacobs, F. C. De Schryver, J. Hofkens, D. E. De Vos, *Angew. Chem. Int. Ed.* **2007**, *46*, 1706–1709.

[24] M. B. J. Roeffaers, R. Ameloot, M. Baruah, H. Uji-i, M. Bulut, G. De Cremer, U. Müller, P. A. Jacobs, J. Hofkens, B. F. Sels, et al., *J. Am. Chem. Soc.* **2008**, *130*, 5763–5772.

[25] L. Karwacki, E. Stavitski, M. H. F. Kox, J. Kornatowski, B. M. Weckhuysen, *Stud. Surf. Sci. Catal.* **2008**, *174*, 757–762.

[26] M. B. J. Roeffaers, R. Ameloot, A.-J. Bons, W. Mortier, G. De Cremer, R. de Kloe, J. Hofkens, D. E. De Vos, B. F. Sels, *J. Am. Chem. Soc.* **2008**, *130*, 13516–13517.

[27] E. Stavitski, M. R. Drury, D. A. M. De Winter, M. H. F. Kox, B. M. Weckhuysen, *Angew. Chem. Int. Ed.* **2008**, *47*, 5637–5640.

[28] L. Karwacki, M. H. F. Kox, D. A. Matthijs de Winter, M. R. Drury, J. D. Meeldijk, E. Stavitski, W. Schmidt, M. Mertens, P. Cubillas, N. John, et al., *Nat. Mater.* **2009**, *8*, 959–965.

[29] M. H. F. Kox, E. Stavitski, J. C. Groen, J. Pérez-Ramírez, F. Kapteijn, B. M. Weckhuysen, *Chem. - A Eur. J.* **2008**, *14*, 1718–1725.

[30] M. B. J. Roeffaers, B. F. Sels, F. C. De Schryver, P. A. Jacobs, J. Hofkens, D. E. De Vos, in *Stud. Surf. Sci. Catal.*, Elsevier, **2007**, 717–723.

[31] M. H. F. Kox, E. Stavitski, B. M. Weckhuysen, *Angew. Chem. Int. Ed.* **2007**, *46*, 3652–3655.

[32] E. Stavitski, M. H. F. Kox, B. M. Weckhuysen, *Chem. - A Eur. J.* **2007**, *13*, 7057–7065.

[33] C. Sprung, B. M. Weckhuysen, *J. Am. Chem. Soc.* **2015**, *137*, 1916–1928.

[34] L. R. Aramburo, S. Teketel, S. Svelle, S. R. Bare, B. Arstad, H. W. Zandbergen, U. Olsbye, F. M. F. de Groot, B. M. Weckhuysen, *J. Catal.* **2013**, *307*, 185–193.

[35] Z. Ristanović, J. P. Hofmann, G. De Cremer, A. V. Kubarev, M. Rohnke, F. Meirer, J. Hofkens, M. B. J. Roeffaers, B. M. Weckhuysen, *J. Am. Chem. Soc.* **2015**, *137*, 6559–6568.

[36] D. Mores, E. Stavitski, M. H. F. Kox, J. Kornatowski, U. Olsbye, B. M. Weckhuysen, *Chem. - A Eur. J.* **2008**, *14*, 11320–11327.

[37] Z. Ristanović, A. V. Kubarev, J. Hofkens, M. B. J. Roeffaers, B. M. Weckhuysen, *J. Am. Chem. Soc.* **2016**, *138*, 13586–13596.

[38] K.-L. Liu, A. V. Kubarev, J. Van Loon, H. Uji-i, D. E. De Vos, J. Hofkens, M. B. J. Roeffaers, *ACS Nano* **2014**, *8*, 12650–12659.

[39] C. Reichardt, *Solvents and Solvent Effects in Organic Chemistry*, Wiley-VCH, Weinheim, Germany, **2003**.

[40] M. Houlleberghs, A. Hoffmann, D. Dom, C. E. A. Kirschhock, F. Taulelle, J. A. Martens, E. Breynaert, *Anal. Chem.* **2017**, under review.

[41] M. Hunger, J. Kärger, H. Pfeifer, J. Caro, B. Zibrowius, M. Bülow, R. J. Mostowicz, *Chem. Soc. Faraday Trans. 1* **1987**, *83*, 3459-3486.

[42] M. Hunger, D. Freude, H. Pfeifer, W. Schwieger, *Chem. Phys. Lett.* **1990**, 167, 21–26.

[43] U. Mueller, K. K. Unger, *Zeolites* **1988**, *8*, 154–156.

[44] S. Z. Chen, K. Huddersman, D. Keir, L. V. C. Rees, *Zeolites* **1988**, *8*, 106–109.

[45] K.-L. Liu, A. V. Kubarev, J. Van Loon, H. Uji-i, D. E. De Vos, J. Hofkens, M. B. J. Roeffaers, *ACS Nano* **2014**, *8*, 12650–12659

[46] C. W. Freudiger, W. Min, B. G. Saar, S. Lu, G. R. Holtom, C. He, J. C. Tsai, J. X. Kang, X. S. Xie, *Science* **2008**, *322*, 1857–1861.

SUPPORTING INFORMATION TO CHAPTER 4

4.6 SUPPORTING INFORMATION

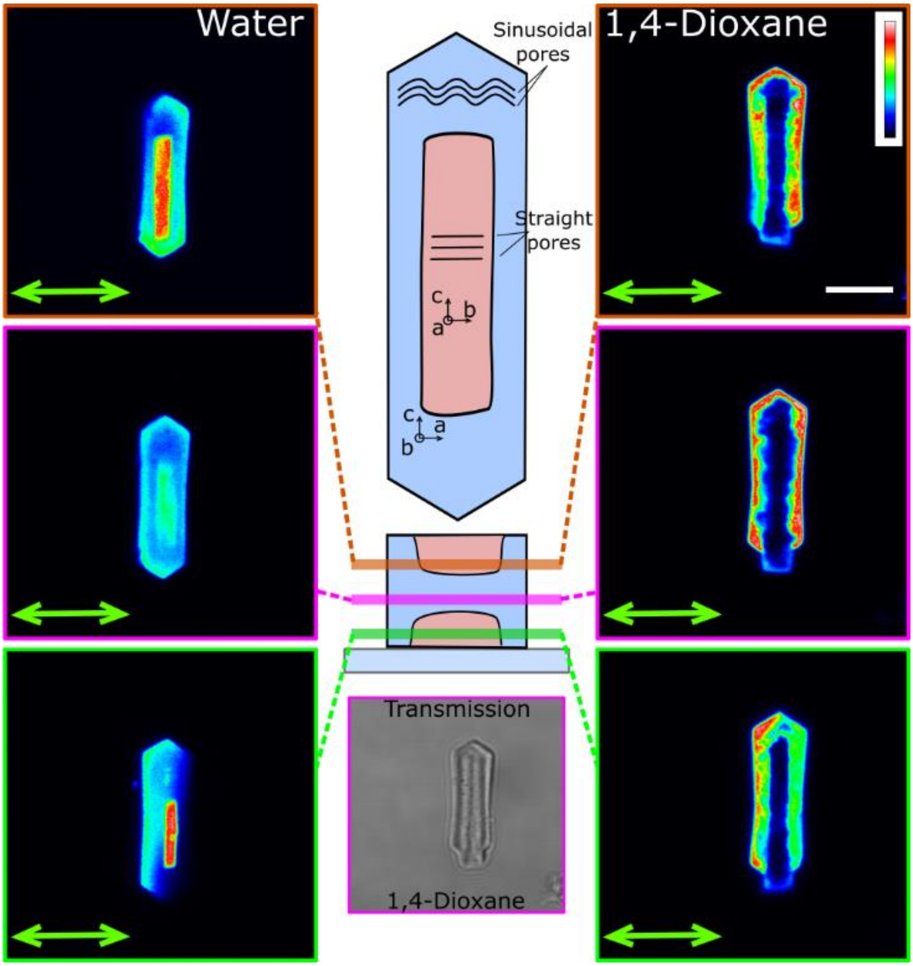

Figure 4.S1. CLSM micrographs of furfuryl alcohol oligomers accumulated at different depth within H-ZSM-5-27 crystals (lying on the [010] facet) using water (left) or 1,4-dioxane (right) as a solvent. Transmission image is presented for 1,4-dioxane based experiment. False color scale shows the observed fluorescence intensity adjusted for each slide; green arrow indicates the excitation light polarization orientation; scale bar: 5 μm.

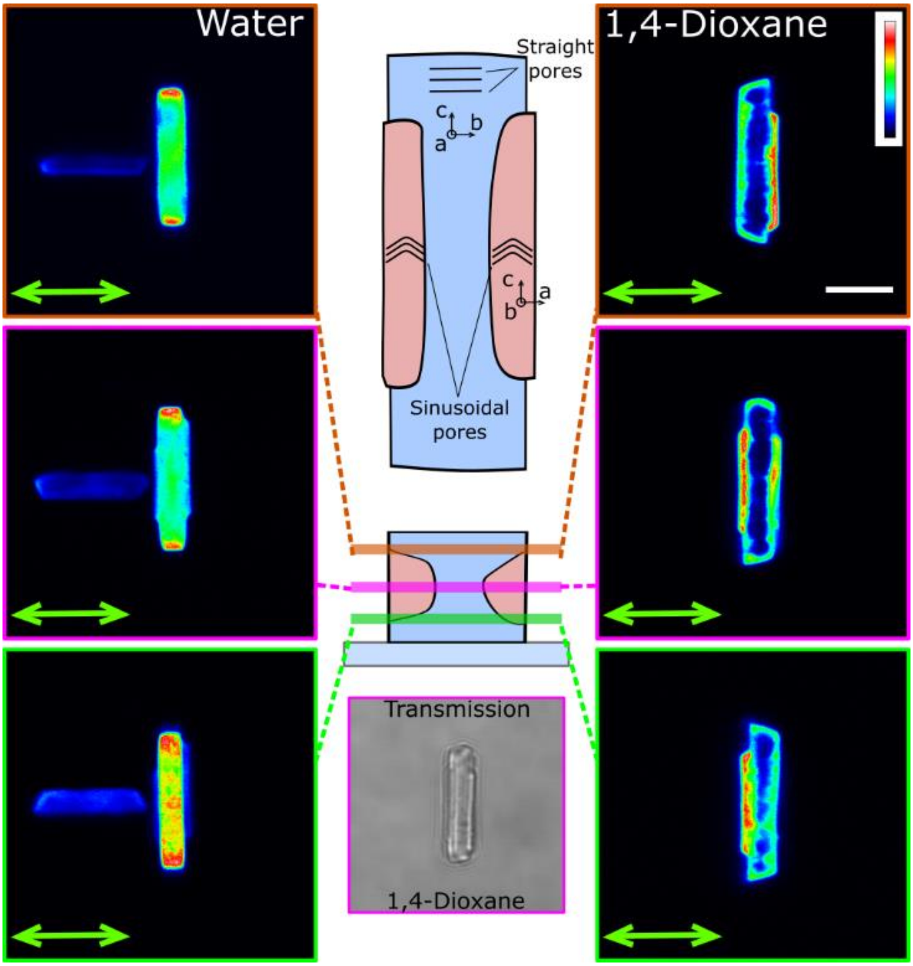

Figure 4.S2. CLSM micrographs of furfuryl alcohol oligomers accumulated at different depth within H-ZSM-5-27 crystals (lying on the [100] facet) using water (left) or 1,4-dioxane (right) as a solvent. Transmission image is presented for 1,4-dioxane based experiment. False color scale shows the observed fluorescence intensity adjusted for each slide; green arrow indicates the excitation light polarization orientation; scale bar: 5 μm.

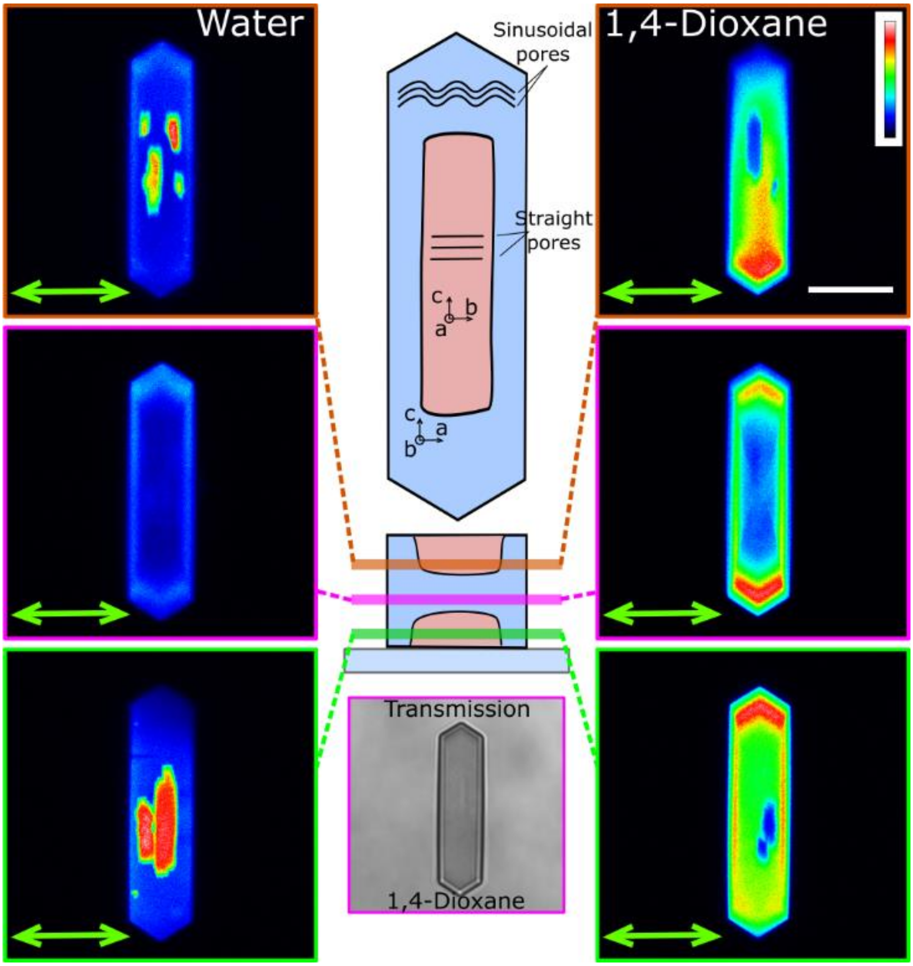

Figure 4.S3. CLSM micrographs of furfuryl alcohol oligomers accumulated at different depth within H-ZSM-5-82 crystals (lying on the [010] facet) using water (left) or 1,4-dioxane (right) as a solvent. Transmission image is presented for 1,4-dioxane based experiment. False color scale shows the observed fluorescence intensity adjusted for each slide; green arrow indicates the excitation light polarization orientation; scale bar: 10 μm.

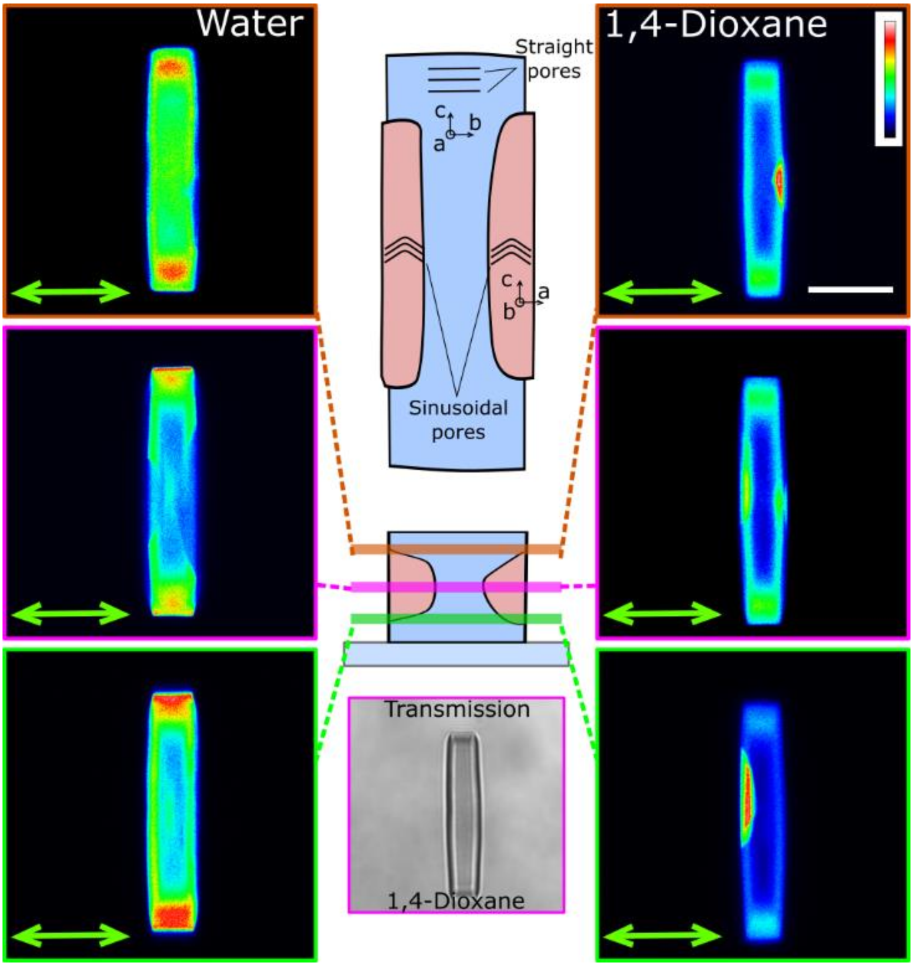

Figure 4.S4. CLSM micrographs of furfuryl alcohol oligomers accumulated at different depth within H-ZSM-5-82 crystals (lying on the [100] facet) using water (left) or 1,4-dioxane (right) as a solvent. Transmission image is presented for 1,4-dioxane based experiment. False color scale shows the observed fluorescence intensity adjusted for each slide; green arrow indicates the excitation light polarization orientation; scale bar: 10 μm.

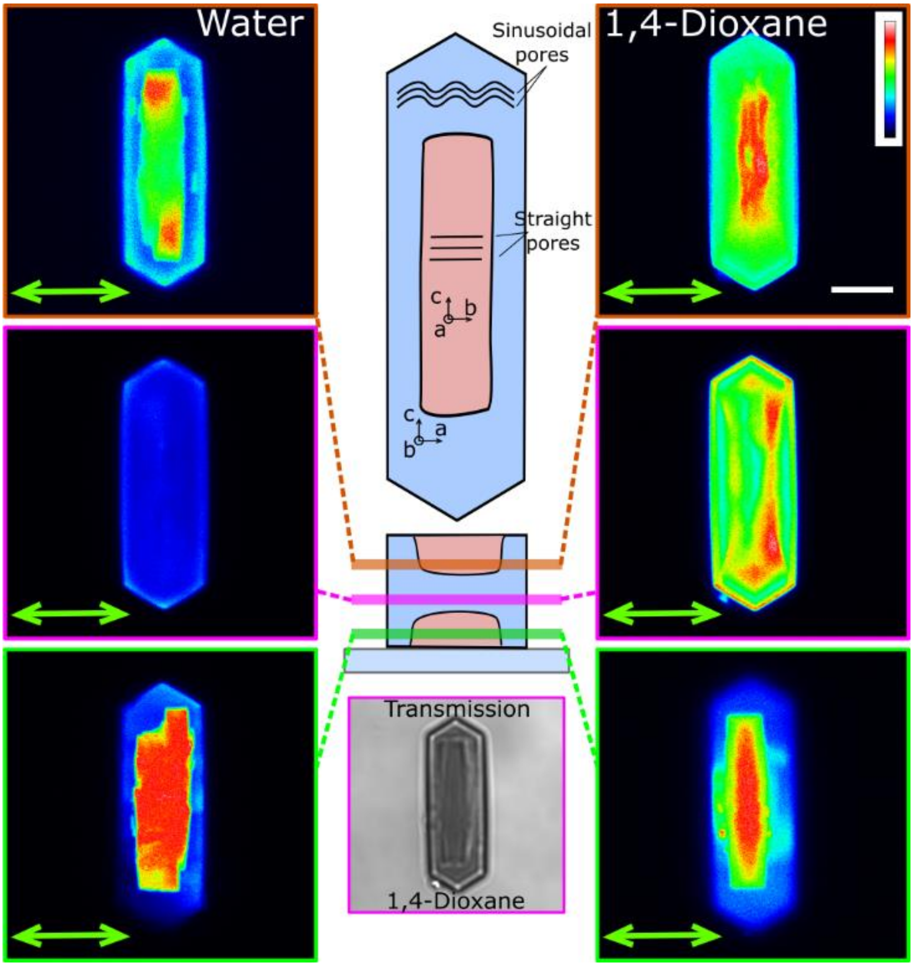

Figure 4.S5. CLSM micrographs of furfuryl alcohol oligomers accumulated at different depth within H-ZSM-5-75 crystals (lying on the [010] facet) using water (left) or 1,4-dioxane (right) as a solvent. Transmission image is presented for 1,4-dioxane based experiment. False color scale shows the observed fluorescence intensity adjusted for each slide; green arrow indicates the excitation light polarization orientation; scale bar: 5 μm.

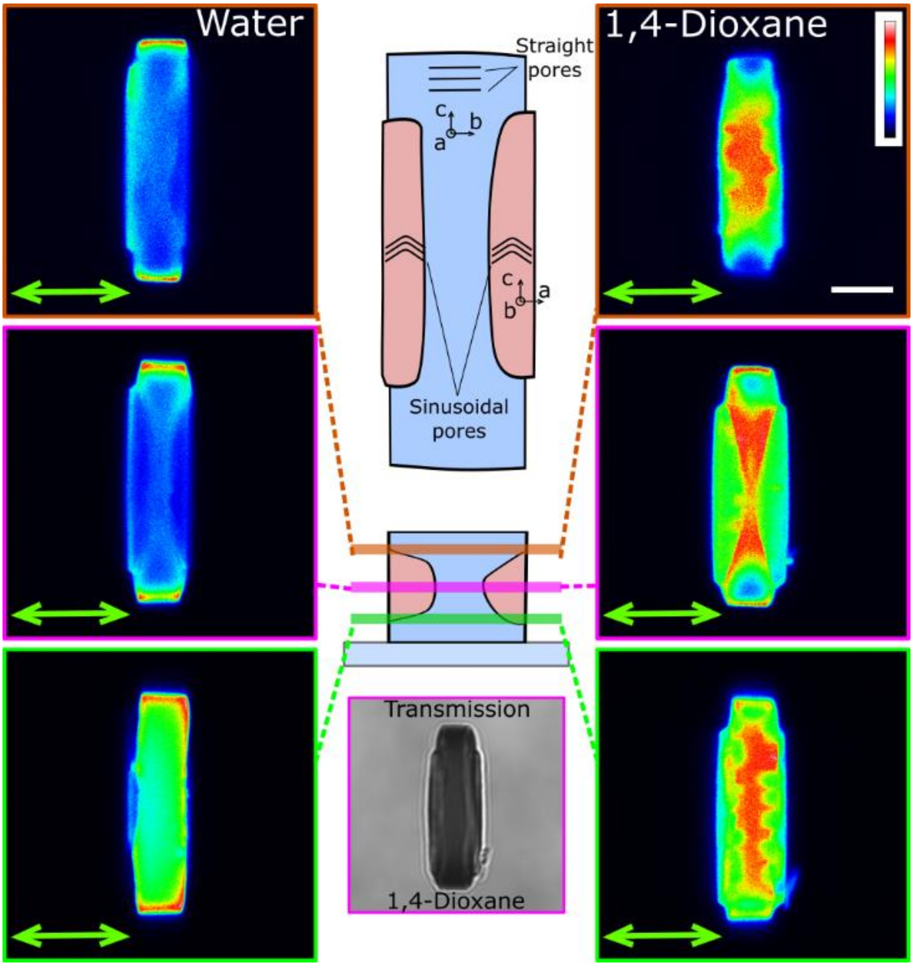

Figure 4.S6. CLSM micrographs of furfuryl alcohol oligomers accumulated at different depth within H-ZSM-5-75 crystals (lying on the [100] facet) using water (left) or 1,4-dioxane (right) as a solvent. Transmission image is presented for 1,4-dioxane based experiment. False color scale shows the observed fluorescence intensity adjusted for each slide; green arrow indicates the excitation light polarization orientation; scale bar: 5 μm.

4.6.1 TGA Investigation Results

To prove that concentrations of adsorbed solvent, reagent, and product are relevant for the catalysis, we used TGA to estimate the amounts of furfuryl alcohol and solvents adsorbed by the zeolite after being subjected to catalytic staining procedure. With TGA we have found that H-ZSM-5-880 crystals absorb up to 9.7% wt (water), 8.1% wt (dioxane), 9.3% wt (furfuryl alcohol and its oligomers, reaction in water), 3.2% wt (furfuryl alcohol and its oligomers, reaction in dioxane) (Figure S7). Hence we conclude that amounts of solvents, reactants and products absorbed are relevant to catalysis.

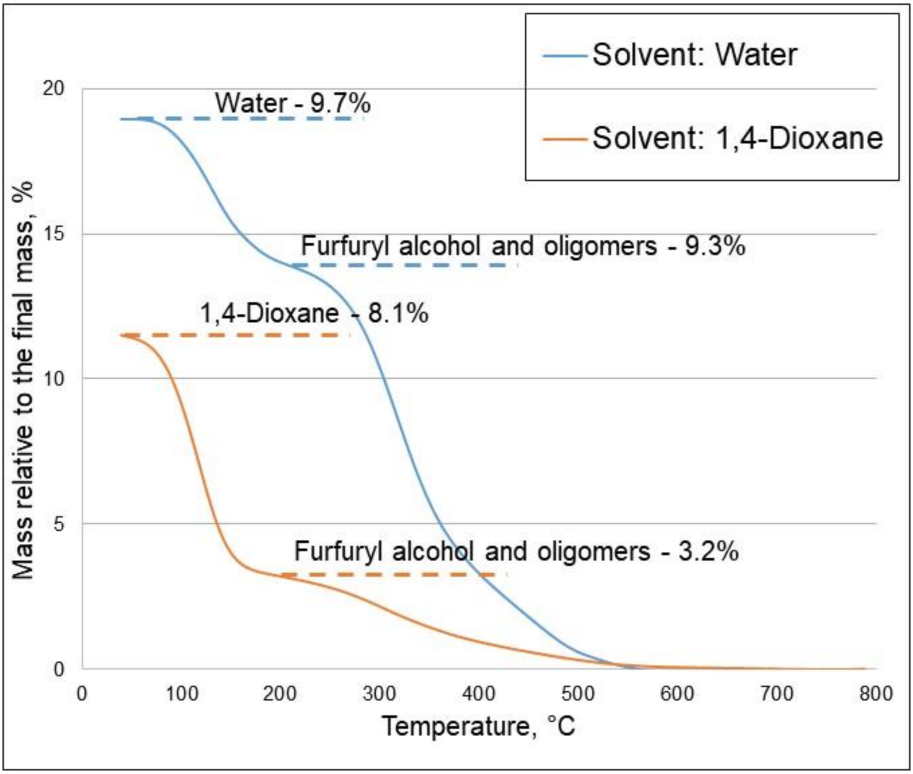

Figure 4.S7. TGA of catalytically stained H-ZSM-5-880 sample.

4.6.2 ^{1}H MAS NMR Spectroscopy Investigation Results

^{1}H MAS NMR spectroscopy investigation revealed a significant concentration of silanol groups in H-ZSM-5-880, which are strongly interacting with water already at low loadings as indicated by the significant impact of exchange phenomena on the spectra shown in **Figure 4.S8**. Although dioxane does not exhibit exchange interactions with water or silanols,[1] even in presence of dioxane the silanol signal is impacted by exchange (**Figure 4.S9**), but less extensively. Whereas in water, the silanol signal disappears due to exchange after addition of 2 mg of water to a rotor containing 47 mg of zeolite, the silanol peak was still observable as a shoulder (shifted and broadened) after addition of 15.6 mg of dioxane. The latter demonstrates that the traces of water present in dioxane and in the calcined zeolite are still in exchange with silanol and thus chemically interact with it, even when the water is strongly diluted in dioxane.

Using the calibration curve determined for water in H-ZSM-5-880 (**Figure 4.S10**), the concentration of silanol defects was estimated from the spectrum of the calcined zeolite sample. In the ^{1}H NMR spectrum for this sample (**Figure 4.S8,** green trace), two peak envelopes corresponding to silanol (~2 ppm) and water (~4.5 ppm) are visible. Quantifying the silanol-derived signal provides an estimated minimal concentration of 0.194 mmol OH per gram zeolite, which corresponds to a Si/SiOH ratio of about 82.

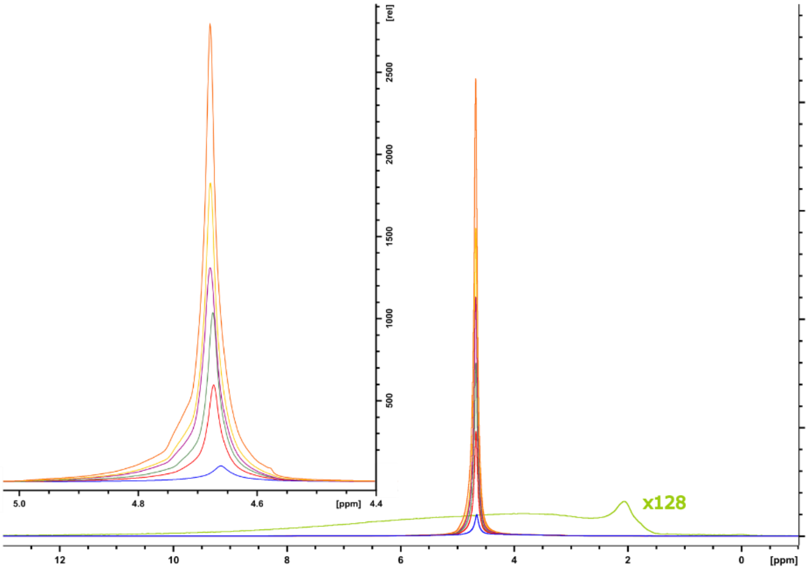

Figure 4.S8. ^{1}H MAS NMR spectra of H-ZSM-5-880 with standard addition of water (2.0, 4.6, 6.5, 8.9, 10.8, 15.8 mg H_2O added to a rotor containing 47.4 mg zeolite). The spectrum of the calcined sample without water added (green trace) was magnified with by a factor 128.

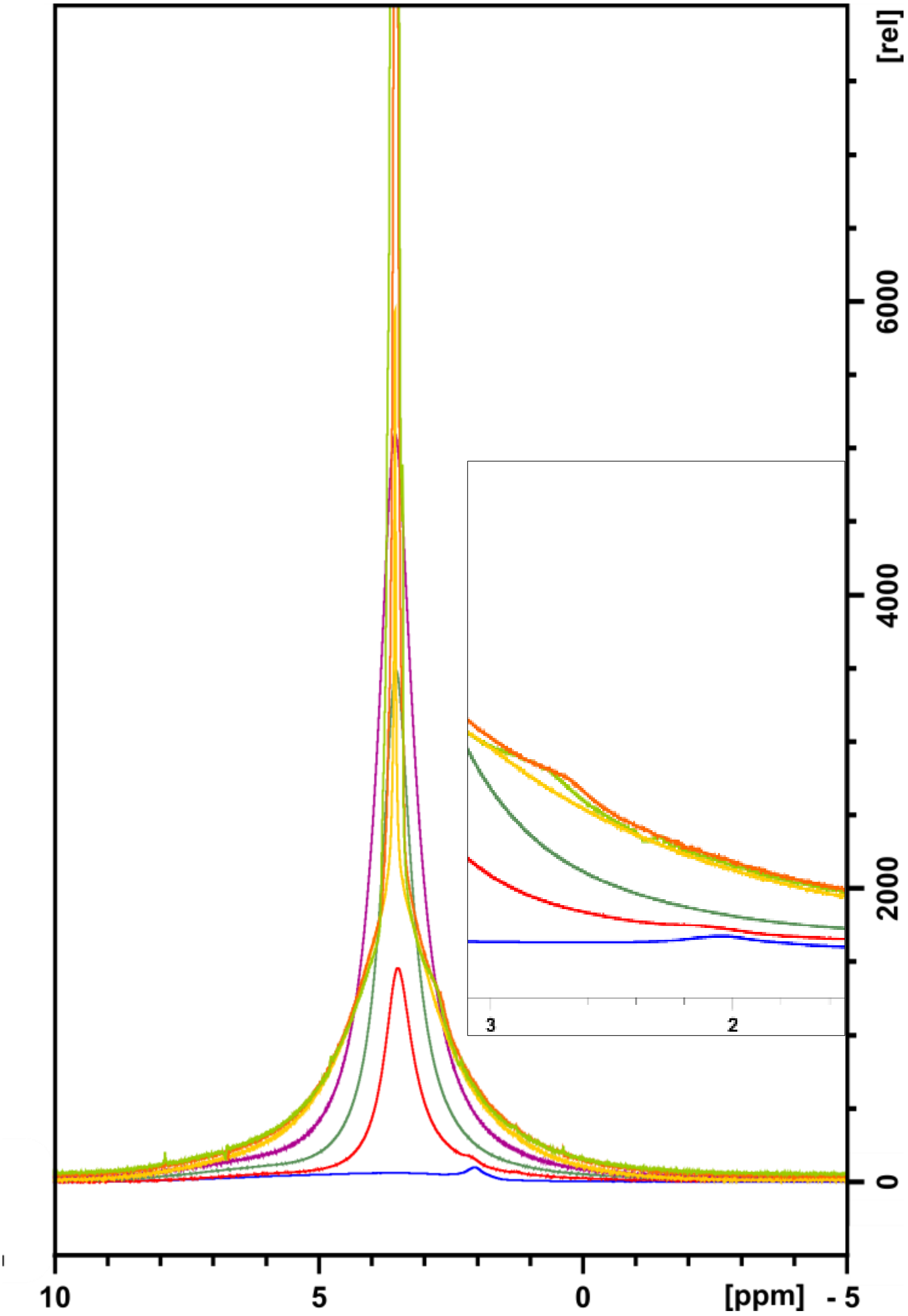

Figure 4.S9. ^1H MAS NMR spectra of H-ZSM-5-880 with standard addition of 1,4 dioxane. (2.0, 3.6, 5.6, 7.6, 9.9, 15.6 mg 1,4 dioxane added to a rotor containing 49.3 mg zeolite). Blue trace: calcined sample. The inset shows the impact of exchange on some traces, using the same colors as the main figure.

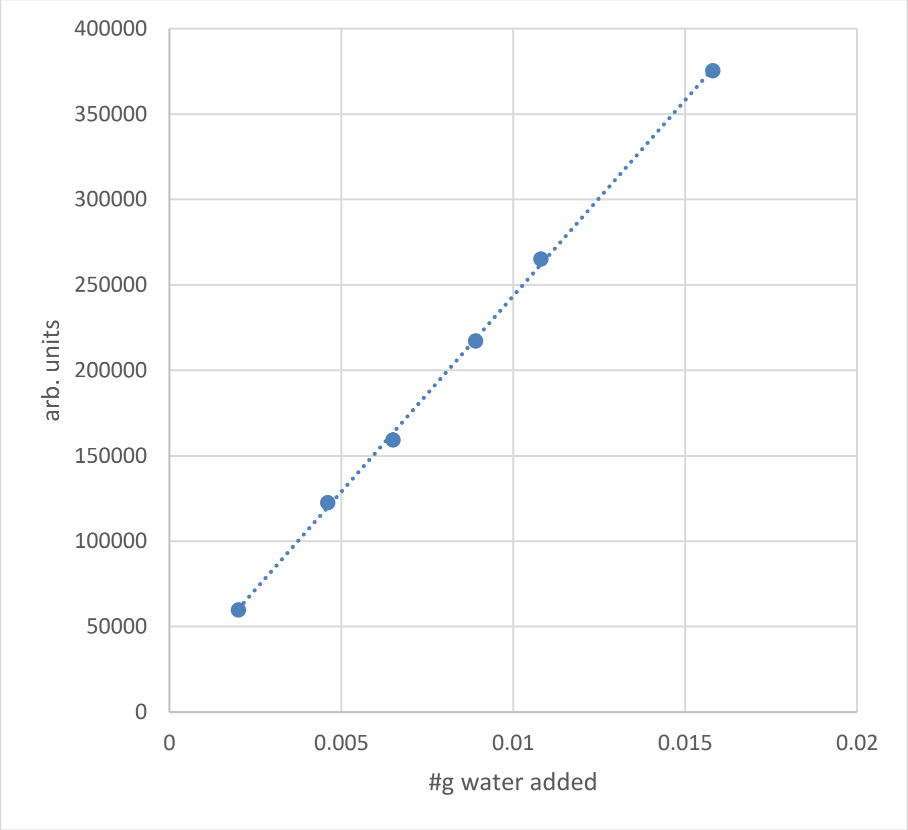

Figure 4.S10. Calibration curve for quantification of water in H-ZSM-5-880. The linear correlation (dotted line) has an R^2 = 0.9994. The calibration curve was generated and analyzed according to the method described by Houllebergths *et al.*[2]

4.6.3 SRS Microscopy Investigation Results

The vacuum treatment used during the preparation of the samples allowed to eliminate the excess of liquid benzonitrile without removing the molecules physisorbed within the pores of the zeolite crystals. The geometrical constraints of the MFI framework lead to an anisotropic orientation of the remaining adsorbed benzonitrile molecules that are tightly fitting inside the ZSM-5 pores. This well-defined orientation of the adsorbed molecules has been highlighted for ZSM-5 zeolites loaded with toluene, where the molecules are either located at the intersection of the straight and sinusoidal channels along the former, or in the sinusoidal channels.[3] We assume that benzonitrile displays a similar behavior since its dimensions are close to those of toluene. Thus, the dependence of the Raman signal associated with the stretching of the nitrile function on the orientation of the incident light polarization can be used to assess the arrangement of adsorbed benzonitrile molecules and thereby provides insights into the local pore organization. Highly sensitive chemical imaging by SRS microscopy allows to obtain this information in a spatially resolved manner.

The chemical mapping of benzonitrile molecules adsorbed in H-ZSM-5-880 lying on its [010] facets at various depths is presented in **Figure 4.S11** on the right. Two distinct regions can be observed for zeolite crystals in this orientation. The central region, corresponding to an intergrowth, where the intensity of the SRS signal is the strongest due to the presence of benzonitrile molecules along the straight channels, parallel to the incident polarization.

The chemical mapping of benzonitrile adsorbed in H-ZSM-5-880 crystals lying on their [100] face is in agreement with the results presented above (**Figure 4.S11**, left). In this case, the main crystal body shows a strong signal originating from the benzonitrile molecules located along the straight channels parallel to the incident polarization.

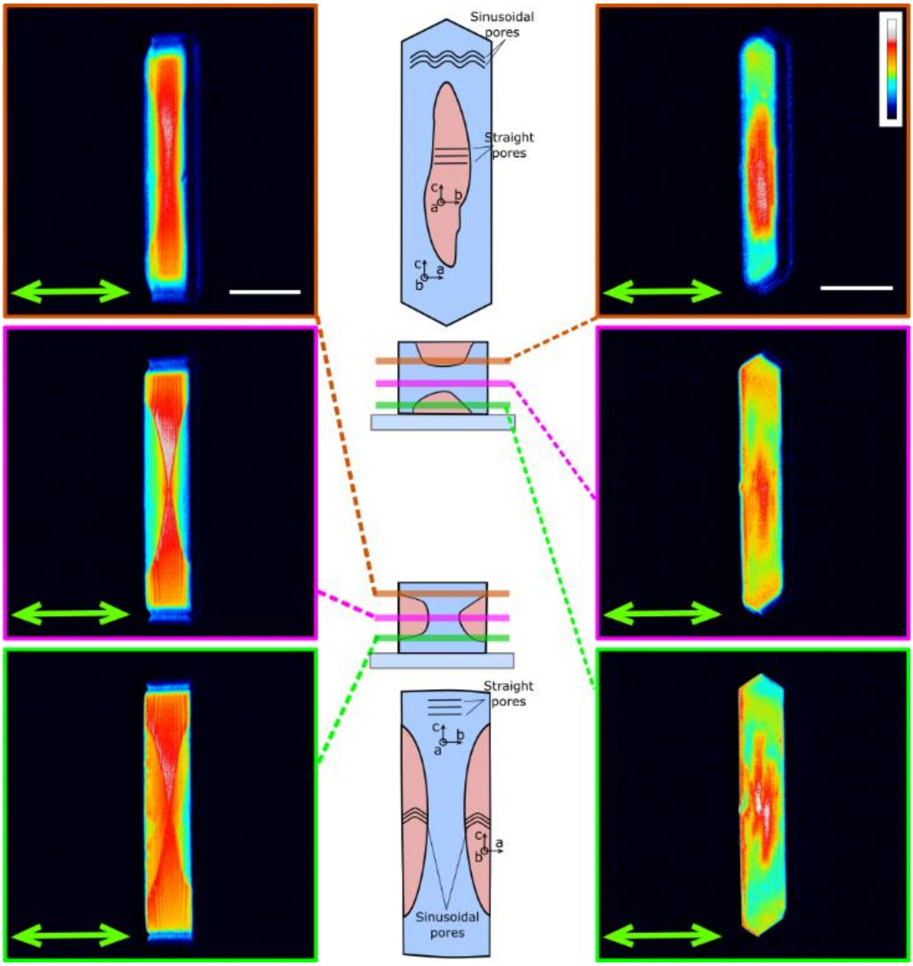

Figure 4.S11. SRS micrographs of benzonitrile adsorbed at different depth within H-ZSM-5-800 crystal lying on the [100] facet (left) or [010] facet (right). False color scale shows the observed SRS intensity for CN vibration adjusted for each slide; green arrow indicates the excitation light polarization orientation; scale bar: 20 μm.

4.6.4 References

[1] N. M. Sergeyev, N. D. Sergeyeva, *Phys. Chem. Chem. Phys.* **2002**, *4*, 2994-2999.

[2] M. Houlleberghs, A. Hoffmann, D. Dom, C. E. A. Kirschhock, F. Taulelle, J. A. Martens, E. Breynaert, *Anal. Chem.* **2017**, under review.

[3] K. Nishi, A. Hidaka, Y. Yokomori, *Acta Crystallogr., Sect. B: Struct. Sci.* **2005**, *61*, 160–163.

CHAPTER 5

Surface acid–base catalytic activity of ZIF-8 revealed by super-resolution fluorescence microscopy

Alexey V. Kubarev and Maarten B. J. Roeffaers

Adapted from: *CrystEngComm*, **2017**, DOI: 10.1039/C7CE00074J

by permission of The Royal Society of Chemistry

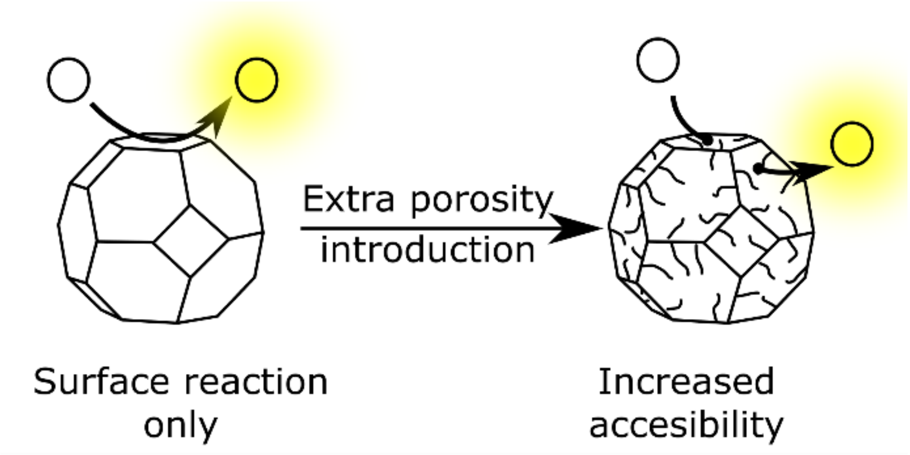

Abstract

We investigated the catalytic activity of ZIF-8 in FDA hydrolysis via super-resolution fluorescence microscopy. Acid–base activity is detected only on the outer surface and crystal defects. Oleic acid etching introduces extra porosity and allows catalytic conversion inside the crystals, but leads to overall activity loss.

Contributions

The main part of the experimental work and article writing was performed by Alexey Kubarev. Maarten Roeffaers and Alexey Kubarev conceived the project and were involved in data interpretation and article writing.

CHAPTER 5 – SURFACE ACID–BASE CATALYTIC ACTIVITY OF ZIF-8 REVEALED BY SUPER-RESOLUTION FLUORESCENCE MICROSCOPY

5.1 INTRODUCTION

In recent years, metal–organic frameworks (MOFs) have been studied extensively as heterogeneous catalysts.[1–3] One of the main advantages of MOFs over more traditional inorganic porous materials is the chemical variability offered by hybrid frameworks. Numerous MOFs have been described by varying the metal cation as well as the organic linkers. As both can be varied independently, this offers unique opportunities for the development of bi-functional catalysts. One industrial process which could benefit from improved bifunctional acid–base catalysts is the synthesis of biodiesel. In this process, fatty acid methyl esters are obtained from the transesterification of triglycerides. Traditionally, (mixed) metal oxides and hydroxides have been extensively investigated for this purpose. The complex nature of surface sites and the limited amount of control over them have triggered researchers to investigate alternative materials. Several MOFs for example have been shown to be active in transesterification reactions.[4,5] In particular, one exceptionally stable[6] MOF type, zeolite imidazolate framework ZIF-8, is active in (trans)esterification reactions,[7,8] as well as in a range of other acid–base-catalyzed reactions.[9–12] However, it is not straightforward to identify the catalytically active sites from the crystal structure of ZIF-8. Theoretically, the structure of ZIF-8 does not possess low-coordinated zinc atoms that could act as Lewis acids, and neither do its imidazolate linkers bear an accessible nitrogen atom that could act as a base. Therefore, the intrinsic catalytic activity of non-functionalized ZIF-8 posed a challenge to the type and location of its active sites. Several investigations of ZIF-8 catalytic properties have been conducted. In particular, Chizallet et al. showed that ZIF-8 can dissociate alcohols, which is necessary for transesterification, and suggested that coordinatively undersaturated Zn(II) species as acid sites are located, with N-moieties and OH groups as basic sites, at the external surface of ZIF-8 or at crystal defects.[7] However, all prior investigations have been done on the macro scale using bulk characterization techniques such as catalytic testing and infrared spectroscopy. For example, the conclusions about the active site location are made based on indirect observations, such as shifts in the frequency of carbon monoxide adsorbed on ZIF-8. The observed CO-vibrational frequencies were attributed to CO adsorbed on sites at the outer surface of the crystal based on supporting density functional theory calculation. These techniques do not have spatial resolution to directly probe the location of catalytic reactions or to pinpoint the active sites in individual catalyst crystals. In our view, the appropriate approach to locate the active sites lies in the use of microscopy techniques. In particular, fluorescence microscopy has been shown to be a suitable tool for investigating the single-crystal catalytic activity of a wide variety of heterogeneous catalysts, such as zeolites,[13–18] fluid catalytic cracking catalysts,[19] layered double hydroxides,[20] metal nanoparticles[21,22] and MOFs.[23] In this approach, the catalytically active zones are selectively stained by the formation of fluorescent reaction products. Nanoscale reactivity maps, with resolutions below the optical diffraction-limited resolution of a few hundreds of nanometers, are based on the localization of individual catalytic conversions of fluorogenic – non fluorescent – reactants into strongly fluorescent products. This single molecule localization-based variant of fluorescence microscopy specifically designed for catalysis research is called NASCA microscopy.[24] NASCA microscopy allows the detection of individual catalytic turnovers with a lateral resolution of tens of nm. Therefore, in this work, NASCA microscopy was selected as the technique of choice for the precise localization of the catalytic activity displayed by individual ZIF-8 crystals.

For our investigation, we synthesized ZIF-8 materials according to the procedure described by Bux et al.[25] This method allowed us to obtain a powdered sample that largely consists of well-defined crystals of truncated rhombic dodecahedral morphology with a wide size distribution – approximate crystal dimensions range from 5 to 25 μm. Crystals with these dimensions are perfectly suited for NASCA microscopy, which would also work with smaller crystals; the limited axial resolution of about 500 nm, related to the optical section that is sharply in focus,[26] simplifies the interpretation. The use of larger crystals has an additional practical advantage as optical transmission microscopy, which is diffraction-limited in resolution, was used to select and identify the crystals under study in the catalytic experiment.

As the use of fluorescence microscopy and by extension NASCA microscopy requires strongly fluorescent reaction products to pinpoint the location of catalytic activity, it is not possible to directly observe the transesterification of triglycerides. Instead, we used in this work fluorescein diacetate (FDA) hydrolysis as an appropriate model reaction (**Figure 5.1**); the catalytic hydrolysis leads to the formation of individual fluorescein molecules (**Figure 5.2B**, inset). Such single catalytic events can be captured by an EM-CCD camera, using the correct color filters, and these catalytic events are consecutively localized with nanometer precision to uncover the distribution of catalytic conversions throughout the ZIF-8 crystal.[17,20,24] This reaction is not only mechanistically similar to transesterification of triglycerides, the molecular size of FDA (minimal projection diameter = 12.08 Å) is also comparable to the size of triglycerides (minimal projection diameter for oleic acid triglyceride = 17.60 Å), and similar to triglycerides, FDA molecule is larger than aperture size of ZIF-8 (3.4 Å).[6]

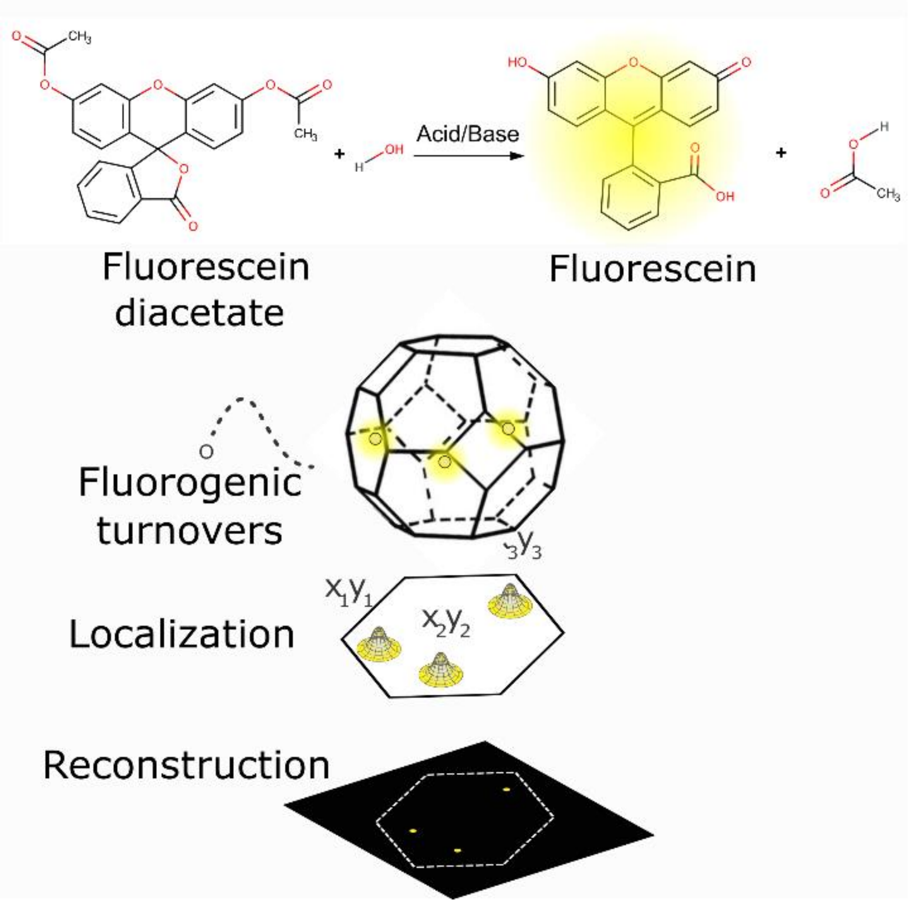

Figure 5.1. Schematic representation of the NASCA microscopy approach.

Figure 5.2 shows an example of the NASCA approach using FDA as a probe molecule revealing the location of catalytic activity on an individual ZIF-8 crystal. The optical transmission image (**Figure 5.2A**) gives a clear view of the truncated rhombic dodecahedron-shaped ZIF-8 crystal with an evident defect at the right side of the crystal. As the transmission image is the result of absorption and scattering events along the optical path length, it does not provide precise information on the structural features and it for sure does not yield insight into the location of the catalytically active centers. After FDA addition, the locations of catalytic activity light up in the WFM microscope (**Figure 5.2B**) as individual bright emitters (**Figure 5.2B**, inset).

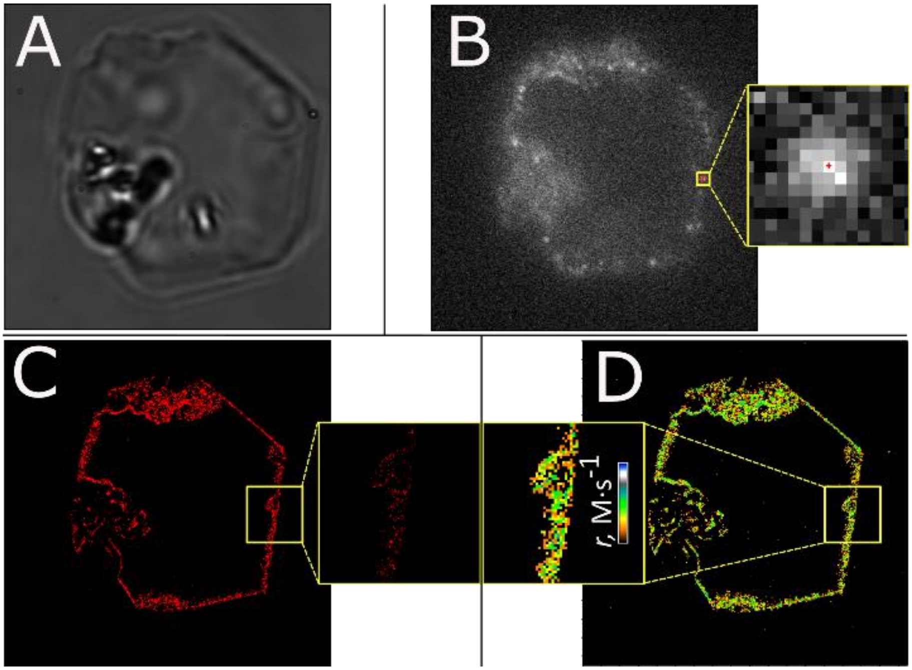

Figure 5.2. Procedure for NASCA microscopy approach as exemplified by ZIF-8 catalysis of FDA hydrolysis. A – bright-field transmission image, B – single frame of WFM-acquired movie, B inset – example of a localized single emitter, C – scatter plot of all localized position for the acquired movie, C inset – magnification of the area of interest, D – NASCA reactivity map of the catalytic activity reconstructed for 50 × 50 × 800 nm^3 voxels (xyz) for the duration of ≈ 150 s, D inset – magnification of the area of interest, false color shows the observed reaction rate in logarithmic scale from 2.2×10^{-9} to 6×10^{-7} $M{\cdot}s^{-1}$.

The entire NASCA experiment consists of recording 1000–10000 consecutive frames of 50 ms integration time each. The FDA molecules are stochastically converted at the catalytically active sites resulting in bright fluorescein molecules that only appear briefly (~100 ms on average or 2 consecutive frames) as the product is photo-bleached or diffuses away. The positions of each catalytic turnover, localized in each frame and corrected for reappearing molecules, were plotted as a scatter plot (**Figure 5.2C**) or as an accumulated reactivity map in which all conversions inside 50 × 50 × 800 nm^3 voxels are counted (**Figure 5.2D**). In contrast to optical transmission imaging, only single fluorescent products formed in a thin optical slice are recorded and localized effectively. Optical slicing allows the reactivity of individual particles to be mapped in 3D.

5.2 RESULTS AND DISCUSSION

The catalytic activity distribution of a single ZIF-8 crystal is presented in **Figure 5.3** as a set of optical slices along the depth of the crystal.

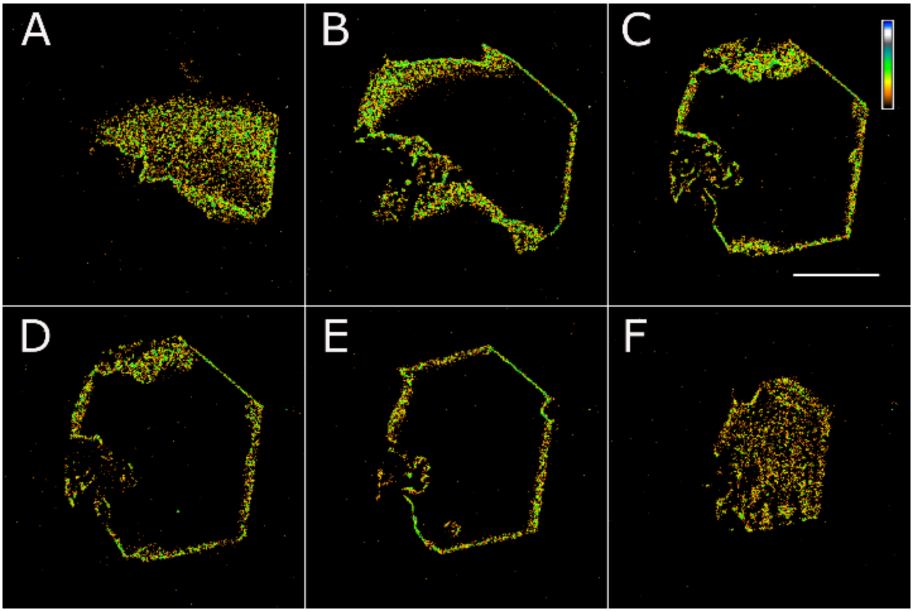

Figure 5.3. NASCA reactivity maps of FDA hydrolysis catalyzed inside of a ZIF-8 crystal. A – bottom surface of the crystal, B-E – gradually progressive slices in the bulk of the crystal, F – top surface of the crystal. Scale bar is 5 μm; maps are reconstructed for 50 × 50 × 800 nm^3 voxels (xyz) for the duration of ≈ 150 s; false color shows the observed reaction rate in logarithmic scale from 2.2×10^{-9} to 6×10^{-7} $M \cdot s^{-1}$.

These NASCA images obtained for the different optical slices spaced ~2 μm apart were recorded from the bottom to the top of the crystal and are presented with an identical color scale. Clearly, the catalytic activity is restricted to the outer surface of the crystal. This observed surface-limited activity is in agreement with the suggestion of Chizallet et al.[7,27] Even more so, several other studies have indicated that the active sites of many MOFs are most likely linked to the defects in the crystalline structure.[28,29] Correspondingly, in some optical slices, the activity at crystal defects is captured showing catalytic conversions also at the internal parts of the ZIF-8 crystal (**Figure 5.3B–E**). Some facets of the crystal are almost free of defects at every depth, while others are rich in defects. Such an uneven defect distribution occurs stochastically only in some ZIF-8 crystals, as additional observations showed (**Figure 5.S1**).

Therefore, we hypothesized that the catalytic activity of ZIF-8 can be improved via introduction of extra-framework pores which increases the effective surface area. Wee et al. described spontaneous formation of mesopores in ZIF-8 during direct glycerol esterification with oleic acid.[8] They proposed that oleic acid treatment alone can be a viable procedure for mesopore introduction. We applied the suggested oleic acid treatment to ZIF-8, which resulted in crystal etching (**Figure 5.4A, B**).

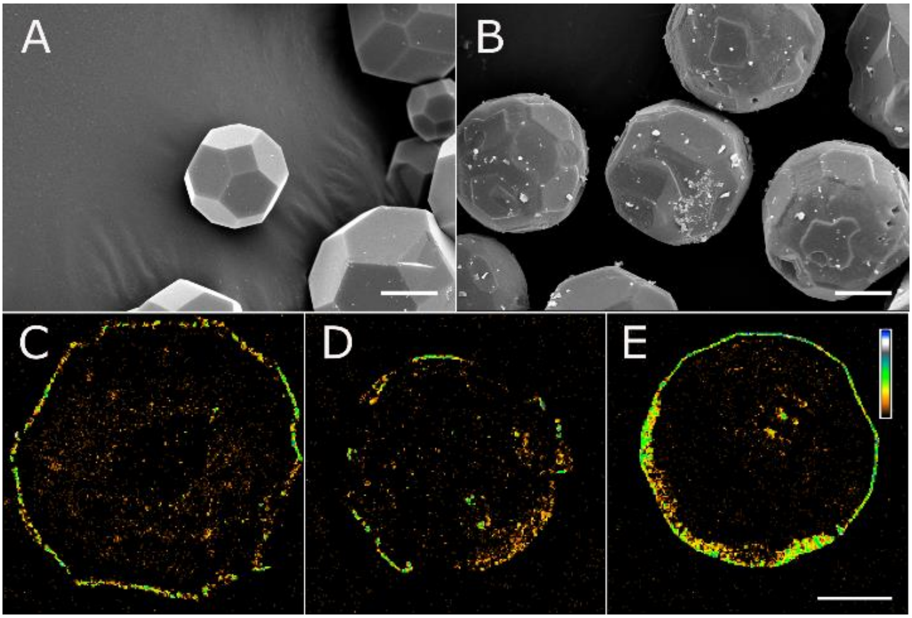

Figure 5.4. Effect of oleic acid etching on structure and activity of ZIF-8 crystals. A-B – SEM micrographs of original (A) and etched(B) ZIF-8 crystals, scale bars are 10 μm; C-E – NASCA reactivity maps of FDA hydrolysis catalyzed inside of three exemplary etched ZIF-8 crystals. Scale bar is 5 μm, maps are reconstructed for 100 × 100 × 800 nm^3 voxels (xyz) for the duration of ≈ 500 s; false color shows the observed reaction rate in logarithmic scale from 2.9×10^{-10} to 2.6×10^{-7} $M{\cdot}s^{-1}$.

It is clear that the catalytic activity of etched ZIF-8 is not exclusively restricted to the outer surface (**Figure 5.4C–E**), in line with our expectations. While the majority of reaction events still take place at the outer surface, some FDA molecules are able to reach the inner regions of the crystals; prolonged etching in the oleic acid solution led to complete fragmentation of the ZIF-8 crystals. Surprisingly, the overall catalytic activity of ZIF-8 seems to have decreased as a result of oleic acid etching as can be seen in the smaller reaction rate values detected in the etched ZIF-8 crystals. The oleic acid treatment however leads to a significant rise in background fluorescence, complicating a precise quantitative comparison between catalytic activities based on the NASCA experiment.

The observations from the NASCA experiment were cross-checked and validated by determining the catalytic behavior on the bulk scale with 0.5 mg of ZIF-8 powder and using a FDA concentration of 5 μM in 3 ml of water. Due to the fluorogenic nature of this reaction, the bulk catalytic activity can be easily monitored using a standard spectrophotometer or fluorimeter. In this experiment, the fluorescein product concentration was measured using the optical absorption at 491 nm wavelength after 24 hours. The bulk-scale catalytic activity of the etched ZIF-8 based on the measured fluorescein concentration was estimated to be about 80% of the activity of the original catalyst sample. It is important to note that in the study of Wee et al.,[8] the etched sample's activity could not be compared with that of the original sample due to oleic acid etching being the inherent side reaction. To the best of our knowledge, no other investigation studied the effect of oleic acid on the structure and activity of ZIF-8. Our results for the first time show that in addition to the increase in surface area, oleic acid etching reduces the number or accessibility of active sites. Such a reduction in activity is probably related to the poisoning of the base active sites by oleic acid preventing FDA molecules from being activated.

Our attempts to remove oleic acid from the sample by washing it with 1-heptanol, heptane, methanol solution of 2-methylimidazol, and methanol did not improve the catalytic performance (**Figure 5.S2**). We conclude that the poisoning by oleic acid is rather strong and that its removal is not trivial.

5.3 CONCLUSIONS

In conclusion, we investigated the catalytic activity of ZIF-8 in FDA hydrolysis reaction as a reference for its activity as a solid catalyst e.g. in triglyceride transesterification. The sites of the activity of microporous ZIF-8 are limited to the outer crystal surface and surface of the bulk defects, providing direct proof to the earlier proposed hypothesis. Introducing additional extra-framework porosity by oleic acid etching allows catalysis to occur deeper inside the crystal, however at a lower reaction rate due to the poisoning of the active sites. Further research on the optimized catalytic performance of the modified ZIF-8 catalyst in transesterification reactions should focus on finding a procedure to effectively remove the porosity-inducing agent (oleic acid) or alternative porosity-inducing agents that can be removed more easily.

5.4 EXPERIMENTAL SECTION

5.4.1 Materials and Synthetic Procedures

Synthesis of ZIF-8 was based on the procedure described by Bux et al.[25] A solid mixture of 0.539 g zinc chloride (>98.5%, Acros Organics), 0.486 g 2-methylimidazole (>97%, TCI) and 0.270 sodium formate (>99.5%, Merck) was dissolved in 40 ml methanol (>99.8%, Honeywell) by ultra sonic treatment. Afterwards the solution was placed into a 100 ml Teflon autoclave and heated in a microwave oven (Microsynth, Milestone) with a rate of 8°C min^{-1} to 100°C and stayed at that temperature for 4 h. After cooling, the precipitated crystals were filtered and washed with methanol and dried for 1 day over silica gel at room temperature.

ZIF-8 modification was based on the procedure described by Wee et al.[8] 0.075 g of oleic acid (>97%, Acros organics), 2.5 g of tert-butanol (>99%, Sigma-Aldrich) and 0.033 g of ZIF-8 catalyst were added to a 20 ml stainless steel reactor and heated in oil bath with a rate of 8°C min^{-1} to 150°C and stayed at that temperature for 20 h. After cooling, modified ZIF-8 crystals were separated by centrifugation and washed with methanol and dried for 1 day over silica gel at room temperature.

To remove traces of oleic acid, modified ZIF-8 sample was washed with excess of 1-heptanol (>98%, Sigma-Aldrich), heptane(>99%, Acros organics), methanol solution of 2-methylimidazol, and methanol. Then, modified ZIF-8 crystals were separated by centrifugation and dried for 1 day over silica gel at room temperature. After that, the sample was tested for catalytic activity (**Figure 5.S2**). Further, the sample was evacuated at 250°C and under 0.08 mBar vacuum, what caused sample to become brightly orange-colored and unsuitable for further fluorescence microscopy investigation due to overwhelming background fluorescence.

FDA (>99%, Sigma-Aldrich) was additionally purified by the means of preparative High-Performance Liquid Chromatography (HPLC). HPLC was conducted on Waters 996 with Waters 600-controller and polar column Alltech Prevail C18 (5 µm particle size, 15 cm length and 22 mm diameter). The separation started with 50:50 mixture of water and acetonitrile and then was gradually switched to pure acetonitrile.

MilliQ water for hydrolysis reaction was obtained from water purification system Synergy UV (Merck Millipore).

5.4.2 Fluorescence Microscopy

For the microscopy experiments, crystals were spin-casted on a clean cover glass (thickness #1). Liquid phase experiments were performed in 1 ml of water solution with a concentration of FDA of 5×10^{-8} M added to polytetrafluoroethylene container sealed to the glass cover slip via a silicone rubber gasket.

The NASCA investigation was conducted on a WFM setup based on an inverted epi-fluorescence inverted microscope IX71 (Olympus) platform equipped with an oil immersion objective lens (100×, 1.4 NA, Olympus) and a Diode-Pumped Solid State Excelsior laser (Spectra-Physics). The latter provided a laser excitation with $\lambda = 491$ nm of 25 W/cm^2 power on the sample. Fluorescence imaging (505 nm long pass filter) was performed using an ImagEM Enhanced C9100-23B EM-CCD camera (Hamamatsu). Further single molecule identification, localization and generation of NASCA images were performed using an in-house developed set of open-source plugin routines (https://bitbucket.org/pdedecker/localizer)[30] for IgorPro v.6.34A software (Wavemetrics). The presented NASCA images were obtained by the accumulation of localized fluorescent emitters which appeared during reaction in the focal plane in the middle of the crystals for a recording duration indicated in the figure captions.

5.4.3 Spectrophotometric Detection

Bulk scale catalytic reaction was conducted in quartz cuvettes. 3 ml of water solution with a concentration of FDA of 5×10^{-6} M was added to 0.5 mg of ZIF-8 catalyst and stirred at 25°C for 96 h. Fluorescein concentration was detected by the means of spectrophotometer Lambda 950 UV/Vis/NIR (PerkinElmer) using the optical adsorption at 491 nm wavelength.

5.4.4 Molecular Geometry Calculations

Geometrical descriptors for FDA and oleic acid triglyceride were calculated using MarvinSketch.[31]

5.5 REFERENCES

[1] A. Dhakshinamoorthy, M. Opanasenko, J. Čejka, H. Garcia, *Catal. Sci. Technol.* **2013**, *3*, 2509–2540.

[2] J. Lee, O. K. Farha, J. Roberts, K. A. Scheidt, S. T. Nguyen, J. T. Hupp, *Chem. Soc. Rev.* **2009**, *38*, 1450–1459.

[3] P. García-García, M. Müller, A. Corma, *Chem. Sci.* **2014**, *5*, 2979–3007.

[4] M. Savonnet, S. Aguado, U. Ravon, D. Bazer-Bachi, V. Lecocq, N. Bats, C. Pinel, D. Farrusseng, *Green Chem.* **2009**, *11*, 1729–1732.

[5] J. Juan-Alcañiz, E. V Ramos-Fernandez, U. Lafont, J. Gascon, F. Kapteijn, *J. Catal.* **2010**, *269*, 229–241.

[6] K. S. Park, Z. Ni, A. P. Côté, J. Y. Choi, R. Huang, F. J. Uribe-Romo, H. K. Chae, M. O'Keeffe, O. M. Yaghi, *Proc. Natl. Acad. Sci. U. S. A.* **2006**, *103*, 10186–10191.

[7] C. Chizallet, S. Lazare, D. Bazer-Bachi, F. Bonnier, V. Lecocq, E. Soyer, A. A. Quoineaud, N. Bats, *J. Am. Chem. Soc.* **2010**, *132*, 12365–12377.

[8] L. H. Wee, T. Lescouet, J. Ethiraj, F. Bonino, R. Vidruk, E. Garrier, D. Packet, S. Bordiga, D. Farrusseng, M. Herskowitz, et al., *ChemCatChem* **2013**, *5*, 3562–3566.

[9] B. Murillo, B. Zornoza, O. de la Iglesia, C. Téllez, J. Coronas, *J. Catal.* **2016**, *334*, 60–67.

[10] X. Zhou, H. P. Zhang, G. Y. Wang, Z. G. Yao, Y. R. Tang, S. S. Zheng, *J. Mol. Catal. A Chem.* **2013**, *366*, 43–47.

[11] L. T. L. Nguyen, K. K. A. Le, N. T. S. Phan, *Chinese J. Catal.* **2012**, *33*, 688–696.

[12] U. P. N. Tran, K. K. A. Le, N. T. S. Phan, *ACS Catal.* **2011**, *1*, 120–127.

[13] K.-L Liu, A. V. Kubarev, J. Van Loon, H. Uji-I, D. E. De Vos, J. Hofkens, M. B. J. Roeffaers, *ACS Nano* **2014**, *8*, 12650–12659.

[14] A. V. Kubarev, K. P. F. Janssen, M. B. J. Roeffaers, *ChemCatChem* **2015**, *7*, 3646–3650.

[15] Z. Ristanović, J. P. Hofmann, G. De Cremer, A. V. Kubarev, M. Rohnke, F. Meirer, J. Hofkens, M. B. J. Roeffaers, B. M. Weckhuysen, *J. Am. Chem. Soc.* **2015**, *137*, 6559–6568.

[16] Z. Ristanović, A. V. Kubarev, J. Hofkens, M. B. J. Roeffaers, B. M. Weckhuysen, *J. Am. Chem. Soc.* **2016**, *138*, 13586–13596..

[17] M. B. J. Roeffaers, G. De Cremer, H. Uji-i, B. Muls, B. F. Sels, P. A. Jacobs, F. C. De Schryver, D. E. De Vos, J. Hofkens, *Proc. Natl. Acad. Sci. U.S.A.* **2007**, *104*, 12603–12609.

[18] E. Stavitski, M. H. F. Kox, B. M. Weckhuysen, *Chem. - A Eur. J.* **2007**, *13*, 7057–7065.

[19] Z. Ristanović, M. M. Kerssens, A. V. Kubarev, F. C. Hendriks, P. Dedecker, J. Hofkens, M. B. J. Roeffaers, B. M. Weckhuysen, *Angew. Chem. Int. Ed.* **2015**, *54*, 1836–1840.

[20] M. B. J. Roeffaers, B. F. Sels, H. Uji-I, F. C. De Schryver, P. A. Jacobs, D. E. De Vos, J. Hofkens, *Nature* **2006**, *439*, 572–575.

[21] X. Zhou, N. M. Andoy, G. Liu, E. Choudhary, K.-S. Han, H. Shen, P. Chen, *Nat. Nanotechnol.* **2012**, *7*, 237–41.

[22] X. Zhou, W. Xu, G. Liu, D. Panda, P. Chen, *J. Am. Chem. Soc.* **2010**, *132*, 138–146.

[23] P. Valvekens, D. Jonckheere, T. De Baerdemaeker, A. V. Kubarev, M. Vandichel, K. Hemelsoet, M. Waroquier, V. Van Speybroeck, E. Smolders, D. Depla, et al., *Chem. Sci.* **2014**, *5*, 4517–4524.

[24] M. B. J. Roeffaers, G. De Cremer, J. Libeert, R. Ameloot, P. Dedecker, A. J. Bons, M. Bückins, J. A. Martens, B. F. Sels, D. E. De Vos, et al., *Angew. Chem. Int. Ed.* **2009**, *48*, 9285–9289.

[25] H. Bux, F. Liang, Y. Li, J. Cravillon, M. Wiebcke, J. J. Caro, *J. Am. Chem. Soc.* **2009**, *131*, 16000–16001.

[26] D. B. Murphy, M. W. Davidson, *Fundamentals of Light Microscopy and Electronic Imaging*, John Wiley & Sons, Inc., Hoboken, NJ, USA, **2012**.

[27] C. Chizallet, N. Bats, *J. Phys. Chem. Lett.* **2010**, *1*, 349–353.

[28] J. Canivet, M. Vandichel, D. Farrusseng, *Dalt. Trans.* **2016**, *45*, 4090–4099.

[29] P. Valvekens, F. Vermoortele, D. De Vos, *Catal. Sci. Technol.* **2013**, *3*, 1435–1445.

[30] P. Dedecker, S. Duwé, R. K. Neely, J. Zhang, *J. Biomed. Opt.* **2012**, *17*, 126008.

[31] MarvinSketch with Calculator Plugins (version 15.9.21.0), calculation module developed by ChemAxon, http://www.chemaxon.com/products/marvin/marvinsketch/, **2015.**

SUPPORTING INFORMATION TO CHAPTER 5

5.6 SUPPORTING INFORMATION

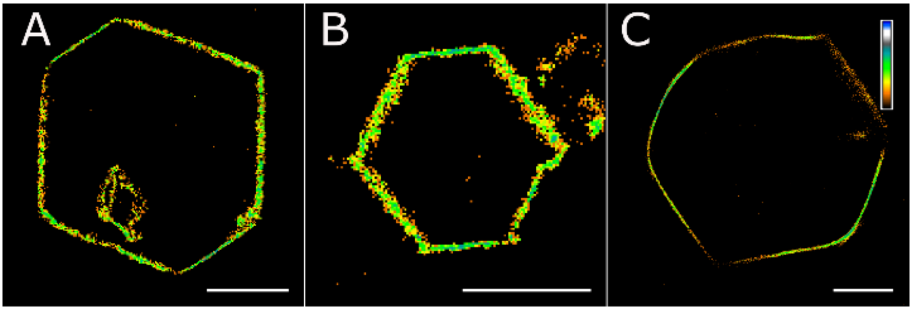

Figure 5.S1. NASCA reactivity maps of FDA hydrolysis catalyzed inside of several ZIF-8 crystals. Scale bars are 3 μm; maps are reconstructed for 50 × 50 × 800 nm^3 voxels (xyz) for the duration of ≈ 150 s; false color shows the observed reaction rate in logarithmic scale from 2.2×10^{-9} to 7.4×10^{-7} M·s^{-1}.

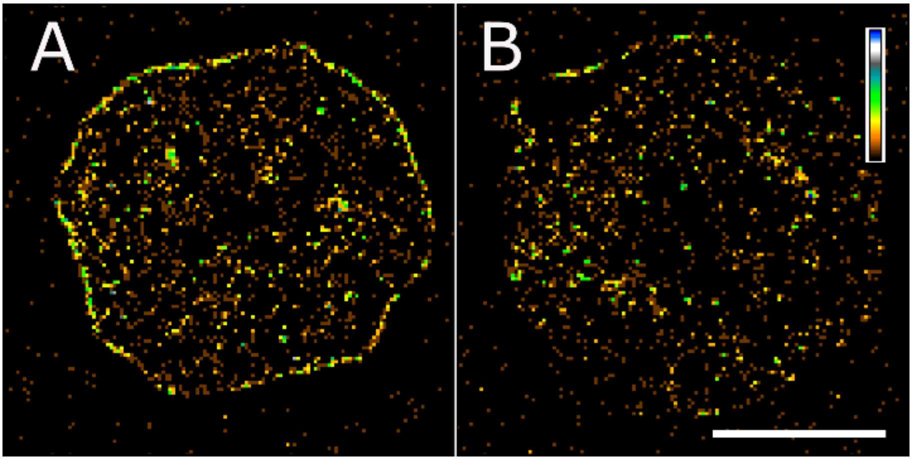

Figure 5.S2. Effect of oleic acid removal attempt on activity of ZIF-8 crystals. NASCA reactivity maps of FDA hydrolysis catalyzed inside of two exemplary etched ZIF-8 crystals. Scale bar is 5 μm, maps are reconstructed for 100 × 100 × 800 nm^3 voxels (xyz) for the duration of ≈ 500 s; false color shows the observed reaction rate in logarithmic scale from 2.9×10^{-10} to 3.0×10^{-8} M·s^{-1}.

CHAPTER 6

Conclusions and Perspectives

CHAPTER 6 – CONCLUSIONS AND PERSPECTIVES

In-depth catalyst characterization is an important aspect of modern catalysis research. As concluded in **Chapter 1**, fluorescence microscopy is a recent addition to the toolbox of the catalysis researcher. This technique in combination with the appropriate probe reaction and assay allows for example to compare catalytic properties between individual catalyst particles and see variations even within individual catalysts. These length scales were typically overlooked by traditional characterization techniques. However, the use of fluorescence techniques is still relatively rare in academic catalysis research and even more so in industrial research and development.

The main goal of this PhD thesis was to further exploit the advantages offered by fluorescence microscopy techniques to investigate the interplay between local catalytic performance and catalyst porosity. In particular, structure-activity and selectivity relationships were derived for several heterogeneous catalysts at the smallest possible length scales and with the highest possible sensitivities down to individual catalytic turnovers taking place at the individual catalyst particles. To achieve this goal I employed both diffraction-limited and super-resolution fluorescence microscopy with support from electron microscopy and advanced Raman microspectroscopy.

In **Chapter 2** of this thesis I used NASCA microscopy to investigate the effect which post-synthetic extra-framework porosity introduction through dealumination has on catalytic performance of acid mordenite zeolites. With NASCA measurements, the "small-port behavior" was for the first time visually evidenced in non-dealuminated mordenites, and it was shown that severe dealumination induces efficient pore opening. On the other hand, mild dealumination induces a large variability in catalytic behavior between individual crystals present in a powdered batch. Visually, the crystals could be subdivided into three subgroups and using the quantitative capabilities of NASCA microscopy I could determine the relative contribution of these three groups to the overall performance. Besides significant interparticle variability the nanoscale resolution of NASCA microscopy also uncovered differences in catalytic activity of subcrystal regions. The precise nature of this inter- and intracrystal activity differences could be rationalized by variations in inter- and intracrystal acid site distribution and accessibility, studied with SRS microscopy. We discovered that there are no gradients in acid site density in parent non-dealuminated mordenite sample proving that the differences in catalytic activity are due to the dealumination. Furthermore, from the results of SRS microscopy it is evident that the uneven distribution of acid sites in mildly dealuminated mordenites is due to the diffusion-limiting step in the dealumination mechanism. In follow-up study, presented in **Chapter 3**, I elaborated on the way how the extra-framework pores are introduced during mild dealumination into mordenite sample. In mildly dealuminated mordenite crystals I discovered large extra-framework macropores, ordered in a fan-like fashion. These extra-framework pores severely enhance the local catalytic activity, which follows a similar fan-shaped pattern. Using the polarized light experiments, I could prove that the locally enhanced catalytic activity is not the result of defects at the walls of the extra-framework pores but rather is due to enhanced molecular transport to the mordenite micropores adjacent to the extra-framework macropores. Overall, I discovered suboptimal catalytic behavior in commercial, industrially-relevant dealuminated mordenites and revealed the origin of it. My results allowed to propose the dealumination mechanism at single-crystal level. I hypothesize that discovered heterogeneities in catalytic activity, acid sites distribution, and extra-framework porosity are caused by gradients in local temperature, steam pressure, and acid concentration, which are common in industrial-scale reactors.[1] Step-by-step dealumination mechanism is broadly accepted,[2] and recent density functional theory calculations indicated that the rate-limiting step is the Al–O hydrolysis upon the water adsorption.[3] The diffusion-limited character of mordenite dealumination process, discussed in **Chapter 2**, is likely related to the hindered mass transport of water during mordenite steaming and supports the step-by-step mechanism hypothesis. I propose that catalytic activity of mordenites can be improved if dealumination is performed in more controlled way, possibly with more gradual increase of temperature and steam pressure to counteract hindered mass transport of water molecules. The development of such optimized dealumination process should rely on detailed insights obtained from (single-molecule) fluorescence microscopy characterization.

Chapter 4 shows the solvent-induced pore preference effect for catalytic activity in H-ZSM-5 zeolite. I show that the acid-catalyzed reaction preferentially occurs in the straight pores of H-ZSM-5 crystals if water is used as solvent, and in the perpendicular sinusoidal pores if 1,4-dioxane or 2-butanone are used as solvents. The results show that this pore preference is governed by the interplay between solvent polarity, reagent polarity and pore polarity. For the studied H-ZSM-5 crystals, it is hypothesized that pore polarity differs between straight and sinusoidal pores due to the preferential location of hydrophilic silanol defects in straight pores. However, additional investigations are required to confirm the origin of the pore-preference effect. Further linking of this process to synthesis parameters would ultimately yield a toolbox to control the presence, direction and extent of the pore preference. These findings will contribute significantly to the process of rational design of selective ZSM-5 based catalysts. For example, these results will pave the way to use this pore preference effect to perform selective pore modification of ZSM-5, and either selectively functionalize or block active sites in only one micropore subsystem. In that way, the reactions performed on these new catalysts could benefit from enhanced, finely tuned shape selectivity.

Finally, in **Chapter 5** the range of microporous materials studied by fluorescence microscopy was expanded from zeolites to MOFs. Here, I studied the location of the catalytic ester hydrolysis by ZIF-8 at the single crystal level by NASCA microscopy. In accordance with the hypothesis in the field,[4] I could directly prove that the catalytic activity of ZIF-8 is limited to the outer surface and bulk crystal defects, leading to inefficient use of catalytic material. To enhance the molecular transport, extra-framework porosity was introduced via an oleic acid based etching procedure. This method successfully increased the penetration of reactants into the ZIF-8 crystals, but unfortunately the overall activity decreased due to strong sorption of the etching molecules at the active sites. The results of this ZIF-8 study shed light on challenges in rational design of heterogeneous catalysts. Similar to the effect of dealumination on zeolites, introducing extra-framework porosity to MOFs material may decrease catalytic activity. While for zeolites removal of post-synthetic treatment agents through calcination is straightforward, for MOFs such removal is typically more complex due to lower thermal stability. Therefore, the development of appropriate post-synthetic treatment has to be done with caution as removal of the etching chemicals is more complex as typical removal via heating and calcination is not straightforwardly possible. Further research is needed on the procedures to effectively control extra-framework pores introduction in the MOFs without decreasing number of available active sites.

To sum up, in this thesis I successfully employed fluorescence microscopy to address unsolved issues in catalysis research in the light of porosity-activity relationship. I showed how fluorescence microscopy is used to resolve details about the catalytic process (inter- and intracrystal heterogeneity) that are typically masked in ensemble-averaged bulk characterization techniques. Based on the novel insights generated for both commercial and laboratory-produced catalysts I suggested procedures to improve these catalysts. My work also shows the great promise that single-crystal investigations hold for catalysis research in general. The fluorescence microscopy techniques can potentially be streamlined and used in industrial research context to routinely scan representative sub-ensembles of catalysts batches to reveal the inter- or intracrystal heterogeneities and modify the catalyst preparation procedures to avoid inefficient catalyst material usage.

I anticipate that further technical developments of the fluorescence microscopy in combination with an expansion of the range of catalytic systems that can be investigated will make this approach widely accepted and used in the field of heterogeneous catalysis.

From the technical side, I believe that an obvious step forward would involve the full implementation of 3D super-resolution fluorescence microscopy techniques. While the attempts to do so in my PhD research were not yet successful (Appendix 1), I believe that the improvement in axial resolution is required to enable detailed investigations of nanocrystalline catalysts, such as nanolayered zeolites, nanosized MOFs, or zeolite domains inside fluid catalytic cracking particles. While variations in RI currently seem to stand in the way of the practical implementation, I see potential solutions in the use of adaptive optics,[5] or the localization correction based on light ray propagation modelling (coupled with catalyst particle morphology determined by correlative structural investigation – see below). A second improvement for catalysis research would be the application of light-sheet fluorescence microscopy to study micron to micrometer-sized catalyst crystals, particles and even shaped catalysts. With this approach improved SBRs can be obtained in the comparison to WFM and improved imaging speeds in the comparison with CLSM. Additionally, if implemented correctly, in light-sheet fluorescence microscopy scattering and absorption of light currently hampering the study of larger objects can be partially overcome. Similar as in 3D super-resolution fluorescence microscopy, while implementing light sheet fluorescence microscopy, care has to be taken to compensate or correct for the expected variations in RI. A third step forward I see is the combination of a detailed structural investigation by for example electron microscopy and activity investigation by fluorescence microscopy to determine structure-activity relationships at the smallest scales. As large interparticle heterogeneities have been identified repeatedly over the last years, detailed structural characterization needs to be performed at the same crystal as the activity measurements. Therefore, the research leading into development and application of these integrated techniques will be a significant breakthrough. Finally, fluorescence microscopy detection could supplement and enhance the use microfluidic reactors in the catalysis research, which allow to downsize chemical processes for lab-scale modelling or analysis.[6]

Additionally, there is a possibility to support the results of super-resolution investigation from the point of view of chemical kinetics. It is possible to conduct kinetic studies on the single-molecule level and correlate the kinetic parameters with the results obtained on bulk level; such studies would allow to further increase the relevance of the results obtained at single-molecule level and facilitate the acceptance of the super-resolution fluorescence microscopy in the industrial research characterization toolbox.

Fluorescence microscopy research has been proven possible for all big groups of heterogeneous catalysts: acid-based, redox, photocatalysis and electrocatalysis. However, a further expansion of the fluorogenic reaction toolbox will enable the study of new catalysts and answer specific questions that cannot be answered with the current (limited) fluorogenic reactions scope. Apart from simply covering the different reaction types (Brønsted/Lewis acid-base and red-ox), new reactions can target specific properties of the catalyst, such as selectivity, porosity, or deactivation speed. As for the potential catalysts to be investigated, I would propose to investigate the catalysts both widely used (zeolite technical bodies,[7] Lewis acid Zr/Ti/Hf/Sn-BEA zeolites[8]) and new (enantioselective MOFs,[9] ZSM-5 hollow fibers,[10] ultra-large pores zeolites[11]). Alternatively, another approach would be to forgo the use of fluorogenic reaction and modify the catalytic active sites so the intermediate or transition state of the active site is fluorescent and reports on the catalytic turnover.

6.1 REFERENCES

[1] J. Gascon, J. R. van Ommen, J. A. Moulijn, F. Kapteijn, *Catal. Sci. Technol.* **2015**, *5*, 807–817.

[2] C. Marcilly, *Acido-Basic Catalysis: Application to Refining and Petrochemistry, Volume 1*, Editions Technip, Paris, France, **2005**.

[3] M. C. Silaghi, C. Chizallet, J. Sauer, P. Raybaud, *J. Catal.* **2016**, *339*, 242–255.

[4] C. Chizallet, S. Lazare, D. Bazer-Bachi, F. Bonnier, V. Lecocq, E. Soyer, A. A. Quoineaud, N. Bats, *J. Am. Chem. Soc.* **2010**, *132*, 12365–12377.

[5] M. J. Booth, *Philos. Trans. R. Soc. A Math. Phys. Eng. Sci.* **2007**, *365*, 2829–2843.

[6] D. Belder, M. Ludwig, L.-W. Wang, M. T. Reetz, *Angew. Chem. Int. Ed.* **2006**, *45*, 2463–2466.

[7] S. Mitchell, N.-L. Michels, J. Pérez-Ramírez, *Chem. Soc. Rev.* **2013**, *42*, 6094-6112.

[8] C.-C. Chang, H. Je Cho, J. Yu, R. J. Gorte, J. Gulbinski, P. Dauenhauer, W. Fan, *Green Chem.* **2016**, *18*, 1368–1376.

[9] K. Leus, Y.-Y. Liu, P. Van Der Voort, *Catal. Rev.* **2014**, *56*, 1–56.

[10] J. Liu, G. Jiang, Y. Liu, J. Di, Y. Wang, Z. Zhao, Q. Sun, C. Xu, J. Gao, A. Duan, J. Liu, Y. Wei, Y. Zhao, L. Jiang, *Sci. Rep.* **2014**, *4*, 7276.

[11] A. Corma, M. J. Díaz-Cabañas, F. Rey, S. Nicolopoulus, K. Boulahya, *Chem. Commun.* **2004**, *12*, 1356–1357.

APPENDICES

APPENDIX 1 – APPLICATION OF 3D SUPER-RESOLUTION FLUORESCENCE MICROSCOPY TO CATALYSIS RESEARCH

7.1 INTRODUCTION

As discussed in the introduction, and in chapters 2, 3, and 5, super-resolution fluorescence microscopy for catalysis research benefits greatly from the improved lateral resolution. Examples of such techniques include NASCA, PALM, STORM, which achieve lateral resolutions down to 10 nm.[1,2] In these methods, the axial resolution still remains diffraction-limited, and depending on the experimental conditions, and localization parameters, can be estimated to about half a micrometer.[3,4] While such z-resolution still allows for 3D scanning of large particles of several micrometers or more in thickness, important structural information is lost. Additionally the majority of industrial zeolites catalysts consist of smaller nano-sized crystals. In order to obtain correct information from such crystals, 3D super-resolution microscopy could be considered. There are several reported ways that enable improving the axial resolution significantly. The most popular approaches use astigmatism-induced anisotropy of the PSF,[5,6] bi-plane detection,[7] and interferometric detection[8] to enhance the localization precision along the axial direction. In my PhD research I focused on the implementation of astigmatism-based 3D super-resolution due to relative technical simplicity of this approach. The working principle of this technique revolves around the controlled introduction of an astigmatic aberration in the detected fluorescence point-spread-function by the use of cylindrical lens in the detection pathway; the schematics of this method are given in **Figure 7.1**. As a result, the detected PSF has an elliptical shape instead of typical circular appearance. The orientation of the elliptical PSF and the extent of ellipticity is determined by the axial position of the emitter relative to the focal plane (**Figure 7.1A**). After calibration, e.g. by measuring the PSF of a fluorescent bead sample at precisely controlled axial positions, each experimental PSF obtained from a single emitter can be localized accurately not only in the lateral but also in the axial direction (**Figure 7.1B**). This yields typically axial resolution of about 50 nm (full width at half-maximum of localization distribution) and lateral resolutions of 25 nm (**Figure 7.1C**).

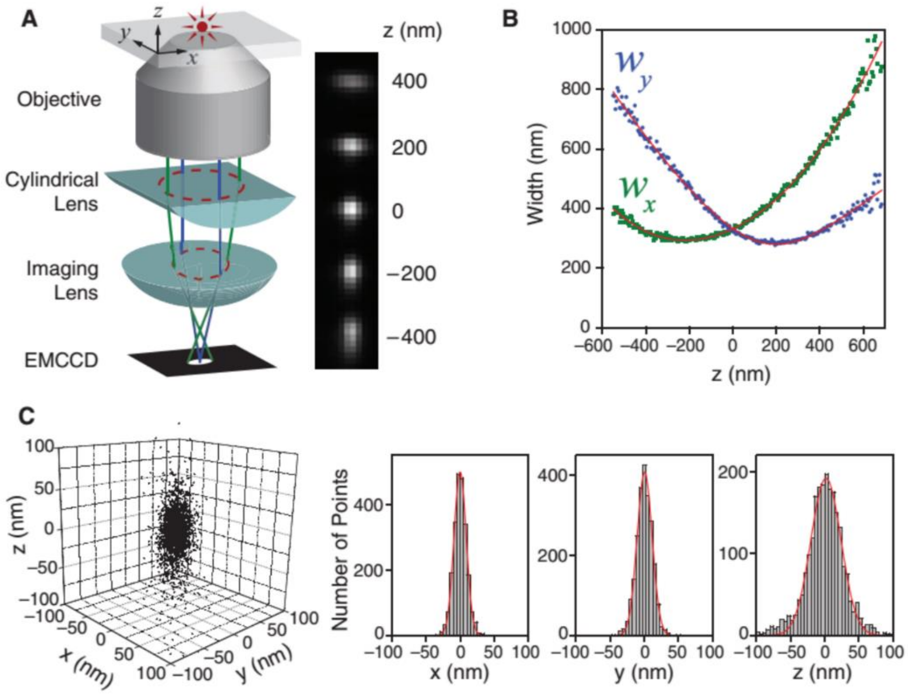

Figure 7.1. A schematic of 3D STORM. (A) Three dimensional localization of individual fluorophores. The simplified optical diagram illustrates the determination of the axial location of a fluorescent object, from the ellipticity of its PSF. Elliptical PSFs are achieved by introducing a cylindrical lens into the imaging path. The panel on the right shows images of a fluorophore at various z-positions. (B) Calibration curve of image widths wx and wy as functions of z obtained from single Alexa-647 molecules. Each data point represents the average value obtained from six molecules. The data were fit to a defocusing function (red curve). (C) 3D localization distribution of single molecules. Each molecule gives a cluster of localizations due to repetitive activation of the same molecule. Localizations from 145 clusters were aligned using their center of mass to generate the overall 3D representation of the localization distribution (left panel). Histograms of the distribution in x, y, and z (right panels) were fit to a Gaussian function, yielding standard deviations of 9 nm in x, 11 nm in y, and 22 nm in z. Reprinted with permission from B. Huang, W. Wang, M. Bates, X. Zhuang, Science. 2008, 319, 810–813.[5]

7.2 RESULTS AND DISCUSSION

In my PhD research I have integrated the described approach into the NASCA microscopy in order to obtain 3D super-resolution images of the catalytic performance. Specifically the acid-catalyzed furfuryl alcohol oligomerization on dealuminated mordenite was used (same system as described in Chapters 2 and 3) as well as the FDA hydrolysis on ZIF-8 (same system as described in Chapter 5). After recording the WFM images for calibration sample and investigated systems (**Figure 7.2**), the individual fluorescent reaction products were localized in 3D by fitting the elliptical PSFs with obtained calibration curves. In this way it is possible to retrieve the precise xyz-position of each localized fluorophores within a focal volume of about half a micron above and below the focal plane.

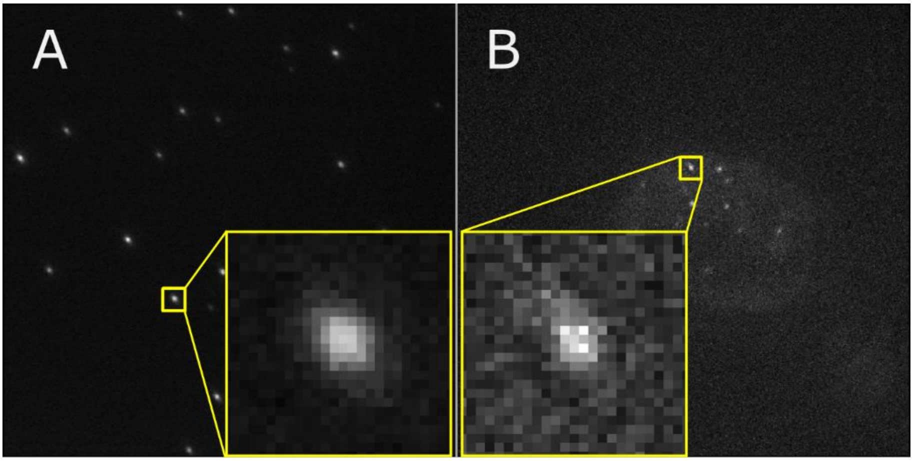

Figure 7.2. Elliptic PSFs in the WFM images of (A) calibration sample and (B) 3D NASCA investigation of furfuryl alcohol oligomerization within a dealuminated mordenite zeolite crystal.

The results of 3D imaging of investigated systems are shown in **Figures 7.3 and 7.4**, respectively.

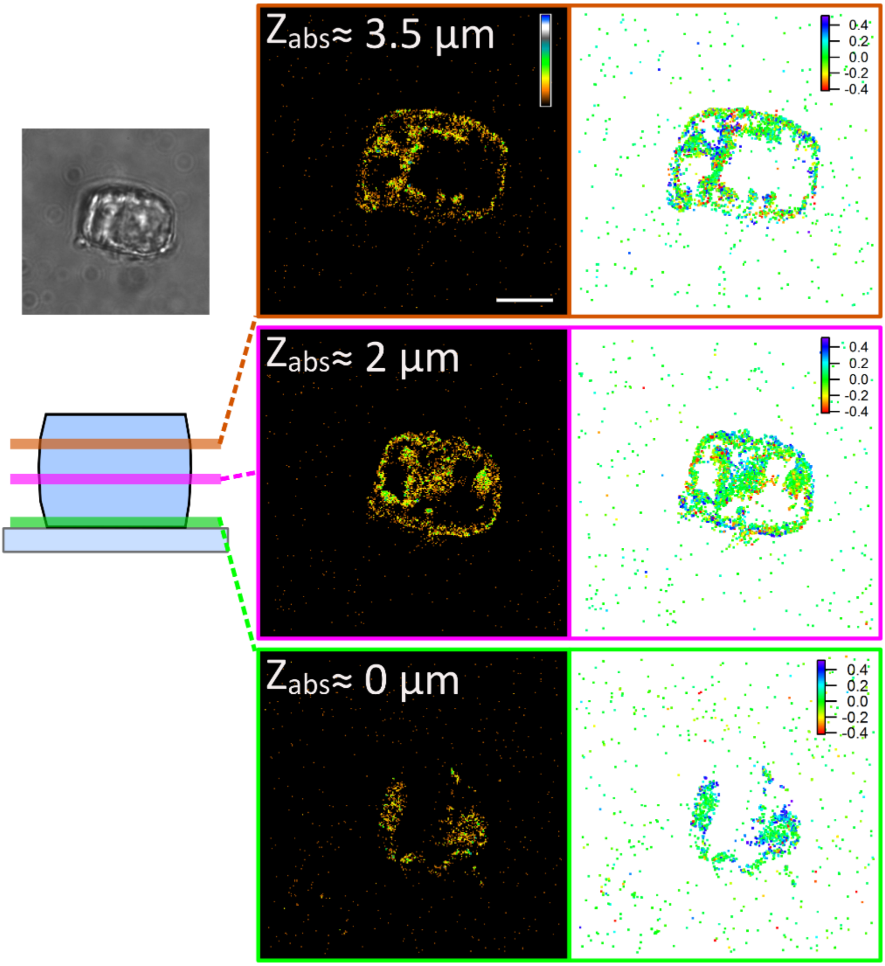

Figure 7.3. 3D NASCA investigation of furfuryl alcohol oligomerization within a dealuminated mordenite zeolite crystal. Left: Bright-field transmission image and crystal schematics showing the different depths of the crystal. Middle: NASCA accumulated images; false color scale shows the observed reaction rate (from 3.9×10^{-9} to 1.5×10^{-6} M·s^{-1}). Scale bar: 10 µm. Right: 3D positions of localized fluorophores; false color scale shows the z-positions in µm of fluorophores relative to those in the middle of focal plane.

After analysis a clear artifact becomes apparent. The effect is most pronounced in the ZIF-8 example where the majority of the localized reaction turnovers are localized below the focal plane; red color signifies that the turnovers are detected from about 600 nm below the focal plane.

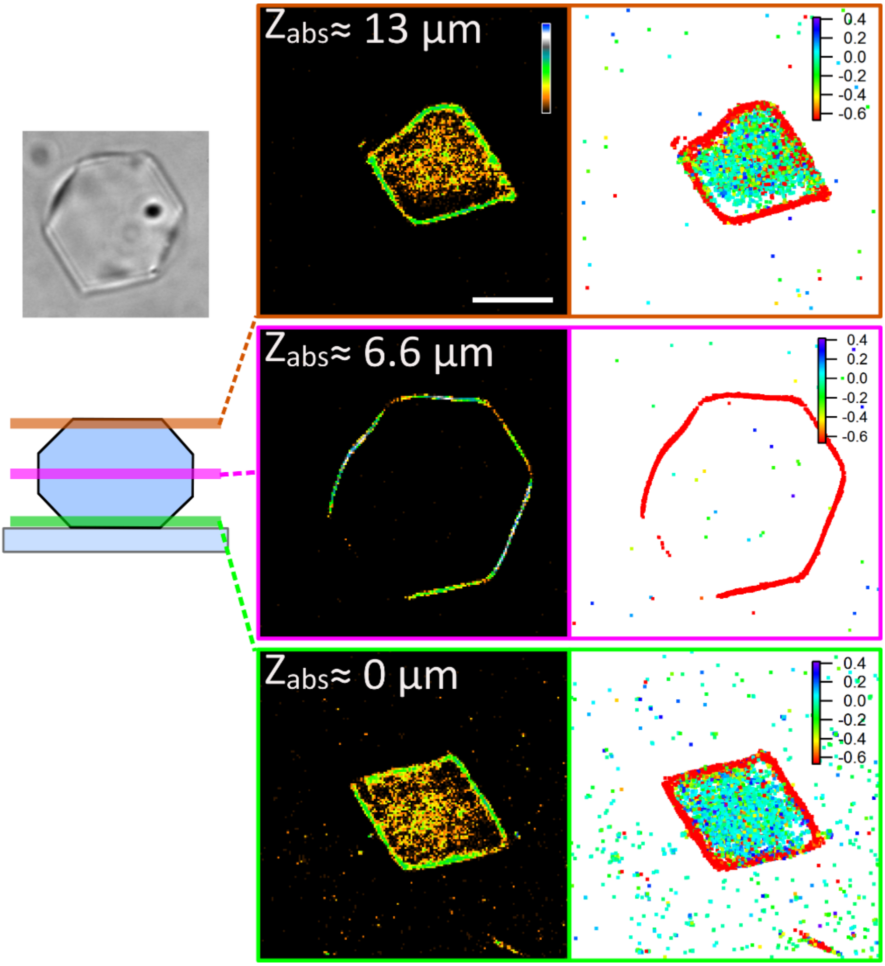

Figure 7.4. 3D NASCA investigation of FDA hydrolysis ZIF-8 crystal. Left: Bright-field transmission image and crystal schematics showing the different depths of the crystal. Middle: NASCA accumulated images; false color scale shows the observed reaction rate (from 5.7×10^{-9} to 1.7×10^{-6} $M \cdot s^{-1}$). Scale bar: 5 µm. Right: 3D positions of localized fluorophores; false color scale shows z-positions in µm of fluorophores relative to the middle of focal plane.

This is caused by spherical aberrations resulting from a mismatch in RI (n) between the cover glass ($n_{\mathrm{glass}} = 1.52$), catalyst crystals ($n_{\mathrm{zeolite}} = 1.472–1.487$[9]; $n_{\mathrm{zif\text{-}8}} = 1.34–1.35$[10]), and the surrounding reaction medium ($n_{\mathrm{water}} = 1.33$). This effect has been described before by Zhuang and co-workers[6] and a simplified schematic explaining the effects is shown in **Figure 7.5**.

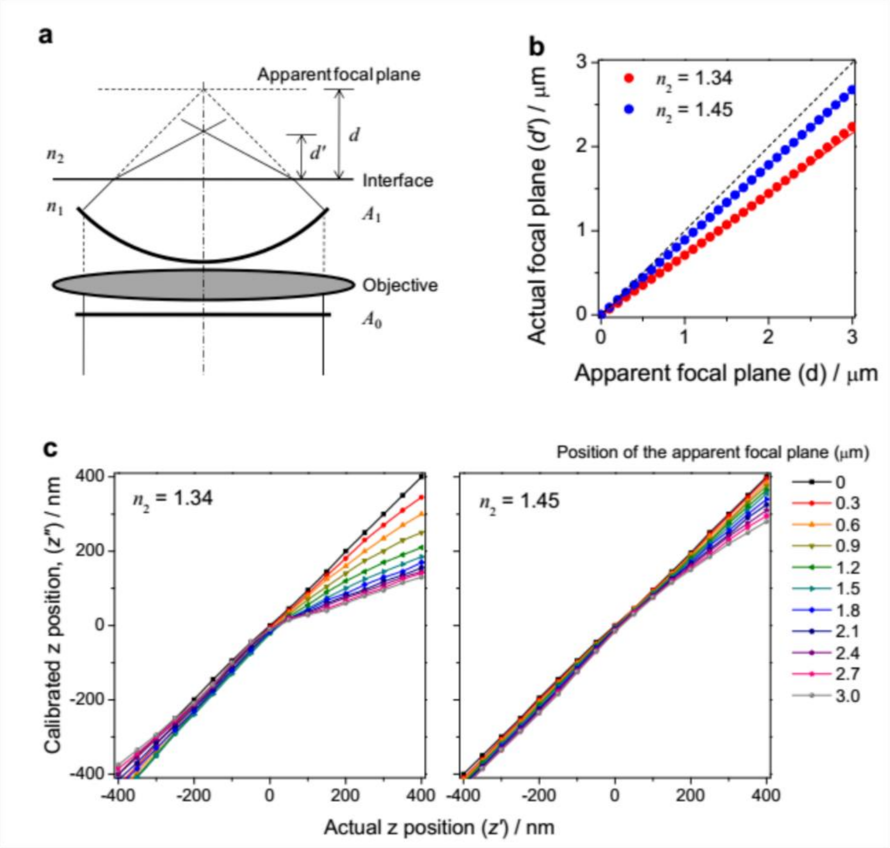

Figure 7.5. Z-localization correction for RI mismatch. (a) Schematic illustration of how refraction at the cover glass - imaging medium interface affects light ray propagation. An oil immersion objective was used to index-match the cover glass. Here A_0 and A_1 indicate the wavefront before and after light propagation through the objective, respectively, and n_1 and n_2 are the RI before and after the interface. The symbols d and d' denote the distance from the apparent and actual focal plane to the interface, respectively. (b) The relationship between d' and d determined by numerical simulation for $n_1 = 1.515$ and $n_2 = 1.34$ (red symbols) or $n_2 = 1.45$ (blue symbols). The results are well approximated by straight lines with slopes of 0.72 (red line) and 0.89 (blue line), respectively, except for a very small deviation of $n_2 = 1.34$ results above 1.5 μm. (c) Numerical simulation of the effect of the asymmetry in PSF caused by spherical aberration from RI mismatching. This effect causes an additional shift between the actual z-position of a fluorophore (z') measured from the actual focal plane and the apparent z-position (z'') determined from the calibration curve obtained using the focal plane at the interface. Reprinted by permission from B. Huang, S. A. Jones, B. Brandenburg, X. Zhuang, *Nat. Methods* **2008**, *5*, 1047–52.[6]

In a two-phase system (cover glass and the imaging medium) the relationship between actual and apparent focal planes can be approximated as linear within the first approximately 2-3 micrometers, enabling straightforward calculation of a corrected z-position. However, the investigated catalytic systems are more complex with at least three-components and imperfect catalyst crystals with irregular shapes. It proved to be very challenging to determine the correction parameters for such complex and irregular systems.

In an attempt to eliminate the effects of RI mismatch solvents with a RI matching that of the mordenite crystals (RI = 1.472 - 1.487)[9] was used: glycerol ($n_{glycerol}$ = 1.4731) and two different Cargille RI Fluids Series A (a mixtures of hydrocarbons with n = 1.460 and 1.480). However, the high viscosity of the used solvents prevented efficient diffusion of the furfuryl alcohol molecules, as well as reaction products. Furthermore, furfuryl alcohol solubility in Cargille RI fluids seemed to be rather low.

7.3 CONCLUSIONS

In conclusion, while it is possible to use RI-matching technique to reduce undesirable aberrations in catalytic systems studied using fluorescence microscopy, my attempts were unsuccessful. An alternative approach could make use of adaptive optics,[11] but this was not investigated in the framework of this PhD research.

7.4 REFERENCES

[1] J. Lippincott-Schwartz, G. H. Patterson, *Trends Cell Biol.* **2009**, *19*, 555–565.

[2] P. Lemmer, M. Gunkel, Y. Weiland, P. Müller, D. Baddeley, R. Kaufmann, A. Urich, H. Eipel, R. Amberger, M. Hausmann, et al., *J. Microsc.* **2009**, *235*, 163–171.

[3] K.-L. Liu, A. V. Kubarev, J. Van Loon, H. Uji-i, D. E. De Vos, J. Hofkens, M. B. J. Roeffaers, *ACS Nano* **2014**, *8*, 12650–12659.

[4] Z. Ristanović, J. P. Hofmann, G. De Cremer, A. V. Kubarev, M. Rohnke, F. Meirer, J. Hofkens, M. B. J. Roeffaers, B. M. Weckhuysen, *J. Am. Chem. Soc.* **2015**, *137*, 6559–6568.

[5] B. Huang, W. Wang, M. Bates, X. Zhuang, *Science* **2008**, *319*, 810–813.

[6] B. Huang, S. A. Jones, B. Brandenburg, X. Zhuang, *Nat. Methods* **2008**, *5*, 1047–1052.

[7] M. F. M. Juette, T. T. J. Gould, M. M. D. Lessard, M. J. Mlodzianoski, B. S. Nagpure, B. T. Bennett, S. T. Hess, J. Bewersdorf, *Nat. Methods* **2008**, *5*, 527–529.

[8] G. Shtengel, J. a Galbraith, C. G. Galbraith, J. Lippincott-Schwartz, J. M. Gillette, S. Manley, R. Sougrat, C. M. Waterman, P. Kanchanawong, M. W. Davidson, et al., *Proc. Natl. Acad. Sci. U. S. A.* **2009**, *106*, 3125–3130.

[9] R. L. Hay, in *Geol. Soc. Am. Spec. Pap.*, Geological Society Of America, **1966**, 1–122.

[10] S. Eslava, L. Zhang, S. Esconjauregui, J. Yang, K. Vanstreels, M. R. Baklanov, E. Saiz, *Chem. Mater.* **2013**, *25*, 27–33.

[11] M. J. Booth, *Philos. Trans. R. Soc. A Math. Phys. Eng. Sci.* **2007**, *365*, 2829–2843.

APPENDIX 2 – FURFURYL ALCOHOL OLIGOMERIZATION MECHANISM

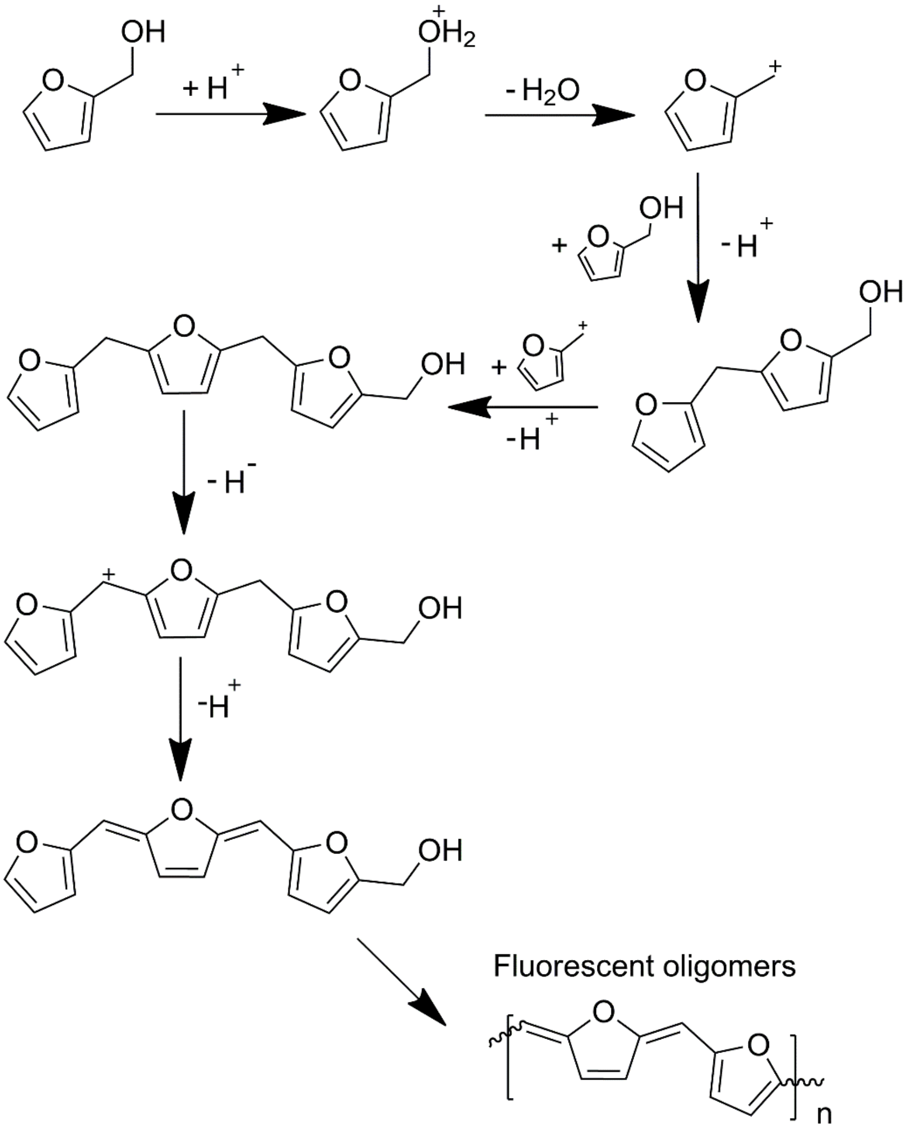

Figure 8.1. The mechanism of main reaction pathway of acid-catalyzed furfuryl alcohol oligomerization based on [1-4]

8.1 REFERENCES

[1] M. Choura, N. M. Belgacem, A. Gandini, *Macromolecules* **1996**, *29*, 3839–3850.

[2] S. Bertarione, F. Bonino, F. Cesano, A. Damin, D. Scarano, A. J. Zecchina, *Phys. Chem. B* **2008**, *112*, 2580–2589.

[3] T. Kim, R. S. Assary, C. L. Marshall, D. J. Gosztola, L. A. Curtiss, P. C. Stair, *ChemCatChem* **2011**, *3*, 1451–1458.

[4] T. Kim, R. S. Assary, R. E. Pauls, C. L. Marshall, L. A. Curtiss, P. C. Stair, *Catal. Commun.* **2014**, *46*, 66–70.

CURRICULUM VITAE

PERSONALIA

Name: Alexey V. Kubarev
Address: Groenstraat 59/1, 3001 Leuven, Belgium
Mobile phone: +32 488 94 85 63
E-mail: kubarev.alexey@gmail.com
Date of Birth: December 18, 1987
Place of Birth: Omsk, Russia
Nationality: Russian

EDUCATION AND WORK EXPERIENCE

2013 – 2017	PhD degree in bioscience engineering Centre for surface chemistry and catalysis, KU Leuven Leuven, Belgium
2004 – 2012	Assistant chemistry teacher Public school “Advanced Educational Scientific Center of Lomonosov Moscow State University” Moscow, Russia
2009 – 2011	Chemistry teacher Public school “Intellectual” Moscow, Russia
2004 –2009	Diploma (M.Sc. equivalent): Chemistry (Magna Cum Laude) Lomonosov Moscow State University Moscow, Russia
2005 –2009	Additional education degree: Teacher (Summa Cum Laude) Lomonosov Moscow State University Moscow, Russia

LANGUAGES

Russian – native

Dutch – intermediate

English – fluent

French – beginner

VOLUNTEERING ACTIVITIES

2004 – 2014	Organizer, administrator, and chemistry teacher, Academic summer camp “Chimera” Kaluga Province, Russia

PUBLICATION LIST

[1] **A. V. Kubarev,** E. Breynaert, J. Van Loon, A. Layek, G. Fleury, S. Radhakrishnan, J. A. Martens, M. B. J. Roeffaers
Solvent Polarity-Induced Pore Selectivity in H-ZSM-5 Catalysis.
ACS Catalysis, **2017,** *7,* 4248–4252

[2] **A. V. Kubarev,** M. B. J. Roeffaers
Surface Acid-Base Catalytic Activity of ZIF-8 Revealed by Superresolution Fluorescence Microscopy.
CrystEngComm, **2017,** DOI: 10.1039/C7CE00074J

[3] X. Zhu, N. Kosinov, **A. V. Kubarev,** A. Bolshakov, B. Mezari, I. Valastyan, J. P. Hofmann, M.B.J. Roeffaers, E. Sarkadi-Pribóczki, E. J. M. Hensen
Probing the Influence of SSZ-13 Zeolite Pore Hierarchy in MTO Catalysis by NASCA microscopy and Positron Emission Profiling.
ChemCatChem, **2017,** DOI: 10.1002/cctc.201700567

[4] Z. Ristanović, **A. V. Kubarev,** J. Hofkens, M. B. J. Roeffaers, B. M. Weckhuysen
Single Molecule Nanospectroscopy Visualizes Proton-Transfer Processes within a Zeolite Crystal.
Journal of the American Chemical Society, **2016,** *138*, 13586–13596

[5] Z. Ristanović, J. P. Hofmann, G. De Cremer, **A. V. Kubarev,** M. Rohnke, F. Meirer, J. Hofkens, M. B. J. Roeffaers, B. M. Weckhuysen
Quantitative 3D Fluorescence Imaging of Single Catalytic Turnovers Reveals Spatiotemporal Gradients in Reactivity of Zeolite H-ZSM-5 Crystals upon Steaming.
Journal of the American Chemical Society, **2015,** *137*, 6559–6568

[6] **A. V. Kubarev,** K. P. F. Janssen, M. B. J. Roeffaers
Noninvasive Nanoscopy Uncovers the Impact of the Hierarchical Porous Structure on the Catalytic Activity of Single Dealuminated Mordenite Crystals.
ChemCatChem, **2015,** *7,* 3646–3650

[7] Z. Ristanović, M. M. Kerssens, **A. V. Kubarev,** F. C. Hendriks, P. Dedecker, J. Hofkens, M. B. J. Roeffaers, B. M. Weckhuysen
High-Resolution Single-Molecule Fluorescence Imaging of Zeolite Aggregates within Real-Life Fluid Catalytic Cracking Particles.
Angewandte Chemie - International Edition, **2015**, *54*, 1836–1840

[8] K. P. F. Janssen, G. De Cremer, R. K. Neely, **A. V. Kubarev,** J. Van Loon, J. A. Martens, D. E. De Vos, M. B. J. Roeffaers, J. Hofkens
Single Molecule Methods for the Study of Catalysis: from Enzymes to Heterogeneous Catalysts.
Chemical Society Reviews, **2014**, *43*, 990–1006.

[9] K.-L. Liu,* **A. V. Kubarev,*** J. Van Loon, H. Uji-i, D. E. De Vos, J. Hofkens, M. B. J. Roeffaers
Rationalizing Inter- and Intracrystal Heterogeneities in Dealuminated Acid Mordenite Zeolites by Stimulated Raman Scattering Microscopy Correlated with Super-resolution Fluorescence Microscopy.
ACS Nano, **2014,** *8*, 12650–12659.

[10] P. Valvekens, D. Jonckheere, T. De Baerdemaeker, **A. V. Kubarev,** M. Vandichel, K. Hemelsoet, M. Waroquier, V. Van Speybroeck, E. Smolders, D. Depla, M. B. J. Roeffaers, D. E. De Vos
Base Catalytic Activity of Alkaline Earth MOFs: a (Micro)Spectroscopic Study of Active Site Formation by the Controlled Transformation of Structural Anions.
Chemical Science, **2014,** *5*, 4517–4524.

***Equal contribution**

CONFERENCE PARTICIPATION

[1] **A. V. Kubarev,** K.-L. Liu, M. B. J. Roeffaers
Oral presentation: Inter- and Intracrystal Heterogeneity in Catalytic Activity of Dealuminated Mordenites.
Symposium Chemical Research in Flanders-1,
Blankenberge, Belgium, **October 2016**

[2] **A. V. Kubarev,** K.-L. Liu, M. B. J. Roeffaers
Oral presentation: Inter- and Intracrystal Heterogeneity in Catalytic Activity of Dealuminated Mordenites.
18th International zeolite conference,
Rio De Janeiro, Brazil, **June 2016**

[3] **A. V. Kubarev,** K.-L. Liu, M. B. J. Roeffaers
Poster presentation: Inter- and Intracrystal Heterogeneity in Catalytic Activity of Dealuminated Mordenites.
Gordon Research Conference in Catalysis,
New London, New Hampshire, United States, **June 2016**

[4] **A. V. Kubarev,** K. Janssen, M. B. J. Roeffaers
Poster presentation: Impact of the Hierarchical Porous Structure on Catalytic Activity of Dealuminated Mordenite: Single-Crystal Study.
17th International Symposium on Relations between Homogeneous and Heterogeneous Catalysis,
Utrecht, The Netherlands, **July 2015**

[5] **A. V. Kubarev,** J. Van Loon, J. Hofkens, M. B. J. Roeffaers
Oral presentation: Intercrystal and Intracrystal Heterogeneity in Catalytic Activity of Dealuminated Mordenites Revealed by Fluorescence Microscopy.
6th international conference of the Federation of European Zeolite Associations (FEZA),
Leipzig, Germany, **September 2014**

[6] **A. V. Kubarev,** P. Valvekens, D. E. De Vos, J. Hofkens, M. B. J. Roeffaers
Poster presentation: Catalytic Performance of Base Metal-Organic Frameworks Investigated by Single-Molecule Fluorescence Microscopy.
Gordon Research Conference in Catalysis,
New London, New Hampshire, United States, **June 2014**

[7] **A. V. Kubarev,** J. Van Loon, F. Lusitani, J. Hofkens, M. B. J. Roeffaers
Poster presentation: Heterogeneities of Catalytic Activity in Dealuminated Mordenites.
15th Netherlands' Catalysis and Chemistry Conference,
Noordwijkerhout, The Netherlands, **March 2014**

[8] **A. V. Kubarev,** J. Van Loon, F. Lusitani, J. Hofkens, M. B. J. Roeffaers
Poster presentation: Single Turnover Reactivity Mapping of Dealuminated Mordenites by Fluorescence Microscopy.
26th International Conference on Photochemistry,
Leuven, Belgium, **July 2013**

NOTES

....

....

....

....

....

....

....

....

....

....

....

....

....

....

....

....

....

....

....

....

....

……………………………………………………………………………………

……………………………………………………………………………………

……………………………………………………………………………………

……………………………………………………………………………………

……………………………………………………………………………………

……………………………………………………………………………………

……………………………………………………………………………………

……………………………………………………………………………………

……………………………………………………………………………………

……………………………………………………………………………………

……………………………………………………………………………………

……………………………………………………………………………………

……………………………………………………………………………………

……………………………………………………………………………………

……………………………………………………………………………………

……………………………………………………………………………………

……………………………………………………………………………………

……………………………………………………………………………………

…………………………………………………………………………